Ocean Boundary Layer Dynamics and Air-Sea Interaction

Jacob O. Wenegrat

A dissertation
submitted in partial fulfillment of the
requirements for the degree of

Doctor of Philosophy

University of Washington

2015

Reading Committee:

Michael J. McPhaden, Chair

Ren-Chieh Lien

Stephen C. Riser

Program Authorized to Offer Degree:
School of Oceanography

University of Washington

Abstract

Ocean Boundary Layer Dynamics
and Air-Sea Interaction

Jacob O. Wenegrat

Chair of the Supervisory Committee:
Senior Scientist Michael J. McPhaden
Pacific Marine Environmental Laboratory, NOAA

The dynamics of the ocean surface boundary layer are examined using theory, high-resolution moored observations from the equatorial Atlantic ocean, and idealized modeling. An approximate solution is found for the ocean response to wind-forcing in the presence of baroclinic pressure gradients, surface wave shear, and spatially varying turbulent mixing. The manner in which these parameters modify the classic physical model of the wind-forced ocean is discussed, and estimates of their spatial distribution are provided. Next, the role of time-varying shear in determining the near-surface eddy viscosity is assessed using velocity observations from the equatorial Atlantic, and the implications for several simple parameterizations are considered. These observations are then utilized to provide a first in situ observational assessment of the diurnal cycle of shear and stratification in the equatorial Atlantic, demonstrating how mixed-layer dynamics modulate the diurnal cycle of sea surface temperature, coupling the dynamic and thermodynamic responses. Further, these results suggest the existence of a deep-cycle turbulence layer in the equatorial Atlantic, providing a complementary perspective on similar recent work from the Pacific. Finally, the effect of time-varying eddy viscosity on the low-frequency wind-driven flow is assessed using theory and idealized modeling, providing a new conceptual tool for understanding the dynamics of the near-surface ocean, and for guiding the interpretation of observations. A particular focus

throughout this thesis is the role of ocean dynamics in determining the near-surface ocean response to surface atmospheric fluxes.

TABLE OF CONTENTS

LIST OF FIGURES

Figure Number Page

LIST OF TABLES

ACKNOWLEDGMENTS

There are many people from the University of Washington, the UW Applied Physics Laboratory, and the NOAA Pacific Marine Environmental Laboratory who I thank for their role in this work, as well as for their camaraderie and friendship throughout my time here. I feel honored to have had the opportunity to participate in this wonderful community of scientists.

In particular, I thank my advisor Mike McPhaden, who gave me the support, guidance, and most of all the tremendous intellectual freedom necessary to pursue these ideas. I also thank my committee for their advice, encouragement, and generosity with their time throughout this process: Curtis Deutsch, Charlie Eriksen, Dennis Hartmann, Ren-Chieh Lien, Jim Murray, and Steve Riser. LuAnne Thompson welcomed me into her group, and Susan Hautala gave me the opportunity to co-instruct a class with her, both of which significantly enhanced my experience as a graduate student.

Two of the chapters of this thesis utilize data from the PIRATA array in the equatorial Atlantic, and I thank Paul Freitag, the TAO project office at PMEL, as well as all those involved in the global tropical mooring arrays. The data collected through these efforts are invaluable.

I thank my parents, Anne and Brant Wenegrat, for instilling in me an appreciation for higher education and science, and for all their support along my path to this point.

Finally, none of this would have been possible or worthwhile without the encouragement (and enablement) of my wife Julia Wenegrat, and my son Ezra Wenegrat.

DEDICATION

For Julia and Ezra.

Chapter 1
INTRODUCTION

The dynamics of the near-surface ocean play a central role in determining air-sea interactions, critical across many aspects of the earth system. Connecting the atmosphere and ocean, physical processes in the ocean surface boundary layer (OSBL) mediate the exchange of heat and momentum, as well as a wide range of biological and chemical fluxes. Despite the critical importance of the dynamics of the OSBL, it remains largely under-sampled, as observational investigation poses particular challenges to traditional forms of oceanographic measurement, with shipboard measurements typically limited to below the ship's draft, and moored observations often lacking the vertical resolution necessary to resolve detailed boundary layer processes. Modern forms of oceanographic observations, including autonomous floats, gliders, and remote sensing, have greatly improved our overall understanding of the OSBL, but generally lack detailed information on the velocity field[1], arguably the most fundamental dynamical measurement. Where near-surface velocity is resolved by these measurement techniques it is often only at a single depth, as for instance with the Global Drifter Program whose drifting surface buoys report ocean currents at 15 m depth (Lumpkin and Johnson, 2013), and thus do not resolve the vertical structure of boundary layer currents. This relatively scarcity of observational evidence has amplified the importance of theory and modeling in informing our understanding of the physical processes which take place in the near-surface ocean, and many important open questions remain. This thesis contributes to our understanding of the dynamics of the OSBL, using a combination of basic theory, a unique set of high-resolution moored observations of near-surface velocity, and idealized mod-

[1] A notable exception to this being the EM-APEX floats (Sanford et al., 2005).

eling. Particular focus is given to the role of ocean dynamics in determining the boundary layer response to surface fluxes of momentum and heat.

This work begins with a re-examination of the basic theory of frictionally driven flows in the OSBL (chapter 2). Building on recent observational and theoretical work (Polton et al., 2005; Cronin and Kessler, 2009; Gula et al., 2014; McWilliams et al., 2015), the classic Ekman theory (Ekman, 1905) of wind-driven frictional flow is extended to include the effects of ocean sources of shear, and spatial variability in mixing (Wenegrat and McPhaden, 2015b). Special consideration is given to shear arising from baroclinic pressure gradients, and the Stokes shear associated with the surface wave field, both of which, it is argued, have the potential to be of first-order importance to boundary layer flows across much of the global oceans. In chapter 3, the role of time-varying near-surface shear in determining the turbulent viscosity is explored using near-surface velocity observations taken in the equatorial Atlantic at 0°, 23°W (Wenegrat et al., 2014). The implications of this variability for parameterizations of turbulent viscosity are also discussed.

Chapter 4 extends the analysis of these observations to focus on the diurnal cycle of near-surface stratification and shear, where the ocean dynamical response to wind-driven surface momentum flux is shown to modulate the diurnal sea surface temperature cycle, with enhanced near-surface shear leading to conditions favorable for shear instability, deepening the mixed layer and limiting near-surface temperature anomalies (Wenegrat and McPhaden, 2015a). The stability characteristics of the flow below the mixed layer are also found to be suggestive of an equatorial deep-cycle turbulence regime, providing an important first counterpart of this type to the limited direct microstructure measurements available in this area (Hummels et al., 2013, 2014), and complementing similar recent work from the Pacific (Smyth and Moum, 2013; Smyth et al., 2013). In Chapter 5 the role of time-varying turbulent mixing on the Ekman solutions is addressed, using a combination of theory and idealized modeling, with a focus on the physical mechanisms through which time-varying mixing results in low-frequency rectification, altering the vertical structure of boundary layer flows.

Chapter 2

WIND, WAVES, AND FRONTS: FRICTIONAL EFFECTS IN A GENERALIZED EKMAN MODEL

Ocean currents in the surface boundary layer are sensitive to a variety of parameters not included in classic Ekman theory, including the vertical structure of eddy viscosity, finite boundary layer depth, baroclinic pressure gradients, and surface waves. These parameters can modify the horizontal and vertical flow in the near-surface ocean, making them of first-order significance to a wide range of phenomenon of broad practical and scientific import. In this work, an approximate Green's function solution is found for a model of the frictional ocean surface boundary layer, termed the generalized Ekman (or Turbulent Thermal Wind) balance. The solution admits consideration of general, more physically realistic, forms of parameters than previously possible, offering improved physical insight into the underlying dynamics. Closed form solutions are given for the wind-driven flow in the presence of Coriolis-Stokes shear, a result of the surface wave field, and thermal wind shear, arising from a baroclinic pressure gradient, revealing the common underlying physical mechanisms through which they modify currents in the ocean boundary layer. These dynamics are further illustrated by a case study of an idealized two-dimensional front. The solutions, and estimates of the global distribution of the relative influence of surface waves and baroclinic pressure gradients on near-surface ocean currents, emphasize the broad importance of considering ocean sources of shear and physically realistic parameters in the Ekman problem.[1]

---

[1]An edited version of this chapter was published as: Wenegrat, J.O. and M.J. McPhaden, 2015: Wind, waves, and fronts: Frictional effects in a generalized Ekman model. *J. Phys. Ocean.*

2.1 Introduction

Diagnosing velocities in the ocean boundary layer is key to many issues of broad practical and scientific importance, from larval dispersion, to search and rescue, to the general ocean circulation. Today much of our understanding of boundary layer currents remains rooted in classic Ekman theory, which holds that, with some knowledge of the turbulent eddy viscosity, the ageostrophic ocean response is completely determined by the surface wind stress (Ekman, 1905). However, despite the tremendous explanatory power of Ekman theory, basic observational confirmation of the structure of flow in the boundary layer has been challenging.

In response to discrepancies between the theory and observations, a large literature has developed, focused on modifications to the classic Ekman theory. Broadly speaking the proposed modifications to Ekman theory can be divided into local one-dimensional mechanisms, such as time-variability (Price et al., 1986; Schudlich and Price, 1998; Price and Sundermeyer, 1999; McWilliams et al., 2009), vertical structure in eddy viscosity (Madsen, 1977; Miles, 1994; Grisogono, 1995), or finite boundary layer depth (Welander, 1957; Stommel, 1960; Lewis and Belcher, 2004; Elipot and Gille, 2009), and mechanisms that involve non-local effects such as horizontal buoyancy gradients (McPhaden, 1981; Cronin and Kessler, 2009), surface waves (Huang, 1979; Jenkins, 1986; Xu and Bowen, 1994; Lewis and Belcher, 2004; Polton et al., 2005), and non-linearity (Stern, 1965; Niiler, 1969; Thomas and Rhines, 2002). Many of these proposed modifications have closed the gap between theory and observations, however, generally analytic solutions are only available for specific forms of parameters, limiting the possibility for inter-comparison of the various proposed mechanisms, and critically, their application to realistic ocean fields.

Here we utilize a simple model of the viscous boundary layer, termed the generalized Ekman model (Cronin and Kessler, 2009), or the Turbulent Thermal Wind balance (Gula

et al., 2014). This model contains many of the modifications to basic Ekman theory that have been proposed individually, and has already proven successful in explaining observed horizontal currents (Cronin and Kessler, 2009), as well as modeled boundary layer vertical velocities (Gula et al., McWilliams et al., 2015). Previously, solutions to this model with physically realistic parameters required numerical methods, with analytic solutions available only for greatly simplified forms of the parameters (Bonjean and Lagerloef, 2002; Cronin and Kessler, 2009; McWilliams et al., 2015), limiting insight into the underlying dynamics.

In this manuscript we significantly extend these earlier results by providing an approximate solution to the generalized Ekman (Turbulent Thermal Wind) model that can accommodate a wide-range of physically realistic parameters, providing a unifying framework for many of the individually proposed modifications to classic Ekman theory (section 2.2). Using this solution, two limiting cases, corresponding to a surface wave field and a horizontal buoyancy gradient, are explored to further illuminate the underlying dynamics (section 2.3). The approximate solutions to these limiting cases reveal how these two ocean dynamic processes modify the Ekman solution in similar ways, drawing a previously unnoted connection between these processes, and their accompanying literatures.

In section 2.4 the solution is applied to an idealized front, illustrating how thermal wind shear in the presence of viscosity can alter both the Ekman layer flow as well as drive overturning circulations in the boundary layer (Garrett and Loder, 1981; Thompson, 2000; McWilliams et al., 2015). Estimates of the global distribution of wave and baroclinic pressure gradient effects on frictional boundary layer flow (section 2.5), and scaling analysis, suggest that these ocean dynamical processes can be expected to be of first order importance in determining near-surface currents for much of the world's oceans.

2.2 Theory

We consider steady, Boussinesq, flow in hydrostatic balance, where the complex horizontal velocity is denoted by $\boldsymbol{u} \equiv u + iv$, and $\nabla \equiv \frac{\partial}{\partial x} + i\frac{\partial}{\partial y}$. Horizontal mixing is ignored, and vertical mixing is parameterized by a turbulent eddy viscosity, A_v, which is considered to

be a specified parameter, allowed to vary vertically subject to moderate constraints imposed by the approximation technique utilized, as discussed below. The horizontal and vertical momentum equations are thus given by,

$$if\boldsymbol{u} = -\frac{1}{\rho_0}\nabla P + \frac{\partial}{\partial z}\left(A_v \frac{\partial \boldsymbol{u}}{\partial z}\right), \tag{2.1}$$

$$0 = -\frac{1}{\rho_0}\frac{\partial P}{\partial z} + b. \tag{2.2}$$

Where the Rossby number, $\epsilon = U/fL$, is assumed small, and therefore the non-linear advection terms are excluded. Equation (2.2) expresses the hydrostatic balance, where $b = -g\rho/\rho_0$ is the buoyancy, also considered to be a known quantity, allowed to vary in the horizontal and vertical.

Equation (2.1), a balance between the Coriolis acceleration, the pressure gradient force, and the turbulent diffusive flux convergence provides the basic starting point for Ekman theory. Deriving Ekman's 1905 result begins with a decomposition of the total velocity into a geostrophic velocity in balance with the pressure gradient force ($\boldsymbol{u_g} = i(\rho_0 f)^{-1}\nabla P$), and solving for the ageostrophic velocity ($\boldsymbol{u_a} = \boldsymbol{u} - \boldsymbol{u_g}$) in a boundary layer with characteristic thickness $h_{Ek} = \sqrt{2A_v/f}$, the Ekman depth, where it is assumed that A_v is vertically uniform and $\nabla b = 0$ (see for example Gill, 1982, section 9.6). Equation (2.1) is a second order linear ordinary differential equation for velocity and so requires two boundary conditions on $\boldsymbol{u}$, given for the classic Ekman problem by $\rho A_v \partial \boldsymbol{u_a}/\partial z = \boldsymbol{\tau_w}$ at the surface, where $\boldsymbol{\tau_w}$ is the surface wind stress, and $\boldsymbol{u_a} \to 0$ as $z \to -\infty$.

Here we take a more general approach that does not require separating into geostrophic and ageostrophic components, by first vertically differentiating (2.1), and multiplying by $\rho_0 A_v(z)$ to form an equation for the stress, $\boldsymbol{\tau} = \rho_0 A_v(z)\partial \boldsymbol{u}/\partial z$, which we refer to as the generalized Ekman model (following Cronin and Kessler, 2009),

$$A_v(z)\frac{\partial^2 \boldsymbol{\tau}}{\partial z^2} - if\boldsymbol{\tau} = \rho_0 A_v(z)\nabla b, \tag{2.3}$$

$$\boldsymbol{\tau}(0) = \boldsymbol{\tau_w}, \tag{2.4}$$

$$\boldsymbol{\tau}(-h) = 0. \tag{2.5}$$

The relationship of this model to various alternate Ekman layer formulations is discussed in detail by Cronin and Kessler (2009), however we further note that this is the same model termed the Turbulent Thermal Wind balance by Gula et al. (2014, and McWilliams et al. 2015) in their investigation of submesoscale cold filament dynamics.

The surface boundary condition, (2.4), is unchanged from the classic Ekman problem, however the bottom boundary condition, (2.5), is posed as a no-stress condition, applied at a finite depth $z = -h$, rather than the no-slip condition utilized in the classic Ekman problem. This formulation of the problem maintains the classic Ekman transport, even in the presence of geostrophic shear at the base of the layer (Cronin and Kessler, 2009), and is applicable at low latitudes or in depth limited seas (Stommel, 1960; Bonjean and Lagerloef, 2002). The solution technique utilized below is a global method, as opposed to a local boundary layer expansion, and thus sufficiently far from the boundary layer the solution will approach the inviscid limit. This gives a measure of flexibility in the choice of an appropriate h, however on the basis of physical arguments, developed further below, h should be chosen to be deeper than significant sources of geostrophic stress (defined in section 2.3.2), so as to avoid the creation of a spurious interior 'Ekman' layer. When $h \gg h_{Ek}$, as is the case for most of the extra-tropics, the near-surface solution is insensitive to the particular bottom boundary condition, and we further note that for the solutions given below letting $h \to \infty$ results in simplified forms of the solutions that are equivalent to applying the bottom boundary condition $\tau \to 0$ as $z \to -\infty$. However, if a no-slip boundary condition is desired, the derivation follows directly from that given in Appendix A.

To solve this linear inhomogeneous ordinary differential equation with non-constant coefficients, we first approximate a solution to the homogenous formulation of equation (2.3) using the Wentzel-Kramer-Brillouin (WKB) method (Bender and Orszag, 1978; Grisogono, 1995), and then solve for the inhomogeneous solution using variation of parameters (Hidaka,

1955; Berger and Grisogono, 1998). A detailed derivation of the full solution is presented in Appendix A, however, briefly, the WKB method assumes the solution can be represented as:

$$\tau \propto e^{(S_0+S_1\delta+S_2\delta^2+\ldots)\frac{1}{\delta}}. \tag{2.6}$$

Here, we use the physical optics approximation, and solve to first order (S_1). The distinguished limit for the small parameter δ is found to be $\delta \sim Ek^{\frac{1}{2}}$, where $Ek = A_v/fH^2$, the Ekman number. The classic non-dimensionalization of (2.1), for uniform A_v, identifies H as the depth scale of the interior flow, which for values typical of a stratified mid-latitude ocean ($A_v \sim 10^{-2}\,\mathrm{m^2 s^{-1}}$, $f \sim 10^{-4}\mathrm{s^{-1}}$, $H \sim 100\,\mathrm{m}$) gives $Ek \sim O(10^{-2})$. However, retaining vertical structure in A_v introduces an additional vertical length scale, h_{Av}, into the problem. We thus have six physically relevant terms (A_v, f, u_g, u_a, H, h_{Av}), with two physical dimensions (time and length). Application of the Buckingham Pi theorem (Buckingham, 1914) then gives 4 non-dimensional parameters, 2 of which take the form of an Ekman number, $\pi_1 = A_{v0}/fH^2$ and $\pi_2 = A_{v0}/fh_{Av}^2$. The latter of these is likely to be a stricter constraint on the validity of the WKB expansion when applied to realistic forms of A_v (Appendix B).

Formally, the use of the WKB approximation requires that the properties of the medium vary more slowly than the solution (Bender and Orszag, 1978), a condition which may be violated in some geophysical flows. Further analysis of this requirement is given in Appendix A, however, as discussed in Appendix B, we find good agreement between numerical and approximate solutions for a range of A_v profiles, and values of Ek (see also Grisogono, 1995), although we emphasize that care must be taken to assess the accuracy of the solution when applied to any specific A_v profile. For simplicity we also require that $A_v > 0$ throughout the layer, so as to avoid the additional complexity of singularities in the equation. This constraint, and the WKB condition (A12), does not allow the direct application of the solution to cases where $A_v \to 0$ as $z \to 0$, a structure which is implied by Monin-Obukhov similarity theory, and which occurs in commonly utilized parameterizations such as the K-Profile Parameterization (KPP) (Large et al., 1994). If necessary, this restriction can be

removed by patching the WKB solution to an inner solution, valid in a thin layer as $A_v \to 0$, an example of which is given in Appendix B. Despite these limitations, the simplicity, and generality, of the WKB method argue its utility, particularly in comparison to the often strict parameter requirements associated with other analytic solutions techniques.

Once the WKB solution to the homogenous problem is identified, the inhomogeneous solution can be found using variation of parameters, and stated in terms of a Green's function. The full solution (as derived in Appendix A) is thus given by,

$$\boldsymbol{\tau(z)} = \boldsymbol{\tau_w} \left(\frac{A_v(z)}{A_v(0)} \right)^{\frac{1}{4}} \frac{\sinh\left[\theta(z)\right]}{\sinh\left[\theta(0)\right]} + \int_{-h}^{0} G(z,s) \left[\rho_0 \nabla b\right] \, \mathrm{d}s. \tag{2.7}$$

Where,

$$\theta(z) = \sqrt{if} \int_{-h}^{z} A_v(Z)^{-\frac{1}{2}} \, \mathrm{d}Z, \tag{2.8}$$

and, $G(z,s)$ is the symmetric Green's function,

$$G(z,s) = \begin{cases} \frac{\sinh[\theta(z)] \sinh[\theta(s) - \theta(0)] A_v(s)^{\frac{1}{4}} A_v(z)^{\frac{1}{4}}}{\sinh[\theta(0)] \sqrt{if}} & \text{if } s > z, \\ \frac{\sinh[\theta(s)] \sinh[\theta(z) - \theta(0)] A_v(s)^{\frac{1}{4}} A_v(z)^{\frac{1}{4}}}{\sinh[\theta(0)] \sqrt{if}} & \text{if } s < z. \end{cases} \tag{2.9}$$

This general solution is a primary result of this manuscript.

Velocity shear follows directly from the definition of stress. However, equation (2.3) is a third-order linear ordinary differential equation in velocity, and hence to go from shear to velocity requires an additional boundary condition. Here, to determine velocity we use the solution for stress directly in the momentum equation (2.1),

$$if\boldsymbol{u} = -\frac{1}{\rho} \nabla P + \frac{1}{\rho} \frac{\partial \boldsymbol{\tau}}{\partial z}, \tag{2.10}$$

where $\boldsymbol{\tau}$ is now known through (2.7). This approach ensures that the vertically integrated ageostrophic velocity satisfies the classic Ekman transport relation.

2.2.1 Wind-Driven Component

The wind-driven component of the stress is given by the first term on the RHS of (2.7), which can be compared to the exact solution for the case where A_v is vertically constant (Stommel, 1960; Bonjean and Lagerloef, 2002),

$$\boldsymbol{\tau(z)} = \boldsymbol{\tau_w} \frac{\sinh\left[\sqrt{\frac{if}{A_v}}(z+h)\right]}{\sinh\left[\sqrt{\frac{if}{A_v}}h\right]}. \tag{2.11}$$

The parallels between the WKB approximation, (2.7), and the solution of the constant-A_v problem (2.11) are apparent, with the leading order modification appearing in the argument of the hyperbolic functions, $\theta(z)$, given by (2.8). This term can be understood as introducing a stretched vertical coordinate system, defined by the integral in (2.8) (Lupini et al., 1975). Accordingly, $h_{Ek}(z) = \sqrt{2A_v(z)/f}$ defines a vertically localized Ekman depth, analogous to the local wavenumber found in WKB solutions to the wave equation (see for example Gill, 1982, section 8.12).

The amplitude of the stress is also modified by vertical variations in viscosity, which appears as a ratio to the 1/4 power. For a slowly vertically decaying A_v, the effect of this term will be apparent only as $z \to -h$, where the ratio of $A_v(z)/A_v(0) \ll 1$. Figure 2.1 compares example vertical profiles of stress and velocity for the case of A_v decaying exponentially with depth, and for constant A_v, to illustrate the modification of the vertical structure arising from retaining a depth-dependent A_v. This depth dependent amplitude term allows the stress amplitude, and hence the ageostrophic velocity, to decay over a different vertical depth scale than the rotation of the stress vector, a feature which is commonly noted in observations but cannot be accommodated in classic Ekman theory (Price et al., 1986; Wijffels et al., 1994; Chereskin, 1995; Price and Sundermeyer, 1999). It is apparent that if A_v is vertically constant in (2.7), the standard solution (2.11), as originally identified by Stommel (1960) in an investigation of the dynamics of the equatorial undercurrent, is immediately recovered.

2.2.2 Inhomogenous Forcing

The second term on the RHS of (2.7) is a Green's function integral, which can accommodate arbitrary vertical structure in both ocean sources of stress, which appear as inhomogenous forcing terms in (2.3), as well as in the profile of $A_v(z)$, subject only to the constraints imposed by the WKB method. The Green's function kernel takes the form of paired Ekman layers above and below interior sources of stress (figure 2.2), which demonstrates how ocean sources of shear in the presence of viscosity drive an ageostrophic frictional response felt throughout the entire boundary layer (Hidaka, 1955; Csanady, 1982). Far from the boundaries the profile of the Green's function is symmetric above and below interior shear, however approaching the boundaries of the domain the shape of the Green's function becomes increasingly asymmetric, and the integral contribution serves to satisfy the boundary conditions (2.4) and (2.5).

The ageostrophic flow associated with several simplified forcings are shown in schematic form in figure 2.3. In the absence of wind-stress, with vertically uniform A_v and ∇b, Ekman layers are generated, both at the surface as well as at the base of the boundary layer, to satisfy the boundary conditions (Bonjean and Lagerloef, 2002). A more physically realistic case is given in figure 2.3b, where a vertically decaying buoyancy gradient gives rise to both a surface Ekman layer, as well as a diffuse interior ageostrophic flow. The strength of the interior portion of the flow, for the situation shown in figure 2.3b, scales as h_{Ek}/h relative to the surface ageostrophic flow, and is therefore often assumed small and neglected. However, we note that this flow is necessary to balance the transport in the surface Ekman layer so as to maintain the classic Ekman transport relation. Further, this flow need not always be small, as illustrated in section 2.3.1 discussing surface wave effects, and hence should be retained. The final panel shows the case of a decaying A_v profile, with constant ∇b. The resulting ageostrophic velocities are similar to those in figure 2.3b, however the associated buoyancy fluxes will differ between the two cases, emphasizing how horizontal fluxes will be a complex function of the spatial structure of both the background fields and A_v, discussed further in section 2.5.2.

The total frictional ageostrophic response thus consists of a directly wind-forced component, as well as an integral over Ekman-like responses to interior shear. Therefore, in order to understand the oceanic response to wind-forcing it is also necessary to understand the ageostrophic frictional response to ocean dynamical processes (Cronin and Kessler, 2009). Recent observational work has emphasized the importance of removing estimates of the geostrophic shear in order to isolate the ageostrophic flow (Chereskin and Roemmich, 1991; Polton et al., 2013; Roach et al., 2015), however the analysis developed here suggests that to fully isolate the wind-driven component of this flow it is also necessary to account for ageostrophic flow driven by the geostrophic shear (section 2.3.2). Further, although we have so far limited the discussion to shear which arises from baroclinic pressure gradients, we note that any other forcing terms in the momentum equations will act in a similar manner, and the case of Stokes shear from surface waves is discussed in section 2.3.1. In order to further illustrate the underlying dynamical mechanisms we now consider two limiting cases representing important sources of shear in the ocean surface boundary layer which admit further simplification of the full solution.

2.3 Limiting Cases

2.3.1 Stokes Shear: $h_s \ll h_{Ek}$

Surface waves modify the oceanic boundary layer in a variety of important ways (Xu and Bowen, 1994; McWilliams et al., 1997; McWilliams and Restrepo, 1999; Sullivan and McWilliams, 2010; Belcher et al., 2012; McWilliams et al., 2012). Here we focus on one particular aspect, termed the Coriolis-Stokes force, which appears as an additional term in the Eulerian momentum equation that arises from rotation acting on the Stokes drift, leading to a tilting of wave-orbitals in the along-crest direction (Polton et al., 2005). The Coriolis-Stokes force has been shown to significantly modify flow in both the very near-surface layer, as well as throughout the entire Ekman layer (Huang, 1979; Jenkins, 1986; Lewis and Belcher, 2004; Polton et al., 2005; Aiki and Greatbatch, 2012; McWilliams et al., 2014).

Equation (2.1) can be re-written to include the Coriolis-Stokes force as,

$$if(\boldsymbol{u}+\boldsymbol{u_s}) = -\frac{1}{\rho_0}\nabla P + \frac{\partial}{\partial z}\left(A_v \frac{\partial \boldsymbol{u}}{\partial z}\right), \tag{2.12}$$

with $\boldsymbol{u_s}$ the Stokes velocity, given by, $\boldsymbol{u_s}(z) = \int_k 2\sigma k \chi(k) e^{2|k|z} \mathrm{d}k$, and where σ is the wave frequency, k the wavenumber vector, and $\chi(k)$ the directional wave spectrum (Huang, 1971). We make the common simplifying assumption that $\boldsymbol{u_s}$ can be treated as a monochromatic wave such that $\boldsymbol{u_s} = U_0 e^{\frac{z}{h_s}} \hat{\boldsymbol{s}}(\boldsymbol{t})$, where $h_s = (2|k|)^{-1}$, and $\hat{\boldsymbol{s}}(\boldsymbol{t})$ is a unit vector in the direction of the waves, which is not necessarily aligned with the local surface wind stress. The wavenumber, k, and amplitude, U_0 are assumed to be known or parameterized. It is important to note that for a time-varying wave field, the Coriolis-Stokes force initially accelerates an 'anti-Stokes' flow (McWilliams and Fox-Kemper, 2013), with transients that decay as $1/ft$ (Lewis and Belcher, 2004). In the steady-state problem, including the Coriolis-Stokes force results in an additional forcing term on the RHS of (2.3), perpendicular to the wave direction, given by $if\rho A_v \partial \boldsymbol{u_s}/\partial z$. This appears in the full solution (2.7) within the Green's function integral, replacing the bracketed term with, $[\rho \nabla b + if\rho \partial \boldsymbol{u_s}/\partial z]$. Hence, both horizontal buoyancy gradients and Stokes shear modify the standard Ekman solution in mathematically identical ways.

In order to provide an asymptotic approximation to (2.7), we can take advantage of the scale separation between the typical depth scale of the surface waves, h_s, which is of order several meters, and h_{Ek} which is of order tens of meters, such that $h_s \ll h_{Ek}$. For simplicity in deriving the given form of (2.13), it is also assumed that $\boldsymbol{\tau_{CS}}(-h) \sim 0$, and $h_{Av} \gg h_{Ek}$ where h_{Av} is the depth scale over which A_v varies, however neither of these assumptions are critical. After repeated integration by parts of (2.7) an asymptotic approximation is given by,

$$\boldsymbol{\tau}(z) \sim [\boldsymbol{\tau}_w - \boldsymbol{\tau}_{CS}(0)] \left(\frac{A_v(z)}{A_v(0)}\right)^{\frac{1}{4}} \frac{\sinh[\theta(z)]}{\sinh[\theta(0)]} + \boldsymbol{\tau}_{CS}(z), \qquad \frac{h_s^2}{h_{Ek}^2} \to 0. \tag{2.13}$$

The surface wave field therefore introduces a Coriolis-Stokes stress,

$$\boldsymbol{\tau}_{CS}(z) = -\rho A_v \frac{\partial \mathbf{u}_s}{\partial z}(1 + i\frac{1}{2}\frac{h_{Ek}^2(z)}{h_s^2})^{-1}, \tag{2.14}$$

which is rotated $(90 + \Lambda)^\circ$ to the left of the wave direction (Northern Hemisphere) where $\Lambda \sim tan^{-1}(h_s^2/h_{Ek}^2)$ (Figure 2.4). This stress modifies the ageostrophic frictional response in two ways. First, the Coriolis-Stokes stress can balance a portion of the applied surface wind stress, leading to a total Ekman layer response which can be considered as forced by an effective stress, given by the first bracketed term on the RHS of (2.13), rather than by the wind stress alone (Polton et al., 2005; McWilliams et al., 2014). Second, the Coriolis-Stokes stress directly affects a layer of depth scale h_s, through the last term on the RHS of (2.13). The vertical divergence of this term, in (2.12), drives near-surface ageostrophic velocities that tend to rotate the surface flow into the down-wave direction (Fig. 2.4b,c). Together these two modifications introduce a boundary layer transport of $-U_0 h_s$, canceling the Lagrangian Stokes transport (see Polton et al., 2005, for a detailed discussion of the frictional Coriolis-Stokes transport).

The results of this section confirm the analysis of Polton et al. (2005), and extend them to an arbitrary vertical structure of A_v, subject to the aforementioned constraints. As discussed by Polton et al. (2005, their section 2c), (2.13) and (2.14) imply that in the limit $h_s^2/h_{Ek}^2 \to 0$, the wave modification to the Eulerian currents can be modeled solely through a modification to the surface boundary condition. The proceeding analysis confirms this result is fully independent of the particular form of vertical mixing, and consequently may be of general use in guiding observational or modeling studies where the Stokes layer is not directly resolved.

2.3.2 Thermal wind shear: $h_{Ek} \ll h_\rho, h_{Av}$

A similar simplification of equation (2.7) can be found for the case of a horizontal buoyancy gradient driving a thermal wind shear in the near-surface layer. We assume that the Ekman

depth is shallow relative to the depth scales over which the horizontal density gradient and A_v vary, ie. $h_{Ek} \ll h_\rho, h_{Av}$. An example of the scales associated with a mesoscale frontal system can be found from observations of the Azores front (Rudnick, 1996), where, using parameters from Nagai et al. (2006), $h_{Ek} \sim 15\,\mathrm{m}$, $h_{Av} \sim 40\,\mathrm{m}$, based on the depth of the transition layer below the mixed layer, and $h_\rho \sim 100\,\mathrm{m}$, based on the depth of the thermocline and the observed geostrophic frontal velocity. This limiting case is marginally valid for these parameter values, and thus can be considered as requiring a fairly idealized frontal configuration (cf. Thomas and Lee, 2005), included largely for the insight it offers into the basic dynamics of (2.7), and for comparison with (2.13).

For simplicity it is also assumed that $A_v \nabla b \to 0$ at $z = -h$. If this assumption is not made the solution requires an additional bottom Ekman layer at $z = -h$ in order to satisfy the bottom boundary condition (2.5), as shown schematically in Fig. 2.3a. Repeated integration by parts of equation (2.7) leads to an asymptotic approximation given by,

$$\boldsymbol{\tau}(z) \sim [\boldsymbol{\tau}_w - \boldsymbol{\tau}_{geo}(0)] \left(\frac{A_v(z)}{A_v(0)}\right)^{\frac{1}{4}} \frac{\sinh[\theta(z)]}{\sinh[\theta(0)]} + \boldsymbol{\tau}_{geo}(z), \qquad \frac{h_{Ek}^2}{h_{\rho,A_v}^2} \to 0. \tag{2.15}$$

Where,

$$\boldsymbol{\tau_{geo}}(z) = \rho A_v \frac{\partial \boldsymbol{u_g}}{\partial z} \left(1 - i h_{Ek}^2(z) \left[\frac{A_v'}{A_v}\frac{\nabla b'}{\nabla b} + \frac{1}{2}\frac{\nabla b''}{\nabla b} + \frac{3}{8}\frac{A_v''}{A_v} + \frac{3}{32}\left(\frac{A_v'}{A_v}\right)^2\right]\right), \tag{2.16}$$

defines the geostrophic stress, with primes denoting vertical differentiation.

Closely paralleling the solution for the Coriolis-Stokes stress, (2.13), the modification of the surface boundary layer stress by horizontal buoyancy gradients also consists of two components. The first is a modification to the Ekman layer, whereby the Ekman response is forced only by that portion of the wind stress that is out of balance with the geostrophic stress, which again can be considered as defining an effective surface stress, given by the first bracketed term on the RHS of equation (2.15) (Thompson, 2000; Nagai et al., 2006;

Cronin and Kessler, 2009). Thus, even in the case of $\boldsymbol{\tau_w} = 0$, thermal wind shear will drive an ageostrophic flow within the Ekman layer, with implications for frontal spin-down (Garrett and Loder, 1981; Csanady, 1982; Thompson, 2000; Thomas and Rhines, 2002), filament frontogenesis (Gula et al., 2014; McWilliams et al., 2015), and near-surface fluxes (Thomas and Ferrari, 2008), discussed in section 2.5.2. It is worth noting that advection of the horizontal buoyancy gradient by the ageostrophic frictional flow can modify the buoyancy gradient and thereby feedback into the Ekman solution, which is discussed in further detail in Thompson (2000), and McWilliams et al. (2015).

The second term on the RHS of equation (2.15) represents the turbulent stress that arises directly from a thermal wind shear in the presence of a viscosity, often termed the geostrophic stress, given by (2.16). The divergence of this term drives a weak flow throughout the entire layer with velocities that scale as h_{Ek}/h relative to the ageostrophic velocity in the Ekman layer, but with a vertically integrated transport that exactly cancels the transport in the Ekman layer driven by the surface geostrophic stress. The definition of geostrophic stress given here, (2.16), differs from that given by previous investigators, who, considering only vertically uniform A_v and ∇b, suggest $\boldsymbol{\tau_{geo}}(z) = \rho A_v \frac{\partial \boldsymbol{u_g}}{\partial z}$. Including vertical structure in these parameters gives rise to four additional terms in the definition of geostrophic stress, bracketed in (2.16), which enter the asymptotic approximation at order $h_{Ek}^2/h_{\rho,A_v}^2$.

These additional terms are imaginary, and thus have the effect of rotating the geostrophic stress vector slightly from the geostrophic shear vector. This is illustrated in figure 2.5, where the geostrophic stress vector is rotated by an angle, λ, which scales as $\lambda \sim tan^{-1}(h_{Ek}^2/h_{\rho,Av}^2)$, or equivalently, $\lambda \sim tan^{-1}(2Ek)$ (figure 2.6). Transport in the Ekman layer, T_{Ek}, is opposed by geostrophic stress driven transport over the full boundary layer depth, T_{BL}. Surface velocity is given by $u_{surf} = u_{Ek}(0) + u_{BL}(0)$, a combination of the Ekman ageostrophic velocity forced by the effective surface stress (u_{Ek}), and an interior ageostrophic velocity forced by the divergence of the geostrophic stress (u_{BL}). The direction of the near-surface frictional flow relative to the buoyancy gradient is consequently a function of both the angle of the geostrophic stress, determined by vertical structure in A_v and ∇b, as well as the ratio

$u_{BL}/u_{Ek} \sim h_{Ek}/h$. As a corollary to this, a latitudinal dependence in λ appears implicitly through the Ekman depth, as $h_{Ek}^2/h_{\rho,Av}^2 \to \infty$ as $f \to 0$, with the geostrophic stress vector becoming increasingly parallel to the buoyancy gradient at low latitudes.

2.4 Frictional Secondary Circulation

The cross front circulation which arises from frictional effects, shown schematically in figure 2.3, acts to spin-down ocean fronts, and sharpen cold filaments, due to buoyancy fluxes associated with the ageostrophic velocities necessary to match the surface boundary condition, (2.4), in the presence of a geostrophic shear (Garrett and Loder, 1981; Thompson, 2000; McWilliams et al., 2015). Further, in the case that $\nabla^2 b \neq 0$, convergences (divergences) of this cross-front ageostrophic circulation will drive negative (positive) vertical velocities in the boundary layer (Garrett and Loder, 1981; Thompson, 2000). These effects have been examined primarily in the context of submesoscale dynamics, where the Rossby number, ϵ, is not small, and hence are generally diagnosed within the context of non-linear models (eg. Nagai et al., 2006). However, recent comparisons with modeled submesoscale eddies and filaments have suggested that vertical velocities in the boundary layer can be accurately diagnosed using this simple linear theory even at high ϵ (Ponte et al., 2013; Gula et al., 2014; McWilliams et al., 2015). At larger spatial scales, similar effects are also suggested in an ocean global climate model (Cronin and Tozuka, 2015). Therefore, friction acting on the baroclinic component of the flow may be important to boundary layer dynamics across a range of spatial scales.

Vertical velocity for the generalized Ekman model is given by the standard relationship,

$$w(x,y,z) = -\hat{k} \cdot \nabla \times \frac{\boldsymbol{\tau}(x,y,z)}{\rho f} + L(x,y), \tag{2.17}$$

where L(x, y) is a constant of vertical integration chosen to fulfill a rigid lid boundary condition. To illustrate how the various components of the full solution enter the calculated vertical velocity we can utilize the simplified definition of stress given by (2.13), and (2.15),

in (2.17), which for a two dimensional configuration, invariant in the y-direction, reduces to,

$$w(x,z) = -\frac{\partial}{\partial x}\left[\mathrm{Im}\left\{\frac{\boldsymbol{\tau_{Eff}}(x)}{\rho f}\left(\frac{A_v(x,z)}{A_v(x,0)}\right)^{\frac{1}{4}}\frac{\sinh\left[\theta(x,z)\right]}{\sinh\left[\theta(x,0)\right]}\right\}\right] - \frac{\partial}{\partial x}\left[\mathrm{Im}\left\{\frac{\boldsymbol{\tau_{Int}}(x,z)}{\rho f}\right\}\right] + L(x). \tag{2.18}$$

The first term on the RHS represents upwelling occurring within the Ekman layer, which is now forced by an effective stress, $\boldsymbol{\tau_{Eff}} = \boldsymbol{\tau_w} - \boldsymbol{\tau_{CS}}(0) - \boldsymbol{\tau_{geo}}(0)$. The second term on the RHS gives the boundary layer vertical velocity arising solely from the gradient of the interior forcing, $\boldsymbol{\tau_{Int}} = \boldsymbol{\tau_{CS}} + \boldsymbol{\tau_{geo}}$. When (2.18) is evaluated at the base of the layer, $z = -h$, it reduces to the classic Ekman upwelling driven solely by the curl of the wind-stress, however, within the layer, both horizontal gradients in the forcing and horizontal gradients of the vertical structure can drive vertical velocities. For the Ekman layer, this can be envisioned as Ekman transport occurring along contours of constant h_{Ek}, which, for a spatially varying A_v, have a vertical component.

Below the surface Ekman layer, where $\tau_{CS}(x,z) \approx 0$, and in the limit of $h_{Ek}^2/h_{\rho,A_v}^2 \to 0$, (2.18) reduces to the scaling given by Garrett and Loder (1981), $w \sim gf^{-2}\rho^{-1}\partial(A_v\partial\rho/\partial x)/\partial x$. Thus, vertical velocity in the boundary layer interior, outside the Ekman layer, is driven by gradients in thermal wind shear and A_v, with order $h_{Ek}^2/h_{\rho,A_v}^2$ modifications due to the gradient of the bracketed terms in (2.16), reflecting the role of the vertical structure of A_v and ∇b in setting the direction of the geostrophic stress vector (section 2.3.2, figure 2.6). Approaching the surface, vertical velocity decays exponentially over an Ekman layer of depth scale h_{Ek}, with additional near-surface vertical velocities in a thin layer of depth scale h_s driven by the Coriolis-Stokes stress.

To illustrate the secondary circulation that arises from the balance (2.1), we examine an idealized front in the x-z plane (200 km width, h=500 m), based on an approximation of the Frontal Air-Sea Interaction Experiment (FASINEX) data (Pollard and Regier, 1992), similar to Thompson (2000). We set $\boldsymbol{\tau_w} = 0$ and $\boldsymbol{\tau_{CS}} = 0$ as the solution is linear and these effects

are simply additive. The buoyancy in this model is given by,

$$b(x,z) = \frac{1}{2} b_f \tanh\left[\frac{\hat{z} - \alpha(\hat{x} - x_0)^3 - z_0}{d_0}\right] + \frac{1}{2} b_b \tanh\left[\frac{\hat{z} - z_0}{d_1}\right], \tag{2.19}$$

with values of parameters given in Table 1 and the hat notation indicating non-dimensionalized coordinates ranging from 0 to 1. Values of A_v are based on the approximation used in McWilliams et al. (2015), designed to be broadly consistent with KPP (Large et al., 1994). This is used simply to illustrate several general features of the solution that arise from horizontal and vertical structure in mixing across a frontal region, rather than provide an absolutely accurate diagnostic, and the qualitative discussion that follows is not sensitive to the detailed particulars of our choice of A_v.

$$A_v(x,z) = A_{v0} G(\zeta) \frac{\hat{h}(\hat{x})}{h_0} + A_{vb}, \quad \zeta = -\frac{\hat{z}}{\hat{h}(x)}, \tag{2.20}$$

$$G(\zeta) = \frac{27}{4}(1 + \zeta_0^2)(\zeta_0 + \zeta)(1 - \zeta)^2, \quad \zeta \leq 1, \tag{2.21}$$

$$G(\zeta) = 0, \quad \zeta > 1. \tag{2.22}$$

G has a maximum value of 1 in the boundary layer, ζ_0 is a small parameter introduced to avoid a singularity at $z = 0$, and $\hat{h}$ is the surface boundary layer depth, taken here as,

$$\hat{h}(x) = h_0 + \delta_h \left(\tanh\left[\frac{\alpha(\hat{x} - x_0)^3}{d_0}\right] - \frac{1}{2}\right). \tag{2.23}$$

All parameter values for equations (2.19-2.23) are given in Table 1. Figure 2.7 shows the structure of the idealized front, and the eddy viscosity, along with the associated along front geostrophic flow, implying $\epsilon \sim 0.05$. We further assume $w = 0$ at $z = 0$ (rigid lid), and define an ageostrophic cross-front streamfunction such that $(u_{ag}, w) = (\psi_z, -\psi_x)$. Using the meridional momentum equation, Im[Eq. (2.1)], gives

$$\psi = \frac{1}{\rho f} \tau^y(x,z). \tag{2.24}$$

The secondary overturning circulation arising from the geostrophic stress is found numerically, and shown in figure 2.7. This is a thermally direct circulation, with a counter-clockwise sense of rotation, that tends to tilt the front and restratify the near-surface (Thompson, 2000). Downwelling velocities on the dense side of the front are stronger than the upwelling on the buoyant side of the front, consistent with previous findings (Samelson, 1993; Thompson, 2000). Streamlines are closed, indicating zero vertically integrated horizontal transport, as required to maintain the classic Ekman transport. This is a general result that does not depend on the frontal configuration. Note however that although the vertically integrated horizontal transport is zero, the associated fluxes need not be zero, as discussed further in section 2.5.2. Further, the vertical buoyancy flux associated with the secondary overturning circulation can be non-zero (McWilliams et al., 2015), and hence may play a role in the general circulation through vorticity stretching of the interior.

To illustrate the importance of spatial variability in A_v, we decompose the total vertical velocity field (figure 2.8a), w_{total}, into vertical velocities due to the gradient in the forcing ($\nabla^2 b$), which we designate $w_{forcing}$, and the remainder which is a function only of the spatial structure in A_v, which we designate w_{Av}, as discussed in relation to (2.18). For the particular frontal configuration examined here w_{Av} is $\sim 25\%$ of w_{total}. However, locally near the base of the turbulent boundary layer (Fig 2.8, dashed line) w_{Av} can be the dominant term, and hence may be of particular importance for vertical fluxes into the near-surface layer. For a geostrophic stress, the ratio of vertical velocities is given by,

$$\frac{w_{Av}}{w_{forcing}} \sim \frac{L_{forcing}}{L_{Av}}, \tag{2.25}$$

where L indicates the relevant horizontal length scales. Observations suggest that horizontal length scales over which vertical mixing varies are comparable to frontal features (Dewey and Moum, 1990; Nagai et al., 2006), and hence these effects may be first order in determining the vertical velocity in the boundary layer. A similar scaling holds within the Ekman layer, where for a surface wind stress aligned orthogonal to a horizontal gradient in A_v, the ratio

of vertical velocities at $z = -h_{Ek}$ is,

$$\frac{w_{Av}}{w_{forcing}} \sim \frac{L_{forcing}}{4L_{Av}}. \tag{2.26}$$

2.5 Discussion and Further Implications

The solutions presented here build upon prior work by allowing vertical variation in A_v, as well as realistic structure in ocean fields, such as ∇b and the Coriolis-Stokes force. Examination of the solutions (2.7, 2.13, 2.15), suggests many ways in which including more physical realism in the problem parameters can modify the expected ageostrophic flow, however to further motivate the importance of this added complexity, we first consider scaling arguments relating the importance of geostrophic stress and Coriolis-Stokes stress to wind stress. The global distribution of these fields are then estimated using a combination of model output and reanalysis data. Finally, we comment briefly on the importance of these modifications to determining horizontal fluxes in the boundary layer.

2.5.1 Scaling and Geographic Distribution

The boundary conditions utilized here ensure that the classic Ekman transport relation is maintained, even in the presence of ocean sources of stress. However, as demonstrated in Section 2.2, ocean sources of stress can greatly modify the vertical structure of currents, and hence are fundamental to understanding boundary layer dynamics. Determining the magnitude of both the geostrophic stress and the Coriolis-Stokes stress depends critically on the value of A_v, which complicates their determination from observations. However, at low frequencies, variability in near-surface A_v may be controlled by variability in the surface wind stress (Wenegrat et al., 2014). Taking $h_{Ek} \sim u^*/f$ (Caldwell et al., 1972), where $u^* = \sqrt{\tau_w/\rho}$, gives $A_v \sim u^{*2}/f$, and hence the ratio of the geostrophic stress to the surface wind stress can be scaled as,

$$\gamma_{GEO} = \frac{\tau_{geo}}{\tau_w} \sim \frac{\nabla b}{f^2}. \tag{2.27}$$

The direct proportionality of γ_{GEO} to ∇b, and independence from τ_w, highlights how the geostrophic stress can be expected to be a ubiquitous forcing of ageostrophic flow at sharp frontal features, and consequently may be fundamental for understanding horizontal heat flux at buoyancy fronts. The f^{-2} dependence indicates a rapid increase at low latitudes. Further, utilizing the stratified Ekman depth scaling, $h_{Ek} \sim u^*/\sqrt{Nf}$ (Pollard et al., 1973), in (2.27) gives $\gamma_{GEO} \sim Bu$, where $Bu = NH/fL$ is the Burger number, defined such that $b \sim N^2 H$. Determination of Bu is thus dependent on the geometry of the particular front being considered, however, for many oceanic flows observations suggest $Bu \sim O(1)$, implying $\gamma_{GEO} \sim O(1)$ (Nagai et al., 2006; Boccaletti et al., 2007).

The Coriolis-Stokes stress can be scaled relative to the surface wind stress as,

$$\gamma_{CS} = \frac{\tau_{CS}}{\tau_w} \sim U_0 h_s \frac{\rho f}{\tau_w} \sim La^{-2} \frac{h_s}{h_{Ek}}. \tag{2.28}$$

Therefore, γ_{CS} is proportional to the Stokes transport divided by the wind-driven Ekman transport (McWilliams and Restrepo, 1999; Polton et al., 2005). Alternatively, this can be rewritten using the turbulent Langmuir number, $La = (u^*/U_0)^{1/2}$, which scales the ratio of wind forced production of turbulent kinetic energy (TKE) to the wave forced production of TKE (McWilliams et al., 1997; Grant and Belcher, 2009), with typical values of 0.2-0.5 (Smith, 1992; Belcher et al., 2012). This suggests that $\gamma_{CS} \sim O(1)$ for h_s/h_{Ek} of 0.04 - 0.25.

To form estimates of the global distributions of γ_{GEO} and γ_{CS} a combination of reanalysis data and model output is utilized. The total Stokes transport is found from the WaveWatch III (WWIII) model, reported every 6 hours on a 0.5° grid (Rascle et al., 2008; Rascle and Ardhuin, 2013). For consistency with the WWIII model forcing, we utilize NCEP Climate Forecast System Reanalysis (CFSR) wind stress, temperature and salinity at 5 m, and horizontal currents at 5 and 15 m depth (Saha et al., 2006). To estimate the geostrophic stress we calculate buoyancy gradients from monthly 5 m temperature and salinity (0.5° resolution), and then infer approximate monthly values of A_v using the surface boundary condition, $A_v = \tau_w(\rho \partial u/\partial z)^{-1}$, with the near-surface shear magnitude approximated using CFSR ve-

locities at 5 and 15 m, $\partial u/\partial z \sim |\boldsymbol{u}(-5) - \boldsymbol{u}(-15)|/10$. Alternate parameterizations of A_v were tested, including wind-stress only parameterizations (Wenegrat et al., 2014) and bulk Richardson number closures (Pollard et al., 1973), and found to give similar results (not shown here). Monthly values of the Stokes transport and τ_{geo} over the period 2001-2011 are then used to form climatologies of γ_{GEO} and γ_{CS}.

Figures 2.9 and 2.10 show the global seasonal climatology of γ_{GEO} and γ_{CS}, respectively. The dependence on latitude through the Coriolis frequency is apparent in both quantities, with γ_{GEO} peaking at low latitudes, and γ_{CS} dominating at higher latitudes (figure 2.11). Regional variability is also evident, with γ_{GEO} enhanced in boundary currents, along the equatorward edges of the subtropical gyres, and through much of the Indian ocean and eastern subtropical Pacific. These parameterized results can be compared to estimates derived from model output and alternate parameterizations of A_v, which indicate similar spatial patterns (Chu, 2015; Cronin and Tozuka, 2015).

In the zonal average, and temporal average, γ_{CS} becomes larger than γ_{GEO} poleward of 15° (figures 2.10 and 2.11), following a spatial pattern that in large part reflects the variability in Stokes transport (McWilliams and Restrepo, 1999). This latitudinal pattern may also reflect the effect of the coarse resolution products utilized here on estimating γ_{GEO}, as the first baroclinic Rossby radius at 15° is $\sim 100\,\mathrm{km}$ (Chelton et al., 1998), which is close to the resolved meridional Nyquist wavelength, and hence ∇b may be underestimated at higher latitudes. Wide swaths of the world oceans have $\gamma_{CS} \sim 0.25$, emphasizing how important these effects may be for Ekman layer currents. Intensification of γ_{CS} in the southern ocean is also evident. In the Northern Hemisphere there is a general enhancement of γ_{CS} in the eastern side of the ocean basins, with seasonal variability in both extent and magnitude, resulting from enhanced Stokes transport associated with increased wintertime wind-forcing.

The relative influences of the geostrophic stress and the Coriolis-Stokes stress can be considered using the joint probability density function (PDF) of the monthly estimates of γ_{GEO} and γ_{CS}, evaluated between $5° - 73.5°$ from 2001-2011 (figure 2.12). Consistent with the spatial maps, the PDF has a broad peak at $\gamma_{CS} \sim 0.1 - 0.25$ with negligible γ_{GEO}. However,

the distribution of γ_{GEO} is long-tailed, reflecting its spatial and temporal inhomogeneity, evident in comparing an example month (figure 2.13) and the climatological maps (figure 2.9). Considering the total relative change in the effective surface stress arising from both the geostrophic stress and the Coriolis-Stokes stress, $\gamma_T = \gamma_{GEO} + \gamma_{CS}$, 36% of all points have $\gamma_T > 0.25$. Together the estimates presented above, while only a rough approximation, suggest that surface waves will be of $O(1)$ importance for much of the extra-tropics, while baroclinic pressure gradients will dominate at low latitudes, in frontal systems, and potentially over shorter timescales, and smaller spatial scales, than resolved here, specifically at the submesoscale, where geostrophic stress effects have been demonstrated to significantly modify the ageostrophic flow (Ponte et al., 2013; Gula et al., 2014; McWilliams et al., 2015).

2.5.2 Horizontal Fluxes

The proceeding analysis, and theory, highlights how ocean sources of stress can be expected to modify the frictional response within the near-surface layer, affecting the magnitude, direction, and vertical profile of the ageostrophic flow. These modifications to the ageostrophic velocity can often be approximated using the concept of an effective stress, τ_{Eff} (section 2.3), leading to a modified Ekman velocity scale of, $u_{Ek} \sim \tau_{Eff}/(\rho f h_{Ek})$. This has wide-ranging implications for horizontal advective fluxes, where for example, the geostrophic stress will always enhance heat flux down the buoyancy gradient relative to the classic Ekman solution, as well as for other dynamically important quantities such as the wind-work on the total ageostrophic flow, $\boldsymbol{\tau_w} \cdot \boldsymbol{u_{Ek}}$, which will be reduced for winds aligned with the surface frontal jet (down-front winds), and enhanced for winds aligned against the frontal jet (up-front winds).

A brief example, which highlights the role of vertical structure in A_v, is given by considering the differential horizontal buoyancy flux across the surface Ekman layer, which can change the stratification, and hence the potential vorticity (PV), of the near surface layer (Thomas and Ferrari, 2008). A scaling for the frictional flux of the vertical component of PV due to a surface wind stress aligned orthogonally to a horizontal buoyancy gradient is

given by (Thomas, 2005; Thomas and Ferrari, 2008),

$$J_z^F \sim \frac{\tau_w}{\rho h_{Ek}} \nabla b. \tag{2.29}$$

However, if A_v is allowed to vary vertically, with depth scale h_{Av}, this scaling is modified to become,

$$J_z^F \sim \frac{\tau_w}{\rho h_{Ek}} \nabla b \left(1 + \frac{h_{Ek}}{4h_{Av}}\right). \tag{2.30}$$

This relationship is shown in figure 2.14, for a wind stress aligned with the front, and an exponential A_v profile that decreases (increases), $h_{Av} > 0$ ($h_{Av} < 0$), with depth. As $|h_{Av}|$ approaches h_{Ek} the surface cross-front current is enhanced (reduced) for $h_{Av} > 0$ ($h_{Av} < 0$), modifying the frictional PV flux. A similar result can be easily derived for the influence of vertical structure of A_v on the frictional PV flux associated with the frontal spin down by the geostrophic stress (Thomas and Ferrari, 2008). Thus, the vertical structure of mixing is linked to the flux of vertical potential vorticity through its effect on the differential horizontal advection of buoyancy.

A conceptual example of how this might affect the ocean boundary layer is is found by considering the near-surface response to up-front and down-front winds. Down-front winds advect dense water over light water, leading to gravitational instability, whereas up-front winds advect light water over dense, enhancing stratification (Thomas and Lee, 2005). Making the idealization that down-front winds lead to a well-mixed layer with $A_v \sim$ constant, whereas up-front winds lead to a stratified near-surface layer with A_v decreasing with depth, would imply the existence of an asymmetry in PV fluxes between the two cases. Consequently, for the same wind stress and buoyancy gradient magnitudes, wind-driven frictional PV fluxes may be enhanced in up-front wind conditions relative to down-front winds, providing a possible alternative route to the creation of positively skewed PV distributions (Thomas, 2007).

2.6 Summary

In this manuscript we present an approximate solution to the generalized Ekman (Cronin and Kessler, 2009), or Turbulent Thermal Wind (Gula et al., 2014; McWilliams et al., 2015), balance. While this theory omits many aspects of boundary layer physics that are likely to be active in the real ocean, the simplicity and generality of the solution provides a useful tool for gaining insight into the underlying dynamics beyond that available from numerical methods. The full solution, (2.7), given in terms of an integral over a Green's function, can be applied quite generally to a variety of sources of near-surface shear, and further allows for arbitrary vertical structure in A_v, subject to the constraints imposed by the WKB method. Many existing modified Ekman theories can thus be considered as particular cases of this solution, providing a framework for comparing their effects on ageostrophic ocean currents.

Two important aspects of surface layer dynamics which are not as readily accommodated in this framework are time-dependence, and non-linearity. Observations suggest significant diurnal variatiability of near-surface shear (Price et al., 1986; Schudlich and Price, 1998; Cronin and Kessler, 2009; Smyth et al., 2013; Wenegrat and McPhaden, 2015a), which has been suggested as an explanation of observed discrepancies with classic Ekman theory (Price and Sundermeyer, 1999). However, analysis of near-surface velocity observations appears to suggest that some of the observed features which have been used to argue for the role of time-variability, such as a flattened spiral, can also be very well explained by alternate mechanisms that do not invoke time-dependence (Lewis and Belcher, 2004; Polton et al., 2005; Cronin and Kessler, 2009). Disentangling these effects using observations is further complicated by measurement challenges, particularly for moored observations which can be biased by surface waves (Rascle and Ardhuin, 2009). A focus of future work should be clarifying the relative contributions of, and interactions between, the diverse sources of near-surface ageostrophic flow.

Non-linear effects may be of particular importance in examining sharp horizontal buoyancy gradients (Stern, 1965; Niiler, 1969; Thomas and Rhines, 2002; Mahadevan and Tandon,

2006). However, a range of modeling efforts which include more complete physics indicate that the basic dynamical mechanisms discussed here continue to be of first order importance in the boundary layer, even at high ϵ (Thompson, 2000; Nagai et al., 2006; Ponte et al., 2013; Gula et al., 2014; McWilliams et al., 2015). We also note that the work of Wu and Blumen (1982), and Tan (2001), can be considered as a blueprint for how the semi-geostrophic momentum approximation could be incorporated into the solution given here.

Examining two limiting cases, the first for Stokes shear of shallow depth relative to h_{Ek}, and the second for a front much deeper than h_{Ek}, reveals the key underlying dynamics. Ocean sources of shear, in the presence of viscosity, act as sources of stress. These ocean sources of stress are, as a first approximation, independent of the surface wind stress, and are capable of driving their own ageostrophic flow, including creating a surface Ekman layer. The equivalency of the closed form solutions for the two limiting cases emphasizes how robust this interpretation of the underlying dynamics is, suggesting the same interpretation holds for the more general Green's function solution (2.7), and highlighting a previously unnoted connection between the frictional effects of surface waves and fronts.

The solutions presented here are unique in their ability to incorporate arbitrary vertical structure in A_v, which is motivated physically by modeling and direct turbulence measurements (Zikanov et al., 2003; Kirincich, 2013; Soloviev and Lukas, 2014), and is shown here to lead to modifications of both horizontal and vertical flows. Improved understanding of the spatial variability of mixing is key to understanding and parameterizing these effects on boundary layer flow. Finally, it should be emphasized that the various dynamical processes discussed here should not be considered as the addition of new parameters to the Ekman problem, but rather as fundamental components of the frictional response of the ocean boundary layer, whose influence may be of the same order of magnitude as the surface wind stress throughout large portions of the global oceans. The total frictional ageostrophic response is a combination of a response to the surface wind, as in the classic Ekman theory, and a response to ocean sources of shear.

2.7 Appendix A: Derivation

Let $A_v(z) = A_{v0}\psi(z)$, then, after non-dimensionalizing (2.3) as discussed in section 2.2, we have,

$$Ek\boldsymbol{\tau}'' - \frac{i}{\psi(z)}\boldsymbol{\tau} = \boldsymbol{\xi(z)}, \tag{2.31}$$

$$\boldsymbol{\tau}(0) = \boldsymbol{\tau_w}, \tag{2.32}$$

$$\boldsymbol{\tau}(-h) = 0, \tag{2.33}$$

where primes indicate vertical derivatives and all variables are non-dimensional unless otherwise noted. The RHS of (2.31) is given in terms of a generic inhomogeneous forcing function, $\boldsymbol{\xi}(z)$, which could arise from geostrophic shear or Coriolis-Stokes shear as discussed in section 2.3. Solving first for the homogenous solution, and making the WKB assumption,

$$\tau \propto e^{(S_0+S_1\delta+S_2\delta^2+\ldots)/\delta}, \tag{2.34}$$

gives,

$$Ek\left[\frac{S_0''}{\delta} + \frac{S_0'^2}{\delta^2} + \frac{2S_0'S_1'}{\delta} + S_1'' + S_1'^2\right]\boldsymbol{\tau} - \frac{i}{\psi(z)}\boldsymbol{\tau} = 0. \tag{2.35}$$

The distinguished limit for the parameter δ is therefore, $\delta \sim Ek^{\frac{1}{2}}$, and the balance conditions are given by,

$$O(\delta^{-2}): \quad S_0' = \pm\sqrt{\frac{i}{\psi(z)}}, \tag{2.36}$$

$$O(\delta^{-1}): \quad S_1' = -\frac{S_0''}{2S_0'}. \tag{2.37}$$

Taking the positive root of S_0' gives,

$$S_0 = \sqrt{i}\int_{-h}^{z}\psi(Z)^{-\frac{1}{2}}\,\mathrm{d}Z, \tag{2.38}$$

and,

$$S_1 = \frac{1}{4}\log\psi(z). \tag{2.39}$$

A similar argument is followed for the negative root, giving the two solutions to the ODE, which dimensionally are given by,

$$\boldsymbol{\tau}(z) = C_1 A_v(z)^{\frac{1}{4}} e^{\theta(z)} + C_2 A_v(z)^{\frac{1}{4}} e^{-\theta(z)}, \tag{2.40}$$

where,

$$\theta(z) = \sqrt{if}\int_{-h}^{z} A_v(Z)^{-\frac{1}{2}}\,\mathrm{d}Z. \tag{2.41}$$

For the WKB approximation to hold, two conditions must be satisified (Bender and Orszag, 1978),

$$\frac{Ek^{\frac{1}{2}}S_1}{S_0} \ll 1, \qquad Ek^{\frac{1}{2}} \to 0, \tag{2.42}$$

$$Ek^{\frac{1}{2}}S_2 \ll 1, \qquad Ek^{\frac{1}{2}} \to 0, \tag{2.43}$$

discussed further in Appendix B.

Variation of parameters gives the inhomogeneous portion of the solution,

$$\boldsymbol{\tau_p} = -y_1\int \frac{y_2\xi(z)}{W(y_1,y_2)}\,\mathrm{d}z + y_2\int \frac{y_1\xi(z)}{W(y_1,y_2)}\,\mathrm{d}z. \tag{2.44}$$

Where W is the Wronskian,

$$W(y_1,y_2) = y_1y_2' - y_2y_1' = -2\sqrt{if}. \tag{2.45}$$

Thus,

$$\boldsymbol{\tau_p} = A_v(z)^{\frac{1}{4}}e^{\theta(z)}\int \frac{e^{-\theta(z)}A_v(z)^{\frac{1}{4}}\xi(z)}{2\sqrt{if}}\,\mathrm{d}z - A_v(z)^{\frac{1}{4}}e^{-\theta(z)}\int \frac{e^{\theta(z)}A_v(z)^{\frac{1}{4}}\xi(z)}{2\sqrt{if}}\,\mathrm{d}z. \tag{2.46}$$

Changing the limits of integration gives,

$$\boldsymbol{\tau_p} = \int_0^z \frac{sinh\left[\theta(z) - \theta(s)\right] A_v(z)^{\frac{1}{4}} A_v(s)^{\frac{1}{4}} \xi(s)}{\sqrt{if}} \, \mathrm{d}s. \tag{2.47}$$

So, the total solution, before application of the boundary conditions, is given by,

$$\boldsymbol{\tau_t}(z) = C_1 A_v(z)^{\frac{1}{4}} e^{\theta(z)} + C_2 A_v(z)^{\frac{1}{4}} e^{-\theta(z)} + \int_0^z \frac{sinh\left[\theta(z) - \theta(s)\right] A_v(z)^{\frac{1}{4}} A_v(s)^{\frac{1}{4}} \xi(s)}{\sqrt{if}} \, \mathrm{d}s. \tag{2.48}$$

Applying the surface BC gives,

$$\boldsymbol{\tau_w} = C_1 A_v(0)^{\frac{1}{4}} e^{\theta(0)} + C_2 A_v(0)^{\frac{1}{4}} e^{-\theta(0)}, \tag{2.49}$$

therefore,

$$\begin{aligned} \boldsymbol{\tau_t}(z) = 2C_1 A_v(z)^{\frac{1}{4}} e^{\theta(0)} sinh\left[\theta(z) - \theta(0)\right] + \boldsymbol{\tau_w} \left(\frac{A_v(z)}{A_v(0)}\right)^{\frac{1}{4}} e^{\theta(0) - \theta(z)} \\ + \int_0^z \frac{sinh\left[\theta(z) - \theta(s)\right] A_v(z)^{\frac{1}{4}} A_v(s)^{\frac{1}{4}} \xi(s)}{\sqrt{if}} \, \mathrm{d}s. \end{aligned} \tag{2.50}$$

The lower BC gives,

$$\begin{aligned} 0 = 2C_1 A_v(-h)^{\frac{1}{4}} e^{\theta(0)} sinh\left[\theta(-h) - \theta(0)\right] + \boldsymbol{\tau_w} \left(\frac{A_v(-h)}{A_v(0)}\right)^{\frac{1}{4}} e^{\theta(0) - \theta(-h)} \\ + \int_0^{-h} \frac{sinh\left[\theta(-h) - \theta(s)\right] A_v(-h)^{\frac{1}{4}} A_v(s)^{\frac{1}{4}} \xi(s)}{\sqrt{if}} \, \mathrm{d}s. \end{aligned} \tag{2.51}$$

Following Hidaka (1955), we multiply equation (2.50) by $sinh[-\theta(0)]$, equation (2.51) by

$-\left(\frac{A_v(z)}{A_v(-h)}\right)^{\frac{1}{4}} sinh[\theta(z)-\theta(0)]$, and add them, giving,

$$\boldsymbol{\tau}(z) = \boldsymbol{\tau_w}\left(\frac{A_v(z)}{A_v(0)}\right)^{\frac{1}{4}} \frac{\sinh\left[\theta(z)\right]}{\sinh\left[\theta(0)\right]} + \int_0^z \frac{\sinh\left[\theta(z)-\theta(s)\right]\sinh[\theta(0)]\xi(s)A_v(s)^{\frac{1}{4}}A_v(z)^{\frac{1}{4}}}{(if)^{\frac{1}{2}}\sinh[\theta(0)]}\,\mathrm{d}s - \int_0^{-h} \frac{\sinh\left[\theta(z)-\theta(0)\right]\sinh[\theta(s)]\xi(s)A_v(s)^{\frac{1}{4}}A_v(z)^{\frac{1}{4}}}{(if)^{\frac{1}{2}}\sinh[\theta(0)]}\,\mathrm{d}s. \quad (2.52)$$

This can be re-written as,

$$\boldsymbol{\tau}(z) = \boldsymbol{\tau_w}\left(\frac{A_v(z)}{A_v(0)}\right)^{\frac{1}{4}} \frac{\sinh\left[\theta(z)\right]}{\sinh\left[\theta(0)\right]} + \int_{-h}^0 G(z,s)\xi(s)\,\mathrm{d}s, \quad (2.53)$$

$$\theta(z) = \sqrt{if}\int_{-h}^z A_v(Z)^{-\frac{1}{2}}\,\mathrm{d}Z, \quad (2.54)$$

$$G(z,s) = \begin{cases} \frac{\sinh[\theta(z)]\sinh[\theta(s)-\theta(0)]A_v(s)^{\frac{1}{4}}A_v(z)^{\frac{1}{4}}}{\sinh[\theta(0)]\sqrt{if}} & \text{if } s > z \\ \frac{\sinh[\theta(s)]\sinh[\theta(z)-\theta(0)]A_v(s)^{\frac{1}{4}}A_v(z)^{\frac{1}{4}}}{\sinh[\theta(0)]\sqrt{if}} & \text{if } s < z. \end{cases} \quad (2.55)$$

2.8 Appendix B: Accuracy of approximate solution

The validity of the physical-optics WKB approximation requires the criteria (2.42) and (2.43) be satisified (Bender and Orszag, 1978). The relative error in the approximation will then be a function of the small parameter $\delta \sim Ek^{1/2}$ and the first ignored term, $S2$, in (2.34), which involves both first and second derivatives of A_v. Thus, errors will be a function of the Ekman number, Ek, as well as the particular vertical structure of A_v. Anecdotally, the WKB solution (2.7) has proven extremely accurate across a wide-range of vertical structures of A_v, and values of Ek, considered in developing the model (see also Grisogono, 1995; Berger and Grisogono, 1998). However, to better illustrate the accuracy of the approximate solution we consider the relative error associated with 3 idealized forms of A_v (figure 2.8).

Case I is a simple exponentially decaying profile,

$$A_v(z) = A_{v0}e^{\frac{\hat{z}}{0.125}}, \quad (2.56)$$

chosen for its analytic simplicity, and consistency with observations (Peters et al., 1988; Dillon et al., 1989). Case II is a linearly decaying profile,

$$A_v(z) = A_{v0}\left(1 + \frac{\hat{z}}{1+\mu}\right), \tag{2.57}$$

where μ is a small value added to avoid a singularity at $z = -h$. Case III is a modified Gaussian profile (Parmhed et al., 2005),

$$A_v(z) = A_{v0}\phi\hat{z}e^{-\frac{1}{2}(\frac{\hat{z}}{0.25})^2} + \mu, \tag{2.58}$$

where, $\phi = 4e^{\frac{1}{2}}$, which approximates the polynomial profile of O'Brien (1970), and μ is a small parameter added for computational regularity (eg. McWilliams and Huckle, 2006). The results of the error analysis are not dependent on the value of μ, which we take to be $\mu = 10^{-6}\,\mathrm{m^2\,s^{-1}}$. This profile violates (2.42) in a thin layer near $\hat{z} = 0$, where $A_v \to 0$, and hence the WKB solution must be patched to an inner solution valid in this thin near-surface region. The depth at which the patching occurs, z_p, can be determined following Parmhed et al. (2005) as,

$$z_p = -\frac{1}{4}\left[W\left(\frac{2}{\sqrt{\phi}}\right)\right]^2, \tag{2.59}$$

where W is the Lambert W function (Corless et al., 1996). For the values used here, $z_p = -0.06$. For the case of a surface wind stress, an appropriate inner solution is determined by assuming a linearized eddy viscosity, $A_{vl}(\hat{z}) = \phi|\hat{z}| + \mu$, valid for $\hat{z} \to 0$, giving (Madsen, 1977),

$$\boldsymbol{\tau}_{Inner} = \boldsymbol{\tau_w}\frac{\sqrt{\beta(z)}}{\sqrt{\beta(0)}}\frac{K_1\left(2\sqrt{\beta(z)}\right)}{K_1\left(2\sqrt{\beta(0)}\right)}, \tag{2.60}$$

where $\beta(z) = \frac{if A_{vl}(\hat{z})}{\phi^2}$, and K_1 is the first-order modified Bessel function of the second kind (Abramowitz and Stegun, 1964). This solution is then patched to the WKB solution at $\hat{z} = z_p$.

Determining the appropriate patched solution for the inhomogeneous problem is beyond the scope of the present work. Thus, for assessing the error associated with geostrophic stress forcing we make the simplifying approximation of applying the surface boundary condition directly to the WKB solution at z_p, similar to the introduction of a roughness length scale (Madsen, 1977), and equivalent in the error analysis to the requirement that any inner solution be exact. The validity of this approximation is supported by the accuracy of the patched homogeneous solution (figure 2.8), which suggests that an appropriate inner solution for the inhomogeneous problem could be identified using variation of parameters (section 2.7).

To form an estimate of the relative error as a function of Ek, WKB solutions (2.7) are compared to numeric solutions, found using a shooting method, and the normalized maximum error identified in each vertical profile,

$$\widehat{\tau_{err}}(Ek) = \frac{max\left\{|\tau_{WKB}(z,Ek) - \tau_{num}(z,Ek)|\right\}}{max\left\{|\tau_{num}(z,Ek)|\right\}}. \tag{2.61}$$

Results are plotted in figure 2.8, for the patched-solution with wind stress forcing (top), and solutions forced by a vertically uniform buoyancy gradient (bottom). Also plotted for reference is the value of the small parameter, $\delta \sim Ek^{1/2}$. Errors are generally small, and, for $Ek \leq 10^{-1}$, the only case with relative errors exceeding 5% is the modified exponential profile, (2.58). The errors associated with this profile are strongly dependent on the choice of patching depth, z_p, rather than the overall vertical structure, as can be anticipated through the logarithmic singularity evident in (2.42). Hence caution is required in applying (2.7) in cases where $A_v \to 0$ near a boundary.

Table 2.1: Parameters for equations (2.19-2.23).

Parameter	*Value*	Physical Interpretation
b_f	$-0.6\frac{g}{\rho_0}$	Buoyancy change across front
b_b	$\frac{b_f}{2}$	Buoyancy change across thermocline
α	-1.185	Horizontal scaling factor
z_0	0.75	Vertical position
x_0	1	Horizontal position
d_0	0.125	Horizontal scale
d_1	0.125	Vertical scale
f	$6.88 \times 10^{-5} s^{-1}$	Coriolis frequency
A_{v0}	$3 \times 10^{-2} m^2 s^{-1}$	Eddy viscosity magnitude
A_{vb}	$1 \times 10^{-4} m^2 s^{-1}$	Background viscosity
h_0	0.84	Turbulent boundary layer depth
δ_h	0.05	Across front change in boundary layer depth
ζ_0	5×10^{-3}	Regularization constant

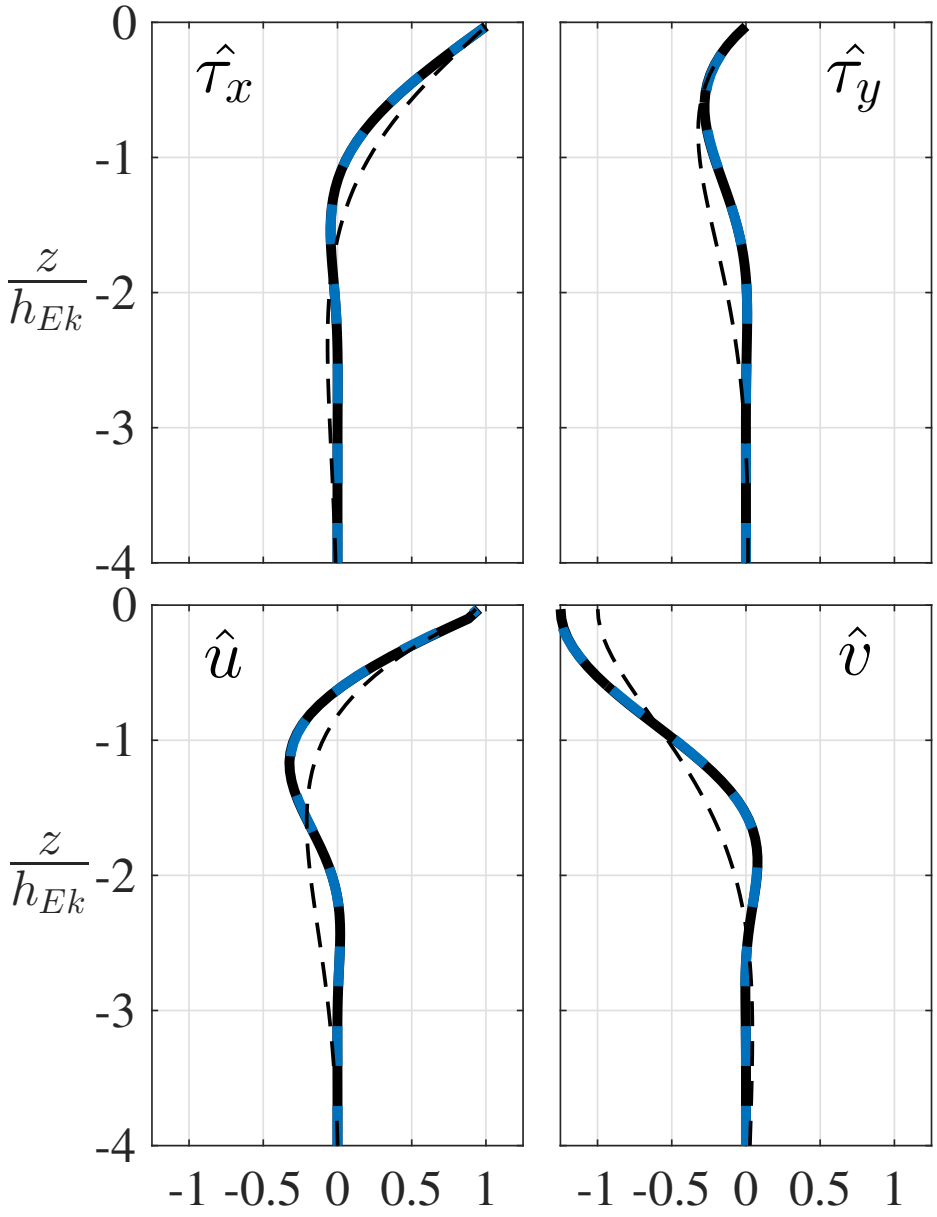

Figure 2.1: Example profiles of stress and velocity for an exponentially decaying eddy viscosity, $A_v = A_{v0} e^{\frac{z}{h_{Ek}}}$ for numeric (solid black) and WKB solution given by equation (2.7) (dashed blue), and for constant eddy viscosity $A_v = A_{v0}$ (thin dashed black). Top row, stress profiles, normalized by the surface wind stress value, $\hat{\boldsymbol{\tau}} = \boldsymbol{\tau}(z)/|\tau_w|$. Bottom row, velocity profiles, normalized by, $\hat{\boldsymbol{u}} = \boldsymbol{u}(z)\,|\tau_w/(\rho f h_{Ek}(0))|^{-1}$. The WKB solution overlaps the numerical solution to within the thickness of the plotted line.

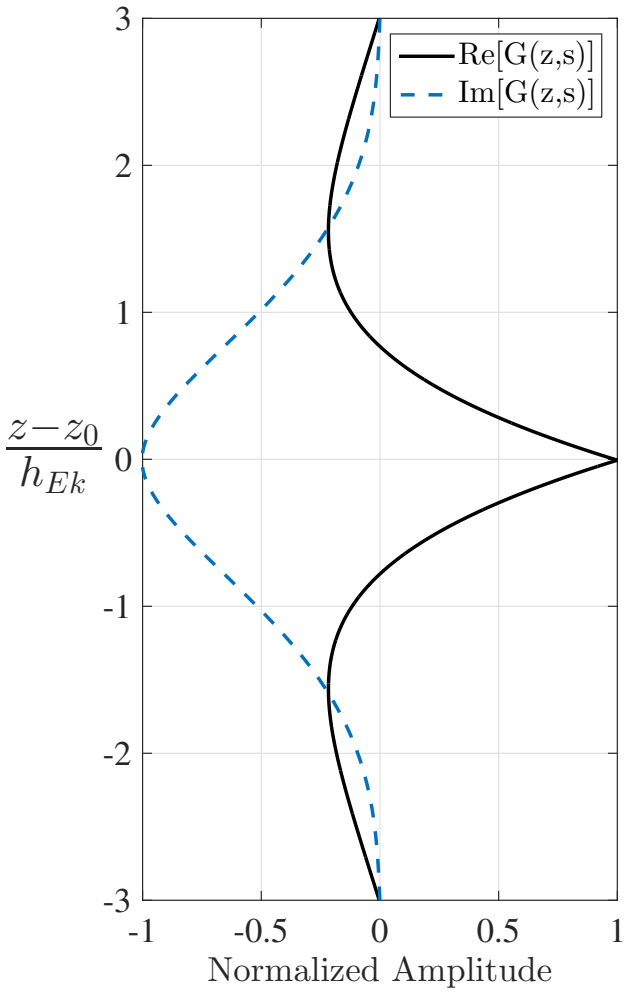

Figure 2.2: Green's function, (2.9), for a point source located at z_0 in a boundary layer of depth $h = 6h_{Ek}$.

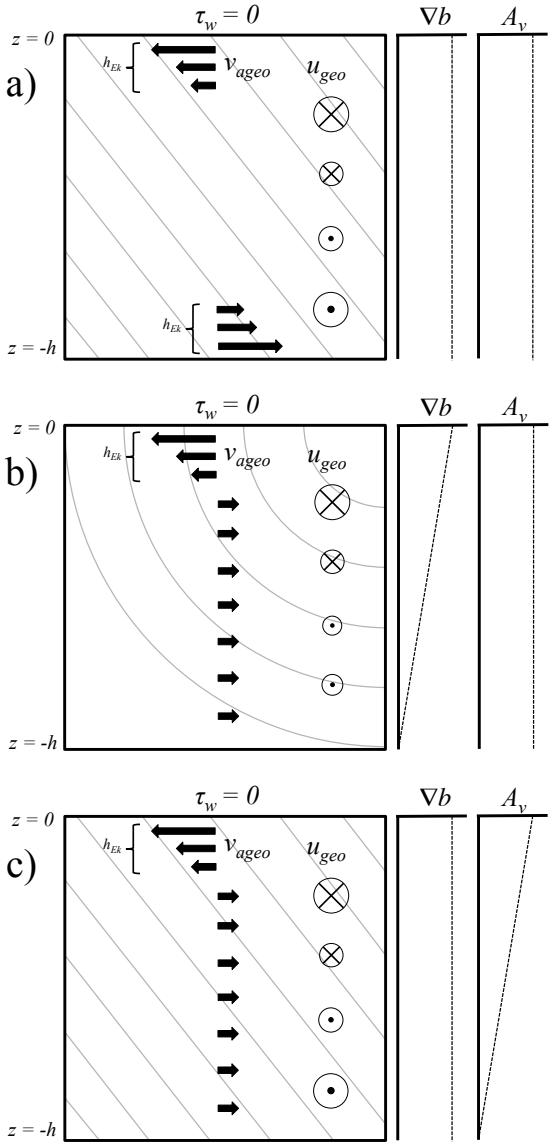

Figure 2.3: Schematics of the ageostrophic flow induced by a horizontal buoyancy gradient, with thin lines indicating density contours. a) Uniform viscosity and buoyancy gradient leads to a downgradient ageostrophic flow in the near-surface Ekman layer, and upgradient flow in a bottom Ekman layer. b) Uniform viscosity and linearly decaying buoyancy gradient leads to a downgradient ageostrophic flow in the Ekman layer, and a uniform weak upgradient flow throughout the remainder of the layer. c) linearly decaying viscosity and uniform buoyancy gradient leads to a similar pattern of flow as in the middle panel. Figure is based on Thomas and Ferrari (2008), their Figure 1.

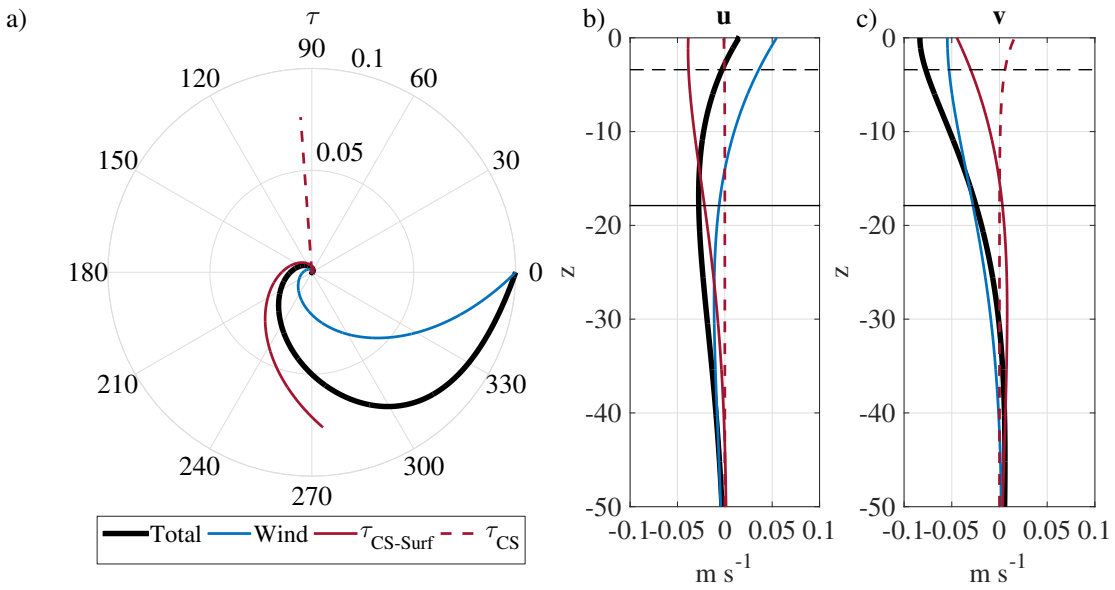

Figure 2.4: Stress and ageostrophic velocity for a zonal surface wind stress, $\tau_w = 0.1\,\mathrm{Nm}^{-2}$, in the presence of a downwind wave field with Stokes velocity amplitude $U_0 = 0.22\,\mathrm{ms}^{-1}$ and depth scale, $h_s = 3.4\,\mathrm{m}$ (Komen, 1996). a) Hodograph of total stress (black), wind-forced component (blue), component forced by the effective surface stress arising from the Coriolis-Stokes stress (solid red), and the Coriolis-Stokes stress (dashed red). b) Zonal ageostrophic velocity profile with components as in a, c) as in b but for meridional velocity. In b and c the Ekman depth (solid black) and h_s (dashed black) are indicated.

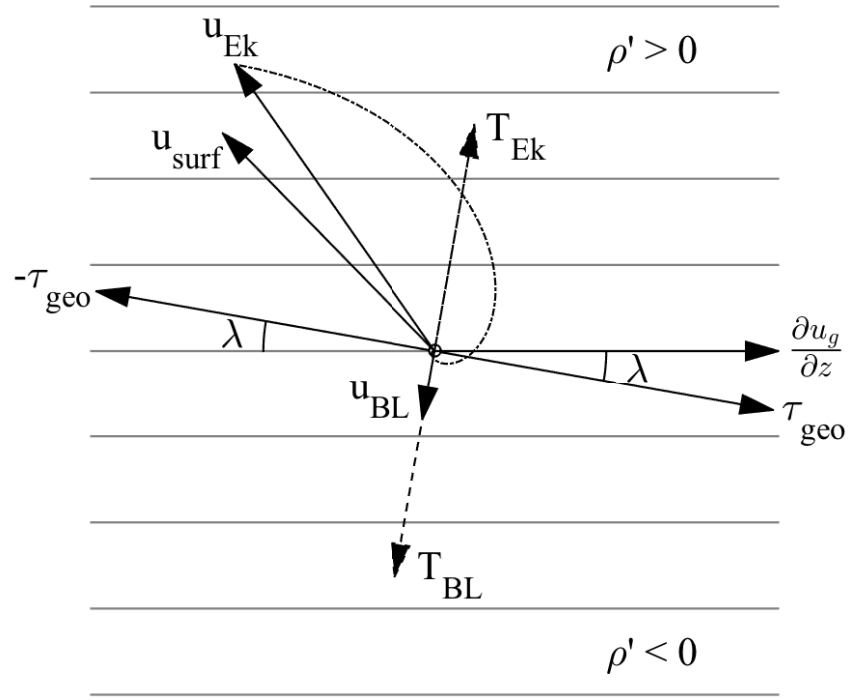

Figure 2.5: Schematic of the components of the frictional ageostrophic response to a horizontal buoyancy gradient, with contours of constant ρ shown in gray. The geostrophic stress is rotated by an angle λ from the geostrophic shear, which points along lines of constant ρ. The divergence of this geostrophic stress drives an ageostrophic velocity, u_{BL}, and transport T_{BL}, rotated 90° to the right (N. Hemisphere). Geostrophic stress at the surface drives an Ekman response, through an effective surface stress $-\tau_{geo}$, with associated velocities u_{Ek}, and transport T_{Ek}. The surface velocity is given by $u_{surf} = u_{BL}(0) + u_{Ek}(0)$. Vectors are not to scale.

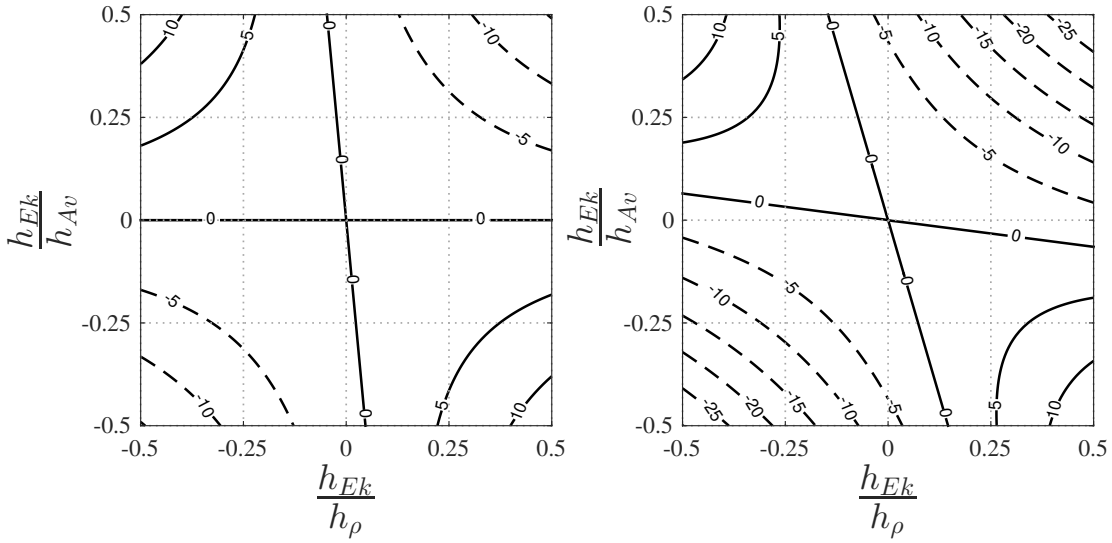

Figure 2.6: Contour plots of λ (°, positive solid, negative dashed), the angle of the geostrophic stress relative to the direction of the geostrophic shear, as defined in the text by (2.16), evaluated at $z = 0$. Left panel: Linear A_v $\left(A_v(z) = A_{v0}[1 + \frac{z}{h_{Av}}]\right)$ and linear ∇b $\left(\nabla b(z) = B_0[1 + \frac{z}{h_\rho}]\right)$, right panel: modified Gaussian A_v $\left(A_v(z) = A_{v0}[\frac{z}{h_{Av}} + 0.25]\exp[-\frac{1}{2}(\frac{z}{h_{Av}})^2 + \frac{1}{2}]\right)$, as discussed in Appendix B, and exponential $\nabla b(z)$ $\left(\nabla b(z) = B_0 e^{\frac{z}{h_\rho}}\right)$. In both plots positive parameter values indicate fields which decay downwards.

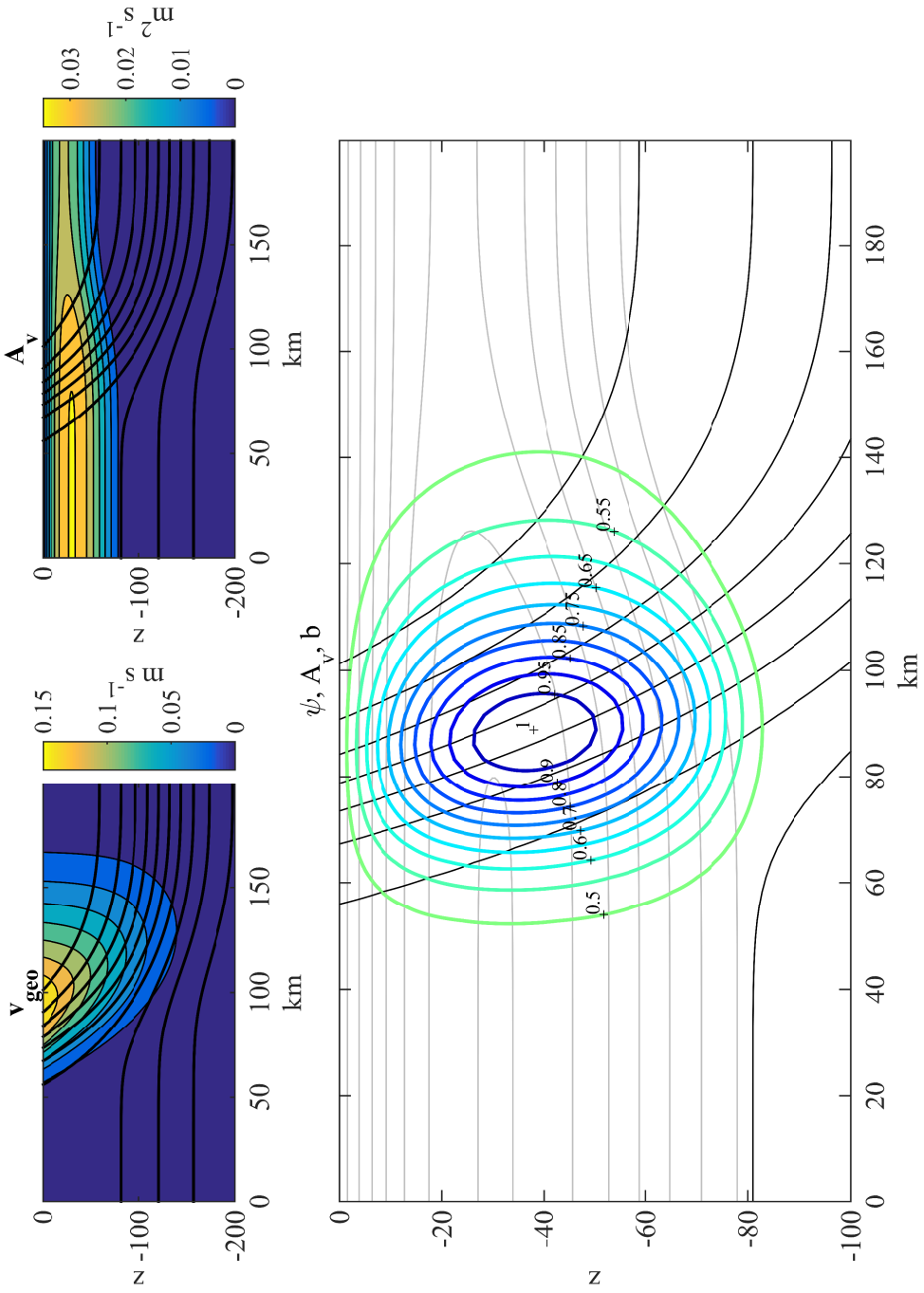

Figure 2.7: Across-front sections of the idealized two-dimensional front discussed in section 2.4, with contours of constant ρ indicated in solid black. Upper left: along-front geostrophic velocity, Upper right: A_v, Lower panel: frictional ageostrophic overturning streamfunction ($m^2 s^{-1}$, eq. (2.24)), with contours of constant A_v in gray.

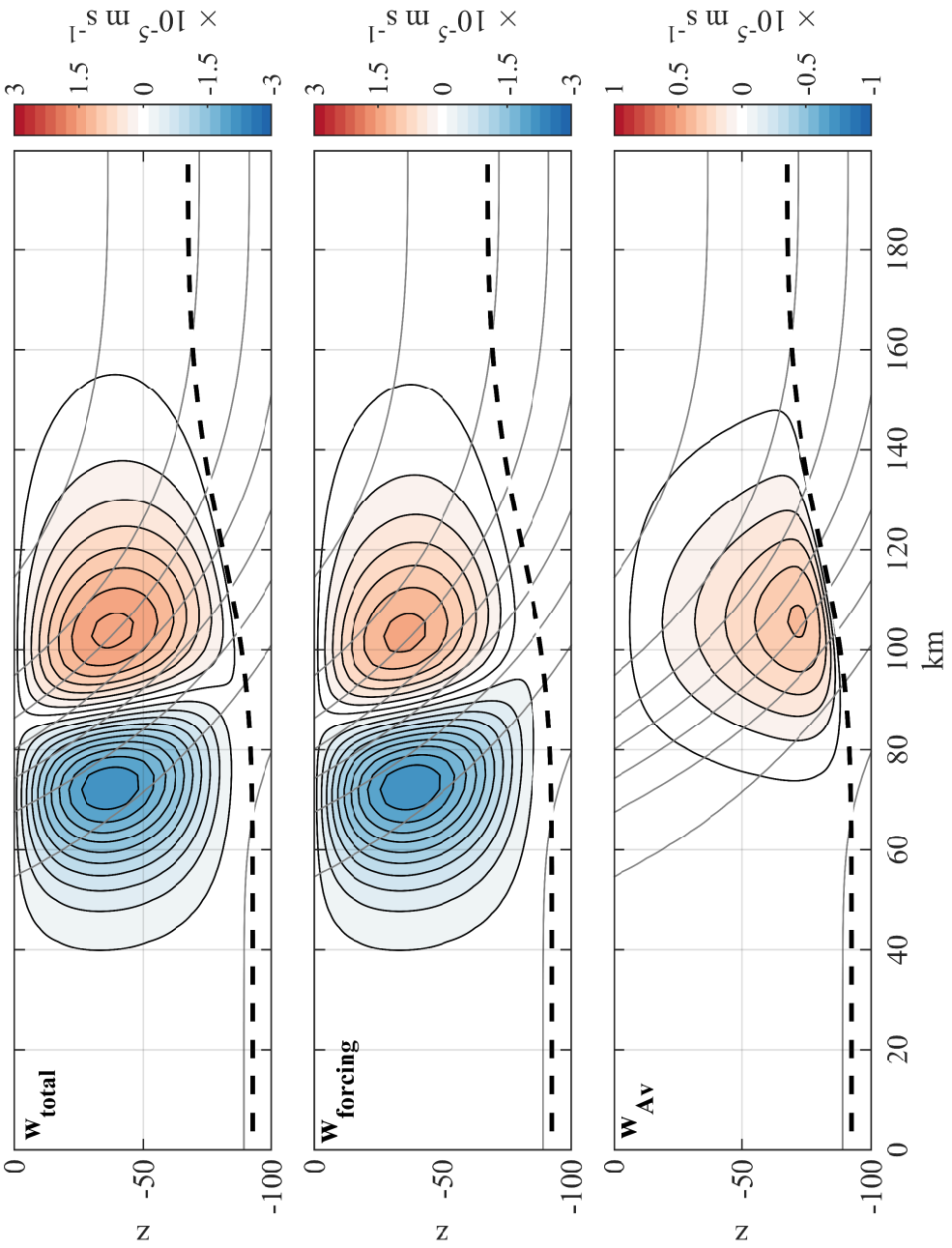

Figure 2.8: Frictionally driven boundary layer vertical velocity. Top: Total vertical velocity, Middle: vertical velocity arising from the gradient in the horizontal buoyancy gradient, Bottom: vertical velocity due to gradient in A_v. The dashed line indicates the turbulent surface boundary layer depth, defined by (2.23). Note reduced colorscale in bottom panel.

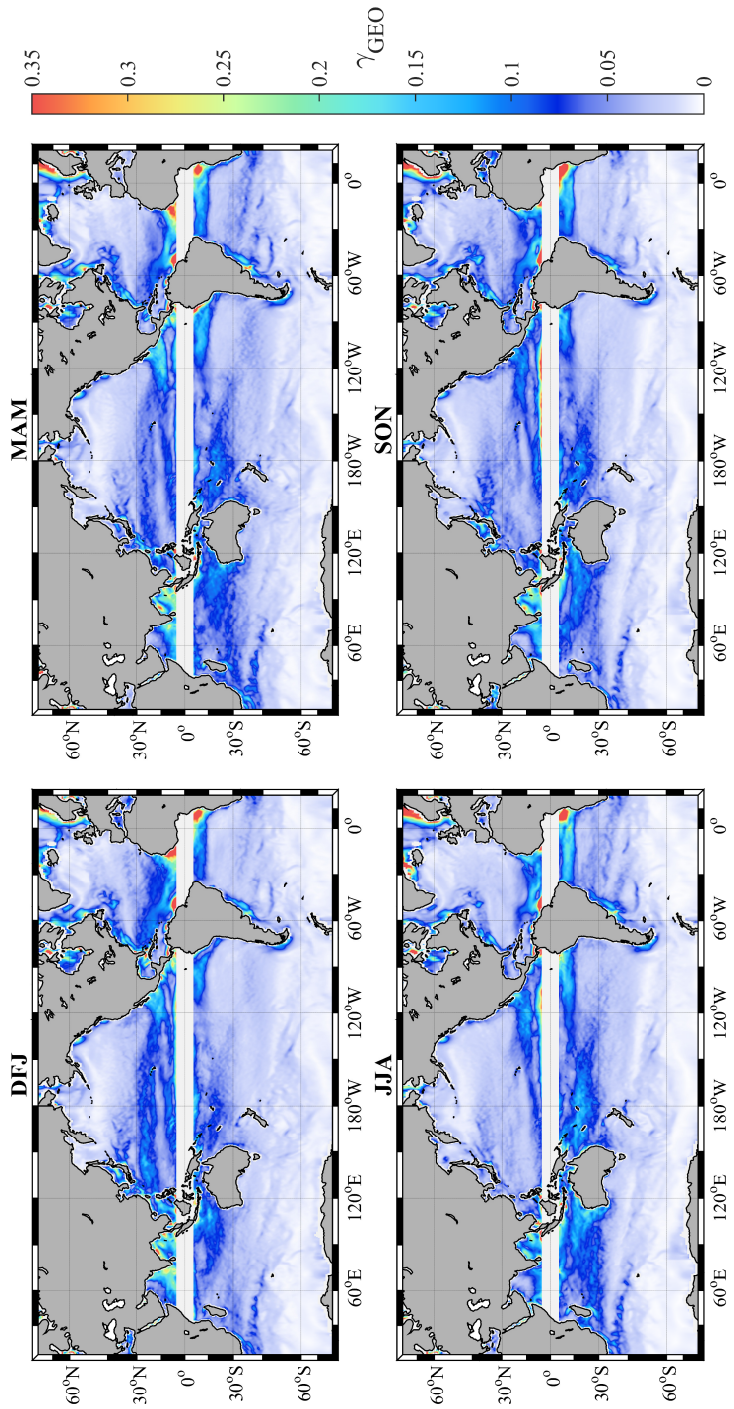

Figure 2.9: Global climatology, 2001-2011, by seasons with months indicated in plot titles, for γ_{GEO} as defined in the text by equation (2.27).

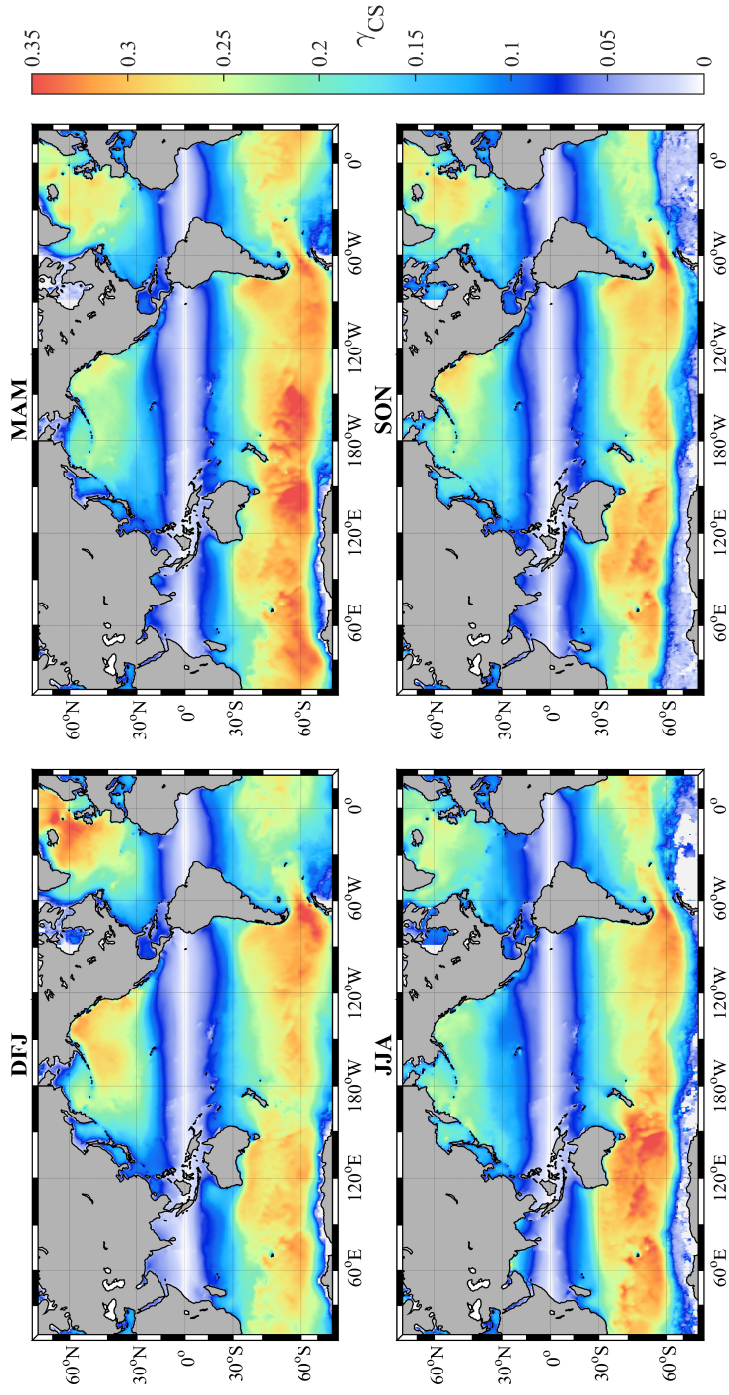

Figure 2.10: As in figure 2.9 but for γ_{CS} as defined in the text by equation (2.28).

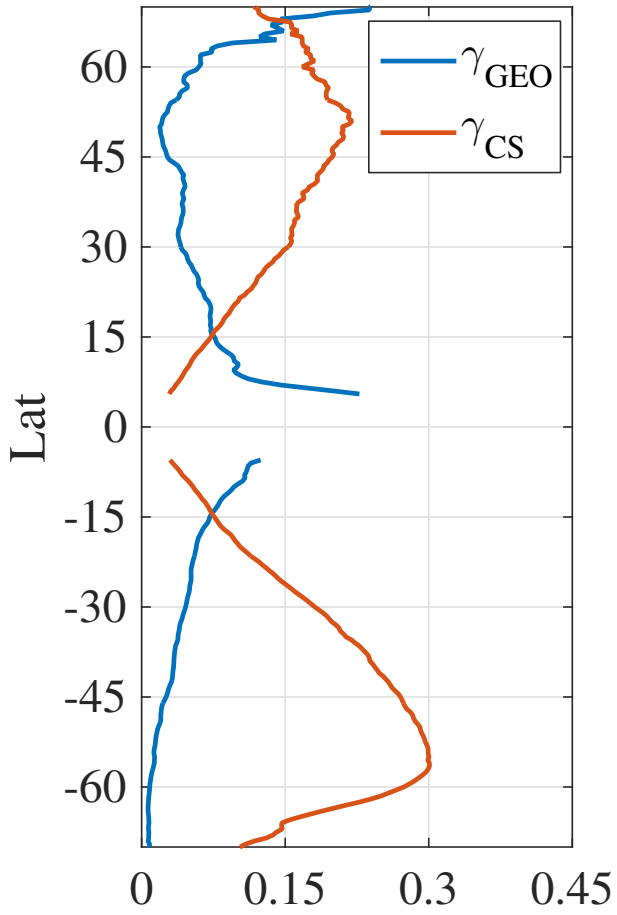

Figure 2.11: Zonal, and temporal, averages of γ_{GEO} and γ_{CS}.

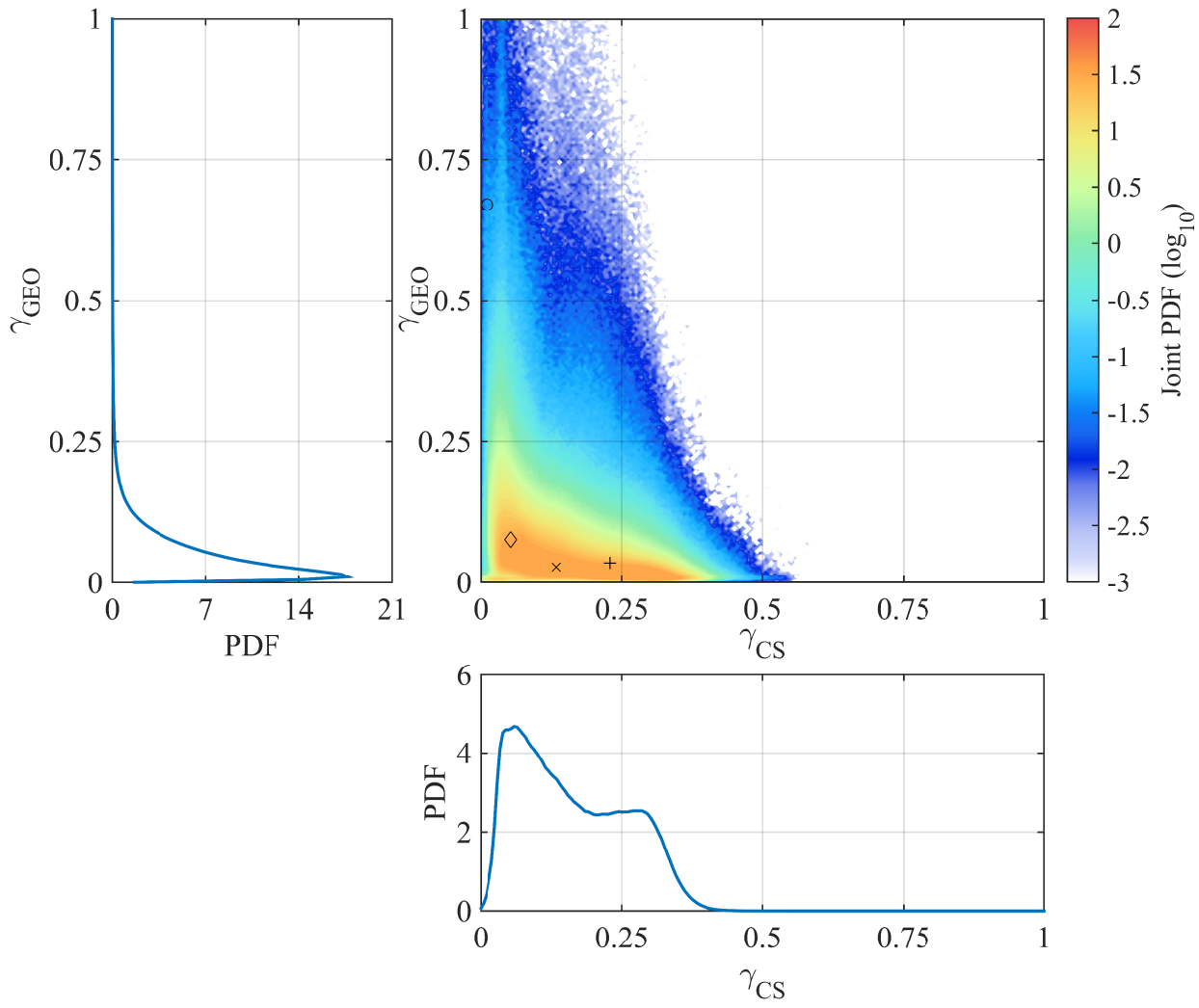

Figure 2.12: Global area-weighted joint probability density function (PDF) of γ_{GEO} and γ_{CS}, center panel, estimated monthly from 2001-2011. Left panel shows the PDF of γ_{GEO}, lower panel the PDF of γ_{CS}. Climatological average values are indicated in the center panel for the locations of several previous Ekman layer studies, Long Term Upper Ocean Study ('x', Price et al., 1987), Transpacific Hydrographic Survey (basin averaged, '$\diamond$', Wijffels et al., 1994), Eastern Boundary Current experiment ('+', Chereskin, 1995), and 2°N, 140°W ('$\circ$', Cronin and Kessler, 2009).

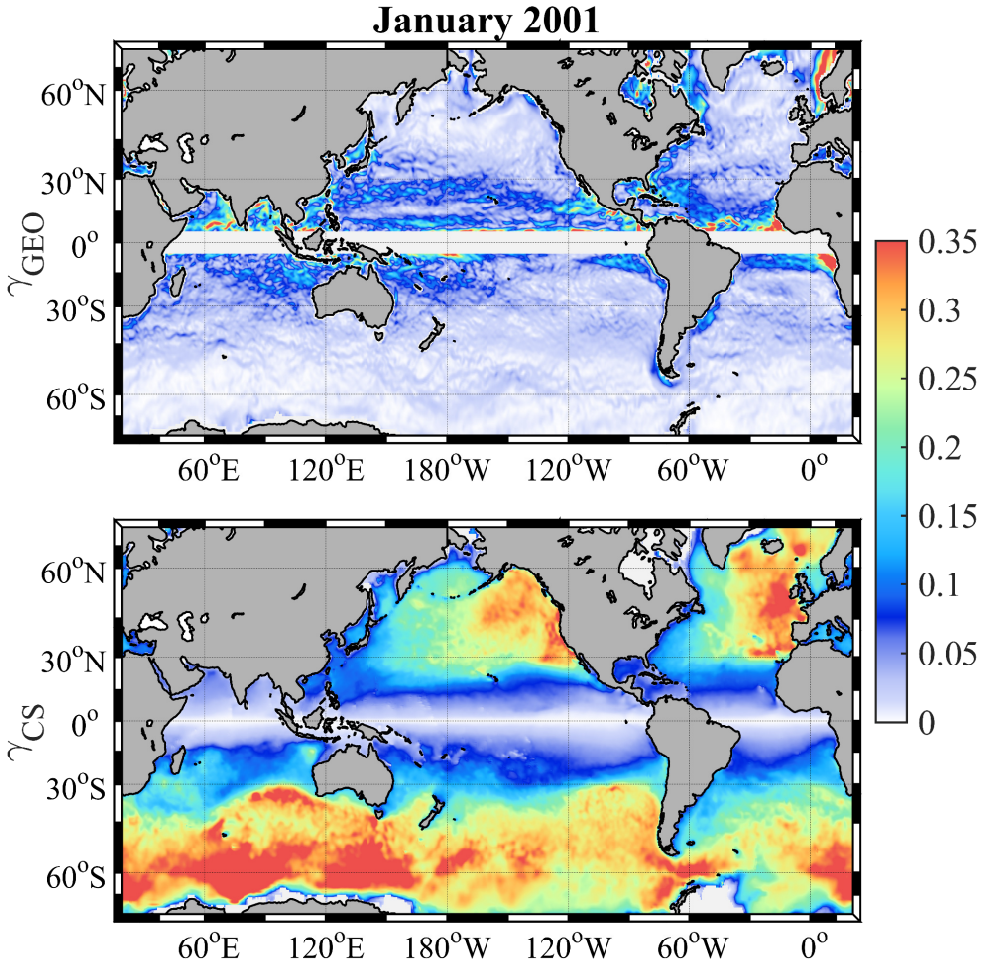

Figure 2.13: Example single month estimate of γ_{GEO} and γ_{CS}, showing additional spatial detail not evident in the climatological maps (figures 2.9, 2.10).

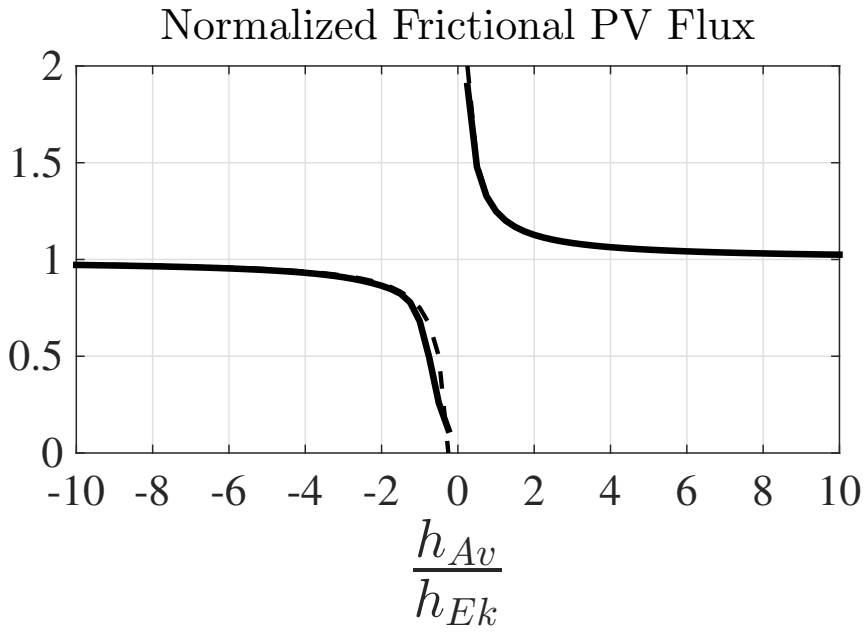

Figure 2.14: Frictional flux of vertical potential vorticity due to the wind-driven differential horizontal buoyancy advection across the Ekman layer. Numerical solutions of $f\left[u_{Ek}\cdot\nabla b\right]_{z=0}$ are plotted (solid) as a function of the eddy viscosity depth scale, where $A_v(z)=A_{v0}e^{z/h_{Av}}$. Values are normalized by (2.29). Also plotted is the scaling suggested by (2.30) (dashed), which overlaps the numerical solution for most of the parameter space.

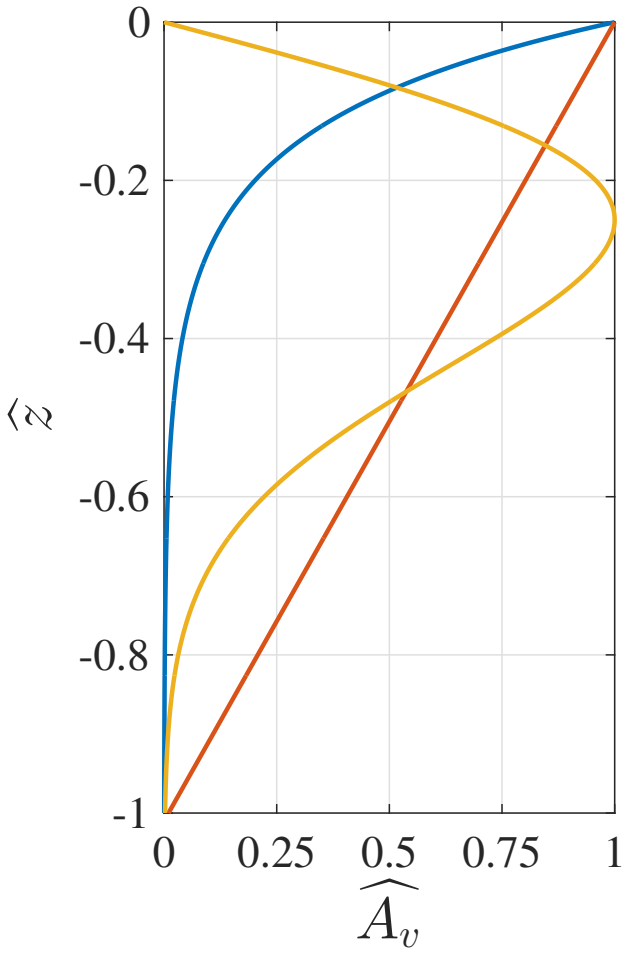

Figure 2.15: Vertical structure of A_v models considered in Appendix B. In each case the normalization is such that $h = 1$, $f = 1$, and $A_{v0} = Ek \times 1\,\mathrm{m^2 s^{-1}}$.

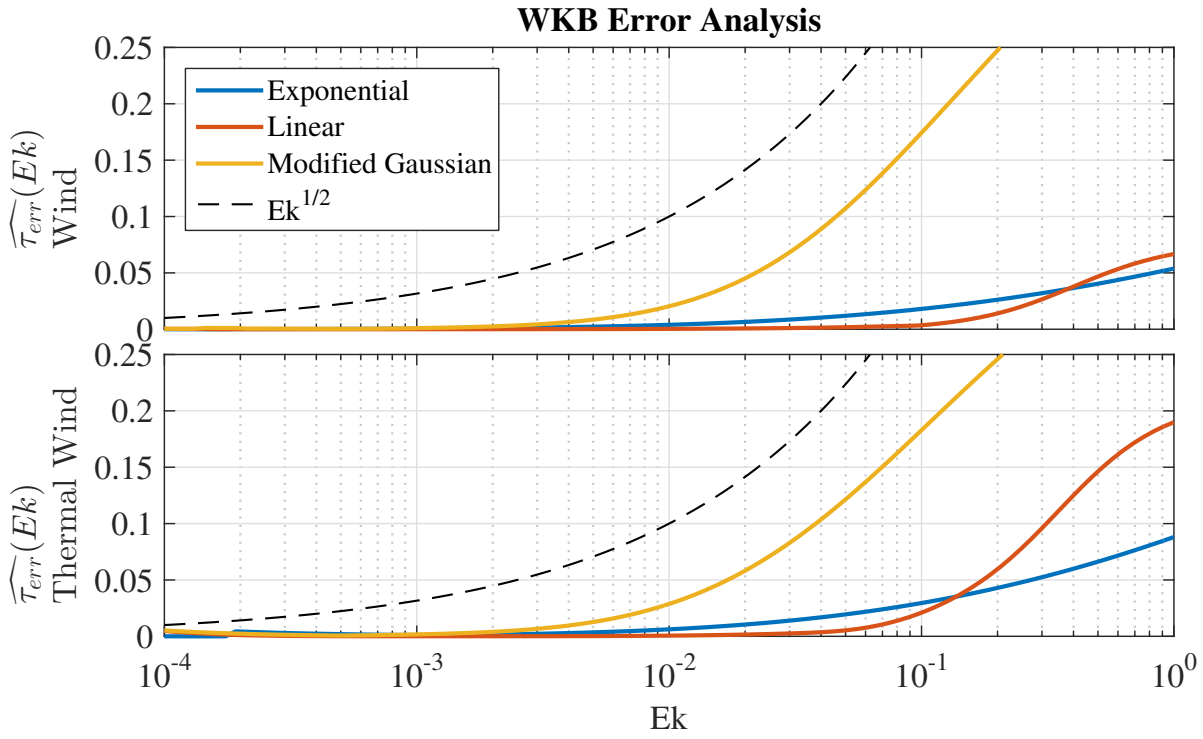

Figure 2.16: Accuracy of WKB approximation as a function of Ekman number for the A_v profiles shown in figure B1. Top panel is for wind-forcing, bottom panel for a vertically uniform horizontal buoyancy gradient. Errors are normalized according to (2.61).

Chapter 3

WIND STRESS AND NEAR-SURFACE SHEAR IN THE EQUATORIAL ATLANTIC OCEAN

The upper ocean response to wind stress is examined using eight months of unique near-surface moored velocity, temperature, and salinity data at 0°N, 23°W in the equatorial Atlantic. The effects of wind stress and shear on the time-varying eddy viscosity are inferred using the surface shear-stress boundary condition. Parameterizations of eddy viscosity as a function of wind stress and shear versus wind-stress alone are then examined. In principle, eddy viscosity should be proportional to the inverse shear but how it is represented implicitly or explicitly can affect estimates of the near-surface flow field. This result may explain some discrepancies that have arisen from using wind stress dependent parameterizations to characterize the effects of turbulent momentum mixing. [1]

3.1 Introduction

The turbulent vertical flux of wind-driven momentum plays a crucial role in the near-surface momentum budget (Smyth et al., 1996), and is critical for accurate understanding and modeling of near-surface currents. This is particularly important at low latitudes, where diminished rotational constraints increase the sensitivity of modeled currents and sea surface temperature to vertical mixing (Schneider and Mller, 1994). Most commonly, the Reynolds stress is approximated by assuming down-gradient transport by turbulence, parameterized by a turbulent eddy viscosity, denoted A_v. Closing the equations of motion then becomes a task of correctly parameterizing A_v as a function of known variables.

---

[1] An edited version of this chapter was published by AGU. Copyright (2014) American Geophysical Union: Wenegrat, J.O., M.J. McPhaden, and R.-C. Lien, 2014: Wind stress and near-surface shear in the equatorial Atlantic Ocean. *Geophys. Res. Lett.*, 41 (4), 1226-1231. DOI: 10.1002/2013GL059149

Ultimately, accurate parameterizations of near-surface A_v need to account for a wide-variety of physical processes, including shear instabilities, thermal convection, Langmuir circulation, and wave breaking (cf. Sullivan and McWilliams, 2010). However, a simple approach that is often applied within the unstratified surface mixed layer, where Richardson number dependent parameterizations are not applicable, is to parameterize A_v as a function of the wind stress alone. This approach has a long history in the literature, dating back to Ekman (1905), and more recently Santiago-Mandujano and Firing (1990, herinafter SF90). The simplicity of this type of parameterization lends itself well to analytic studies of the Ekman layer (Cronin and Kessler, 2009) or in applications where detailed upper ocean data are lacking, such as with the Ocean Surface Current Analysis - Real Time (OSCAR) surface current product (Bonjean and Lagerloef, 2002), which utilizes only remotely sensed data.

Despite the widespread use of wind-stress parameterizations of A_v, the literature contains a large spread of coefficients (Huang, 1979, SF90), and lacks clarity on their appropriate usage. Progress on this topic has been hampered by the relative scarcity of observations of near-surface velocity, as shipboard current profilers are limited by ship draft, and moored upward-facing Acoustic Doppler Current Profilers (ADCPs) are subject to surface reflection effects. Here we utilize a unique dataset from a moored downward-facing ADCP in the equatorial Atlantic, providing both high vertical resolution as well as an extended time series of near-surface velocity. Using this data we infer an eddy viscosity based on wind stress data and near-surface shear, and examine three parameterizations. Model 1 is based on regression analysis using only wind stress, following SF90. Models 2 and 3 are formulated explicitly to include the mean shear, which improves their generality and may lead to significantly more accurate modeling of near-surface flow.

3.2 Data and Methods

As part of an engineering comparison of current meters, a 600 kHz ADCP was deployed at the 0°N, 23°W Prediction and Research Moored Array in the Tropical Atlantic (PIRATA) (Bourlès et al., 2008) mooring from 13 October 2008 through 18 June 2009. The ADCP was

deployed facing downwards on the mooring bridle, and returned data in 0.75 m vertical bins between z = -3.76 m and z = -38.26 m (Fig. S1 b, c). To limit the effect of mooring motion due to surface waves, velocity data was recorded as the ensemble average of 120 consecutive 1 Hz samples, once per hour at the top of the hour.

Several ADCP velocity bins were biased by side-lobe reflection off instruments on the mooring line. Corrupted bins were identified visually based on discontinuities in profiles of echo intensity and velocity, and removed from the data. Data collected during 14-15 October 2008 and 18-19 March 2009 were particularly noisy, and consequently excluded from the analysis. ADCP velocity data was compared with point current meters located at depths of 6, 10, 17, 20, and 26 m. After correction for a systematic bias in the ADCP compass headings, the hourly zonal (meridional) interpolated ADCP velocities compared favorably with the point current meters, with correlation coefficient r = 0.994 (r = 0.985) and RMS differences of 0.032 $m\,s^{-1}$ (0.038 $m\,s^{-1}$) at 6 m depth.

Near-surface shear was calculated by forward differencing between z = -3.76 m and z = -7.51 m, the uppermost uncorrupted bins, giving a nominal depth for the uppermost shear bin of 5.64 m (Fig S1 d). A white-noise threshold for shear was determined from the spectra of shear components by taking the average spectral level (S) from 4.8 cycles per day (cpd) to the Nyquist frequency (NF), and estimating the RMS shear error as $\sigma_E = [S \times NF]^{\frac{1}{2}}$. For the hourly shear magnitude, $\sigma_E = 1.2 \times 10^{-2}\,\mathrm{s}^{-1}$, consistent with estimates derived from RMS differences between the point current meters and the ADCP.

Temperature and salinity were recorded every 10 minutes, at depths of 1, 5, 10, 13, 20, 23, 40, and 60 m and 1, 5, 20, 40, and 60 m respectively. The 1 m salinity data was only returned for the first 22 days of the record. During this period the 5 m salinity values were highly correlated with the 1 m values ($R^2 = 0.98$), hence linear regression was used to fill the missing 1 m salinity data using the 5 m observations for the remainder of the record. Density was then calculated using hourly averaged data, and linearly interpolated to a uniform grid (figure 3.4e). Mixed layer depth was defined as the depth at which the density first exceeds the 1 m density by 0.125 $\mathrm{kg\,m}^{-3}$ (Levitus, 1982).

Wind stress was calculated from mooring observations of wind speed at 4 m height (figure 3.4a), using the COARE 3.0b algorithm (Fairall et al., 2003). We consider A_v parameterizations formulated as functions of the wind stress, rather than the wind speed. This approach is most general, and avoids issues of consistency in the choice of wind stress parameterizations when the A_v parameterization is applied to new datasets. Where necessary for comparison with prior work, we approximate the conversion between wind speed and wind stress as $\vec{\tau} = \rho_{air} C_d |\vec{U}| \vec{U}$, where $\vec{U}$ is the wind velocity vector at 10 m, $\rho_{air} = 1.18\,\mathrm{kg\,m^{-3}}$, and $C_d = 1.14 \times 10^{-3}$ chosen for consistency with SF90.

Observations where the velocity shear and wind stress components are of opposite signs (implying a negative A_v), where A_v exceeds $0.045\,\mathrm{m^2 s^{-1}}$, the 99th percentile estimated using the bootstrap method, or where the uppermost bin of shear is below the mixed layer, were excluded from analysis.

3.3 Results

3.3.1 Eddy Viscosity

Continuity across the air-sea interface requires that the surface ocean stress match the wind stress. This leads to the standard surface boundary condition, $\rho A_v \vec{u_z} = \vec{\tau}$ for z = 0, where ρ is the density of seawater, $\vec{u}$ the horizontal velocity vector, z the vertical coordinate defined positive upwards, $\vec{\tau}$ the wind stress vector, and subscript z denotes differentiation. Assuming wind stress and shear are aligned (discussed below), the boundary condition can be rearranged to give a formula for A_v,

$$A_v = \frac{\tau}{\rho u_z}, \quad for\ z = 0, \tag{3.1}$$

where the vector notation has been dropped to indicate vector magnitudes.

We evaluate (3.1) using hourly wind stress and shear, assuming uniform stress in a layer between the surface and 5.64 m. Observational evidence suggests that near-surface stress profiles decay smoothly from the surface wind stress value (Smyth et al., 1996), however,

temporal variability of the vertical structure of near-surface stress is not well understood, and may be a function of Richardson number (Soloviev et al., 2001) or free-surface effects (McWilliams et al., 2012). Assuming a linear decay of stress between the surface and the thermocline (Hebert et al., 1991; Smyth et al., 1996), the average stress at 5.64 m will be 92% of the surface stress, which does not materially alter our analysis. Given this, we do not attempt to correct for a decaying near-surface stress profile, and proceed with the assumption of a uniform stress layer. Free surface effects may modify the shear profile near the surface, thus the value of A_v we infer is most conservatively treated as the 5.64 m value.

Daily values of the shear direction are generally aligned with the wind stress direction (figure 3.1a), although greater scatter is observed in hourly values. Misalignment between wind stress and shear would suggest a vector A_v. However, as (3.1) still defines the magnitude of A_v, we don't further consider the directionality of A_v here. Consistent with SF90, we find that the shear magnitude is not well correlated with the wind stress magnitude (figure 3.1b), confirming that A_v must be a time-varying quantity in order to fulfill the surface boundary condition. Observations span several decades of magnitude of A_v (figure 3.1b, color scale), with comparable variance in each dimension.

The variance of A_v can be approximated using the first order Taylor expansion of (1), giving $Var(A_v) \approx \frac{\bar{\tau}^2}{(\rho^2 \bar{u_z}^2)} \left(\frac{Var(\tau)}{\bar{\tau}^2} - \frac{2Cov(\tau,u_z)}{\bar{\tau}\bar{u_z}} + \frac{Var(u_z)}{\bar{u_z}^2} \right)$, where overbars denote mean values. The first and third terms on the RHS are comparable in magnitude, and together are approximately 5 times larger than the covariance term. Two-dimensional projections of A_v as a function of each independent variable (figure 3.1c,d) also emphasize that although A_v can be approximated as a univariate function of either stress or shear, both independent variables contribute to the true A_v. The accuracy of wind-stress only parameterizations will decline with increasing shear variance, and so, before discussing parameterizations, we characterize the variability of the shear.

3.3.2 Shear Variability

Figure 3.2 shows the variance preserving spectra of the wind stress and shear components. Each component is normalized by the square of its time domain mean, as it appears in the first-order Taylor series expansion of the A_v variance (Section 3.3.1), allowing a frequency-domain estimate of the relative contribution of each variable to the eddy viscosity. At the lowest frequencies variability is dominated by the wind stress, with comparable contributions from both shear and stress between frequencies of approximately 0.05 to 0.8 cpd, above which shear variance surpasses stress variance. Wind-stress only parameterizations are thus expected to perform best at the lowest frequencies, where the relative shear variance is low, and to miss significant portions of the true variance at frequencies at or above 0.05 cpd, where the shear variance increases.

Shallow mixed layers were found to be associated with both increased variability, and mean values, of near-surface shear (figure 3.3). This is believed to result both from the formation of an afternoon near-surface stratified diurnal jet (Price et al., 1986), as well as the vertical advection of the high shear region on the upper flank of the equatorial undercurrent during periods of low wind stress (figure 3.3 color scale, figure 3.4). Consequently, for the equatorial region, wind-stress only parameterizations may not be appropriate in the case of shallow mixed layers, or low wind stress. Alternatively, our assumption of uniform stress between the surface and 5.64 m may be violated when the mixed layer is shallow. Attempts to relate shear to other physical variables, such as the thermocline depth or the Monin-Obukhov length were unsuccessful.

Next, we consider three models that parameterize A_v as a function of wind stress.

3.3.3 Model 1: Wind-Stress Only

Previously, parameterizations of A_v as a function of wind stress alone have specified a model of the form $A_v = \beta\tau$, where β is estimated by least squares regression. When an intercept term is included it is found to not be significantly different than zero, as anticipated from

(3.1), and we proceed using regression through the origin, which produces the following estimate of the coefficient:

$$\hat{\beta} = \frac{\sum \tau A_v}{\sum \tau^2} = \frac{1}{\rho}\overline{\left(\frac{1}{u_z}\right)} + \frac{Cov\left(\tau^2, u_z^{-1}\right)}{\rho\overline{\tau^2}} \tag{3.2}$$

For our dataset $\hat{\beta} = 0.113\,\mathrm{m^2 s^{-1} Pa^{-1}}$ (Table 1, figure 3.5), similar to that of SF90. We note that SF90 also considered a regression based on the logarithm of (3.1), however in the wind ranges considered here (0 - 10 $\mathrm{m\,s^{-1}}$) the two formulations are very similar.

3.3.4 Model 2: Mean Inverse Shear

In our dataset, the correlation between inverse shear and squared stress is weak, thus a simple and transparent estimate for β is given by,

$$\bar{\beta} = \frac{1}{\rho}\overline{\frac{1}{u_z}} \tag{3.3}$$

In the case of completely uncorrelated inverse shear and squared stress (3.3) is exactly equivalent to (3.2), and our estimate $\bar{\beta} = 0.108\,\mathrm{m^2 s^{-1} Pa^{-1}}$ is within the confidence intervals of our estimate of $\hat{\beta}$ (Table 1, figure 3.5). Model 2 has the advantage of explicitly including the dependence on the mean inverse shear, a dependence that is obscured in regression based coefficients.

3.3.5 Model 3: Mean Shear

One important consequence of utilizing a parameterization where A_v is directly proportional to the wind stress is that it follows immediately from (3.1) that $u_z = (\rho\beta)^{-1}$. Hence, the estimated surface shear magnitude is assumed constant by definition. Generally $\overline{u_z} \neq \left(\overline{u_z^{-1}}\right)^{-1}$, so the shear calculated using model 1, or 2, will be biased relative to the true shear. This argues for the parameterization,

$$\tilde{\beta} = \frac{1}{\rho}\frac{1}{\overline{u_z}} \tag{3.4}$$

which is the first term in a Taylor expansion of (3.1), exact only when the true shear is constant. Table 1 shows that by traditional measures model 3 underperforms the other models, and additionally we note that it is the most biased of the models (figure 3.5). However, model 3 minimizes $\sum \left(u_z - (\rho\beta)^{-1}\right)^2$, the mean-square error of shear estimated using the surface boundary condition, desirable for modeling surface currents. This is discussed further below.

3.4 Discussion

In the absence of detailed upper ocean data it is often necessary to rely on very simple parameterizations of A_v, and wind-stress only parameterizations have a history in the literature of over a century and remain an appealing goal (Huang, 1979). However, wind-stress only parameterizations, of any form, imply $u_z = \tau \left[\rho A_v(\tau)\right]^{-1}$, or equivalently $u_z = f(\tau)$. Without the inclusion of additional parameters to constrain the relationship between shear and stress, Figure 3.1b suggests that the best possible choice may simply be constant u_z, which implies $A_v \propto \tau$. Within the framework of Ekman dynamics, this can be understood as the boundary layer depth adjusting to the wind stress, maintaining constant near-surface shear. Our analysis suggests that this form of parameterization may not be accurate at frequencies above 0.05 cpd, and in the case of shallow mixed layers and low wind stress.

Examining the algebraic statement for the regression coefficient (3.2) highlights the first order dependence on the mean inverse shear. Thus, discrepancies in published coefficients for wind-stress only parameterizations could result simply from the different mean shears across observations, a fact that also raises doubts about the generality of these parameterizations. Accordingly, rather than relying on published coefficients, it is preferable to use some local estimate of the mean shear which might come from either in-situ or historical data when available. A high correlation between monthly averaged bulk shear and bulk stratification

over the upper 30 m ($R^2 = 0.80$) is consistent with the observed relationship between shear and mixed layer depth (section 3.3.2), and suggests the possibility that in-situ stratification data might be used to infer an expected near-surface shear when no direct estimate is available, a form of Richardson number closure (cf. Pollard et al., 1973; Price et al., 1986; Ralph and Niiler, 1999).

Coefficients proportional to the mean inverse shear, as is implicit in regression-based models, result in considerably biased estimates of the surface shear. Comparing the OSCAR model, which is based on the analytical model of Bonjean and Lagerloef (2002) and utilizes the SF90 parameterization for equatorial A_v, to our data set reveals a $25\,\mathrm{cm\,s^{-1}}$ eastward bias in the OSCAR currents. This is consistent with a recently identified eastward bias in the OSCAR climatology throughout the equatorial Atlantic and Pacific Oceans (Lumpkin and Johnson, 2013). For this data set model 3 implies surface shears 35% larger than SF90, suggesting that a portion of the observed bias may be related to the choice of A_v parameterization. However, velocity errors are sensitive to both the surface value and the vertical profile of shear, highlighting the need for further study of the vertical structure of A_v in the near surface layer.

Table 3.1: Summary of Model Parameters.

	$\beta \times 10^2$	R_a^2	R_b^2	SE$\times 10^3$	NRMSE
Model 1	11.3 (10.8, 11.9)	0.61	0.33	2.54	1.18
Model 2	10.8 (10.3, 11.4)	0.56	0.33	2.54	1.16
Model 3	6.59 (5.50, 7.67)	0.21	0.14	2.99	1.00
SF90	8.9	0.38	0.28	2.65	1.07

β ($\mathrm{m^2\,s^{-1}\,Pa^{-1}}$) coefficients with 95% confidence intervals calculated using the wild bootstrap method; R_a^2 is the coefficient of determination for regression through the origin (Eisenhauer, 2003); R_b^2 is the standard squared correlation coefficient; SE is the heteroscedastic-consistent standard error ($\mathrm{m^2 s^{-1}}$) (Cribari-Neto, 2004); and NRMSE is the RMS error of the estimated shear, normalized by the standard deviation.

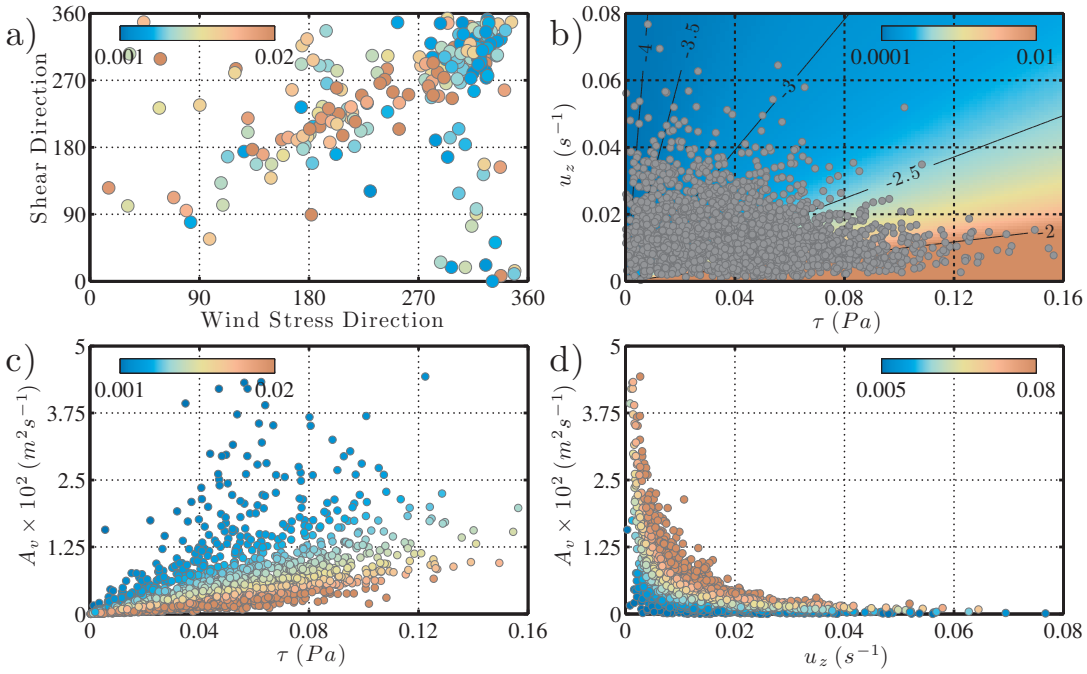

Figure 3.1: a) Daily averaged shear direction vs. wind stress direction with shear magnitude (color scale, s^{-1}), b) hourly shear magnitude vs. wind stress magnitude, superimposed over the value of A_v predicted by (1) (color scale, $m^2 s^{-1}$, and log contours), c) A_v vs. wind stress, with shear magnitude (color scale, s^{-1}), d) A_v vs. shear, with wind stress magnitude (color scale, Pa).

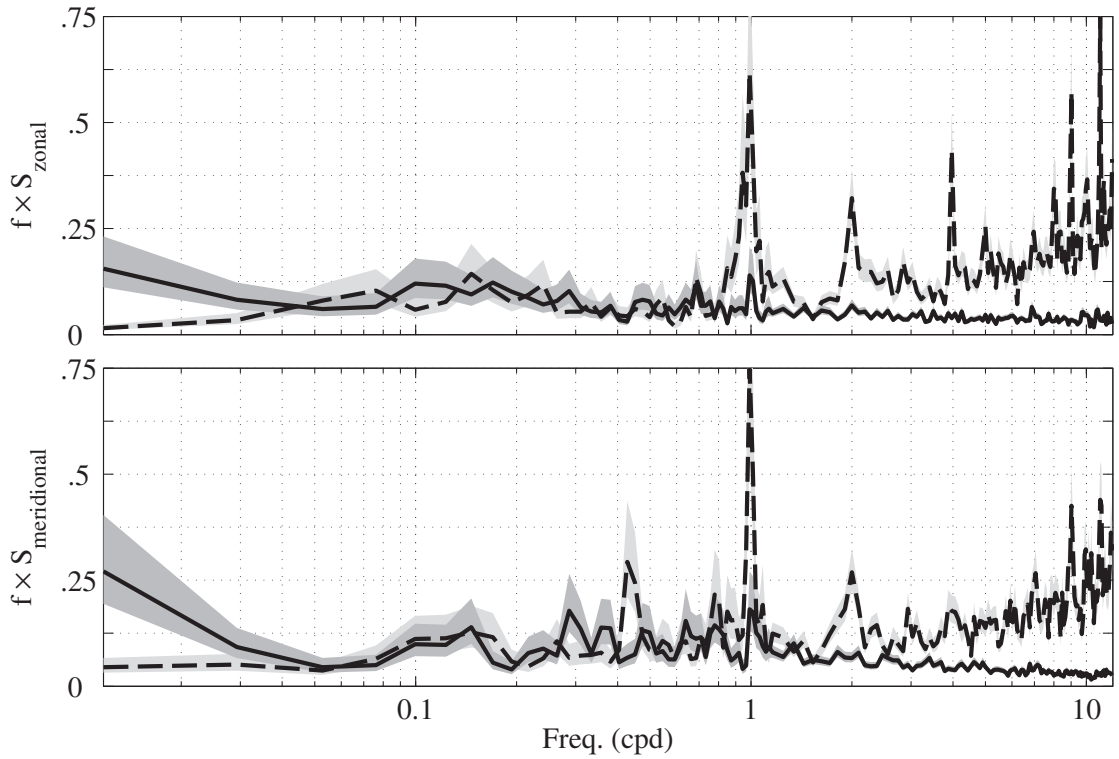

Figure 3.2: Variance preserving spectra for, Top: Zonal components of wind stress (solid) and shear at 5.64 m (dashed), with 95% confidence intervals (shaded), Bottom: As in top, but for meridional components. Both shear and stress spectra are non-dimensionalized as discussed in Section 3.3.1.

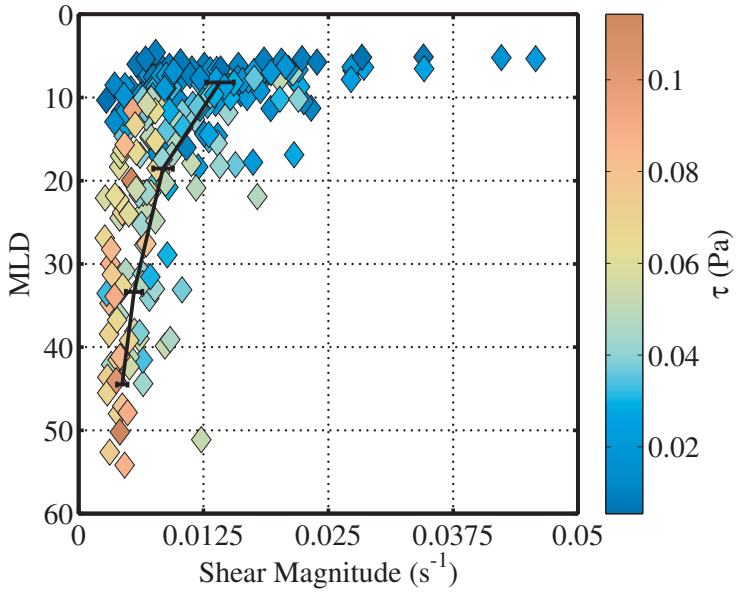

Figure 3.3: Daily shear magnitude at 5.64 m vs. mixed layer depth (scatter), binned mean shear with 95% confidence intervals based on a one sample t-test (solid line), and daily wind stress magnitude (color scale).

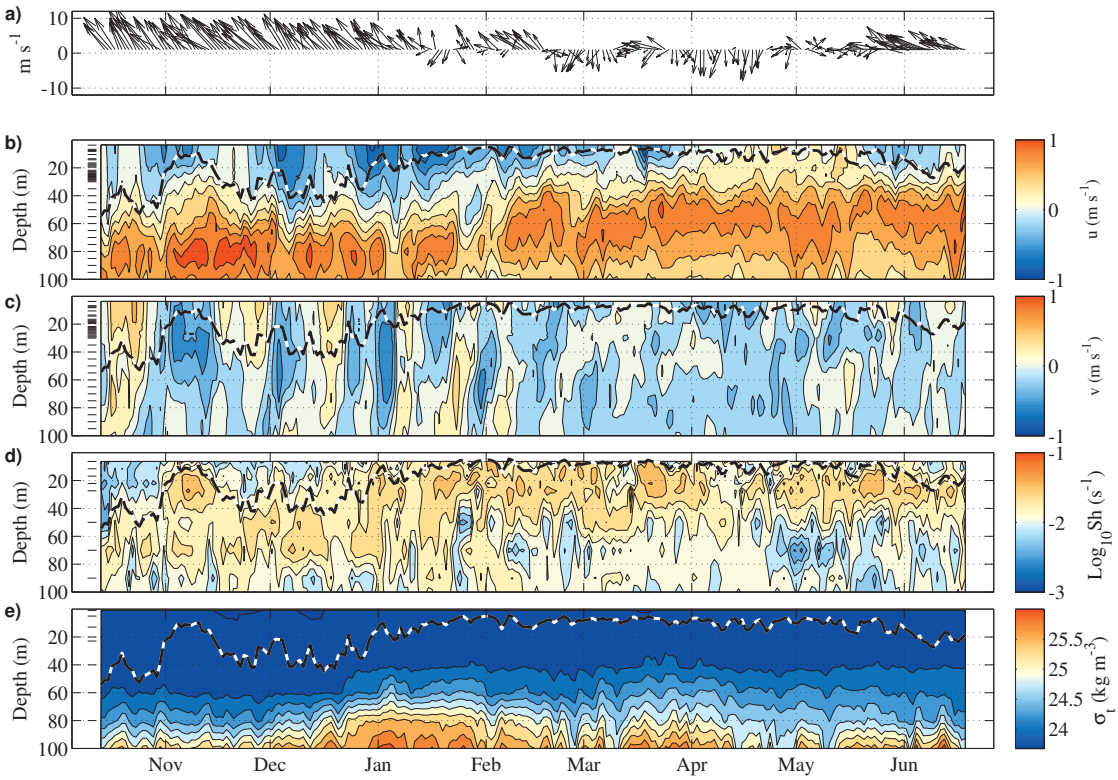

Figure 3.4: Overview of observations, a) Wind vectors oriented with North up, and East right ($m\,s^{-1}$), b) Zonal velocity ($m\,s^{-1}$), tick marks inside the left vertical axis indicate observation depths, black and white line indicates mixed layer depth defined as a $\Delta\rho = 0.125\,\mathrm{kg\,m^{-3}}$ from the 1 m value. Data from a subsurface upward-facing ADCP deployed approximately 6 km from the surface mooring is included to provide velocities below 35 m for context, c) as in (b) but for meridional velocity, d) as in (b) but for shear magnitude (s^{-1}), with logarithmic color scale, e) density ($kg\,m^{-3}$), tick marks inside the left vertical axis indicate temperature observation depths.

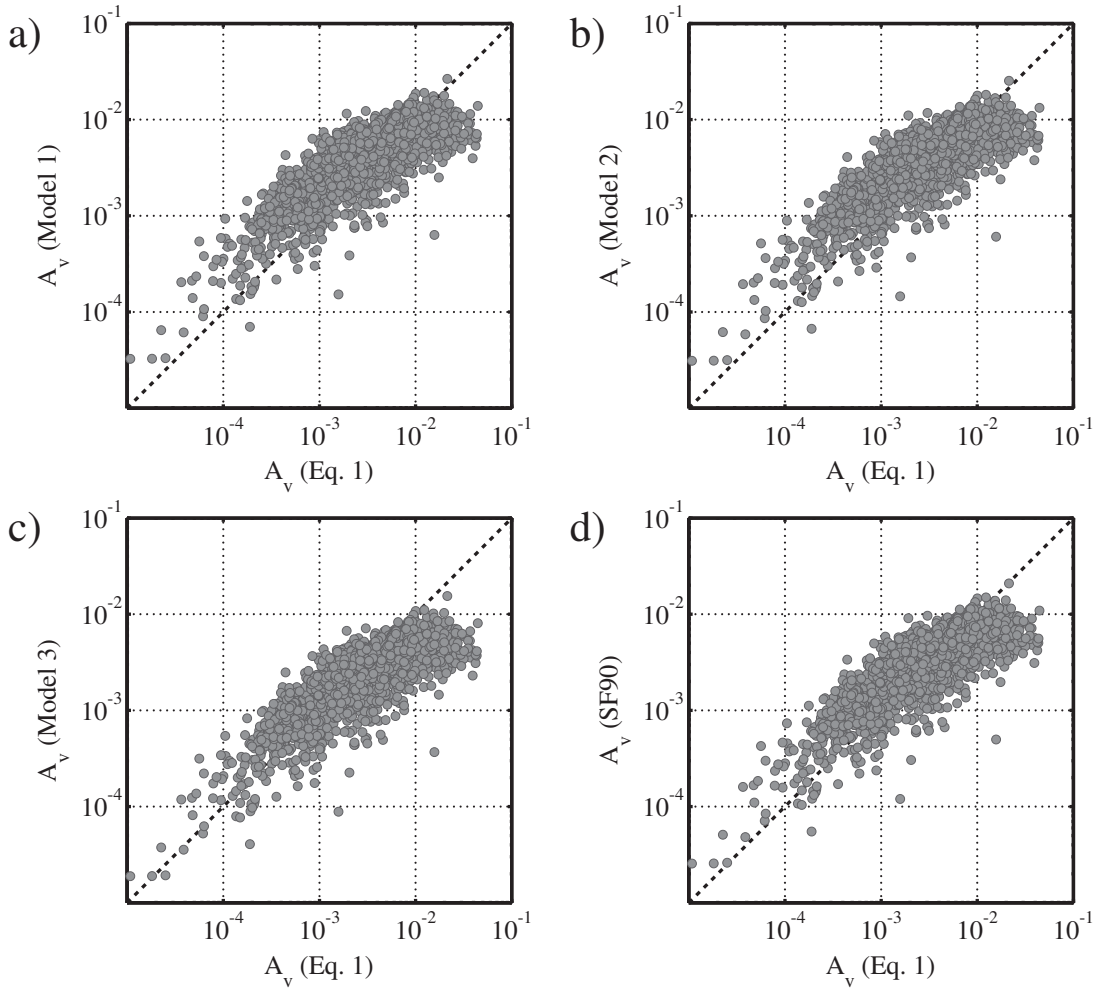

Figure 3.5: Model comparisons to A_v, a) Model 1, b) Model 2, c) Model 3, d) SF90. All units are $m^2 s^{-1}$. The roll-off of modeled values at high values of A_v results from the gradient of A_v in the plane being increasingly aligned with the shear axis for high values of A_v (Fig. 1 b). This can also be observed in the (A_v, τ) plane, where high values of A_v are associated with increased scatter (figure 3.1c).

Chapter 4

DYNAMICS OF THE SURFACE LAYER DIURNAL CYCLE IN THE EQUATORIAL ATLANTIC OCEAN (0°, 23°W)

A 15 year time series (1999-2014) from the 0°, 23°W Prediction and Research Moored Array in the Tropical Atlantic (PIRATA) mooring, which includes an 8-month record (10/2008-6/2009) of high-resolution near-surface velocity data, is used to analyze the diurnal variability of sea surface temperature, shear, and stratification in the central equatorial Atlantic. The ocean diurnal cycle exhibits pronounced seasonality that is linked to seasonal variations in the wind field. In boreal summer and fall steady trade winds and clear skies dominate, with limited diurnal variability in sea surface temperature. Diurnal shear layers, with reduced Richardson numbers, are regularly observed descending into the marginally unstable equatorial undercurrent below the mixed layer, conditions favorable for the generation of deep-cycle turbulence. In contrast, in boreal winter and spring winds are lighter and more variable, mixed layers are shallow, and diurnal variability of sea surface temperature is large. During these conditions diurnal shear layers are less prominent, and the stability of the undercurrent increases, suggesting seasonal covariance between diurnal near-surface shear and deep-cycle turbulence. Modulation of the ocean diurnal cycle by tropical instability waves is also identified. This work provides the first observational assessment of the diurnal cycle of near surface shear, stratification, and marginal instability in the equatorial Atlantic, confirming previous modeling results, and offering a complementary perspective on similar work in the equatorial Pacific. [1]

---

[1]An edited version of this chapter was published by AGU. Copyright (2015) American Geophysical Union: Wenegrat, J.O., and M.J. McPhaden, 2015: Dynamics of the surface layer diurnal cycle in the equatorial Atlantic Ocean (0°, 23°W). *J. Geophys. Res. Oceans*, 120 (1), 563-581.

4.1 Introduction

The daily cycle of solar insolation is one of the most fundamental drivers of variability in the Earth system, with prominent effects on both the atmosphere and oceans. The diurnal cycle of heat flux between the surface ocean and the atmosphere results in a concomitant cycle of sea surface temperature (SST), which was observed as early as 1854 by *William Henry Smyth*, who recorded 3-4°C diurnal variations in Mediterranean SST (Smyth, 1854). Around the same time the importance of these diurnal SST variations for ocean variability and air-sea interaction was posited by Maury (1864) who vividly described the diurnal variability of atmosphere and ocean as 'cogs, and ratchets, and wheels in that grand and exquisite machinery which governs the sea.'

Subsequent to those early observations, it was established that much of the global ocean exhibits significant diurnal variability of SST (Stommel et al., 1969; Halpern and Reed, 1976; Stuart-Menteth, 2003), with the largest annual mean diurnal SST ranges reaching 0.5-1°C in the tropics (Bernie et al., 2007). The diurnal cycle of SST has also been shown to feedback to the atmosphere in a variety of important ways (Clayson and Curry, 1996), including modifying the heat and moisture content in the atmospheric boundary layer, with significant effects on the lifecycle of convective cloud systems and associated precipitation (Chen and Houze, 1997; Clayson and Chen, 2002; Dai and Trenberth, 2004; Woolnough et al., 2007). Modeling studies also reveal that diurnal variability modifies SST on intraseasonal, seasonal, and longer timescales (Shinoda, 2005; Danabasoglu et al., 2006; Bernie et al., 2007, 2008), which presents a challenge for accurate climate modeling (Flato and al, 2013; Sillmann et al., 2013).

The diurnal cycle of solar heating also has important dynamic effects, as afternoon stratification of the near-surface layer inhibits the vertical transfer of momentum that is input at the ocean surface by the wind (Price et al., 1986). Over the course of the day, the trapping of momentum can lead to the creation of a highly sheared near-surface diurnal jet. After the mid-day peak of solar insolation, this sheared diurnal jet can decrease the near-surface

Richardson number, moving the flow towards shear instability (Price et al., 1986; Cronin and Kessler, 2009; Smyth et al., 2013). Recent work in the tropical Pacific suggests that the descent of this low Richardson number shear layer into a marginally unstable equatorial undercurrent system can provide the initiation mechanism for deep-cycle turbulence (Smyth et al., 2013; Pham et al., 2013), leading to large vertical fluxes of heat and momentum through the thermocline (Lien et al., 1995; Moum et al., 2013).

While the fundamental role that the diurnal cycle of near-surface stratification, and shear, plays in the dynamics of the equatorial Pacific has been extensively documented (Gregg et al., 1985; Moum and Caldwell, 1985; Peters et al., 1994; Sun et al., 1998), to date the diurnal cycle in the equatorial Atlantic has not been as fully characterized. Recent microstructure field campaigns have provided an initial view into the turbulent processes occurring in the upper equatorial Atlantic, with suggestions of deep cycle turbulence, although reduced in strength relative to the Pacific (Crawford and Osborn, 1979; Hummels, 2012; Hummels et al., 2013, 2014). The diurnal cycle of turbulence has not been as clearly identified in observations, although this may result from limited temporal resolution, as modeling studies suggest an expectation of processes similar to those identified in the Pacific (Skielka et al., 2011; Wade et al., 2011).

Here we utilize a long time series spanning 15 years of atmosphere and ocean data from the 0°, 23°W PIRATA mooring in the central equatorial Atlantic (Fig. 4.1) (Servain et al., 1998; Bourlès et al., 2008) to address the dynamics of the surface layer diurnal cycle. This mooring is located in the Atlantic cold tongue region (Fig. 4.1), enabling comparisons with the extensive diurnal cycle literature from 0°, 140°W in the Pacific (Gregg et al., 1985; Moum and Caldwell, 1985; Bond and McPhaden, 1995; Lien et al., 1995; Sun et al., 1998; Smyth et al., 2013). Additionally, this time series is augmented with data from an 8-month enhanced monitoring period (EMP) where high resolution velocity observations resolved hourly horizontal currents between depths of 3.75 m and 150 m.

Together these observations, which are described in Section 4.2, enable a unique description of diurnal variability spanning from the ocean surface to the thermocline. Section 4.3

begins with a description of the seasonal cycle of diurnal SST in relation to atmospheric forcing, followed in Section 4.4 by a detailed examination of the mixed-layer processes which mediate the surface response to forcing. Finally, Section 4.5 examines the seasonal cycle of stability of the undercurrent layer below the mixed layer, a proxy for deep-cycle turbulence (Smyth et al., 2013). To the best of our knowledge this represents the first in-situ observational assessment of the diurnal cycle of near-surface shear, stratification, and marginal instability in the equatorial Atlantic Ocean.

4.2 Data

4.2.1 PIRATA Data

PIRATA moorings are instrumented with a suite of subsurface temperature and salinity measurements (Table 1). In addition to the subsurface measurements, the 0°, 23°W mooring collects enhanced atmospheric measurements as part of the OceanSITES program of deep-water flux measurement sites (*http://www.pmel.noaa.gov/tao/oceansites/*). Included in the surface instrumentation are measurements of wind speed and direction, air temperature, relative humidity, rainfall, and downwelling shortwave and longwave radiation. Daily averaged observations are transmitted from the mooring via real-time telemetry, with 1-10 minute resolution data available on recovery of the mooring. Surface and subsurface observations utilized in this study are summarized in Table 4.1.

The uppermost temperature observation is at 1 m depth. Significant temperature gradients can develop in the upper few meters of the water column, particularly during conditions of low wind stress (Donlon et al., 2002; Ward, 2006). Thus, while we will reference the 1 m observations as being representative of a bulk SST, they do not necessarily represent the skin temperature directly associated with atmosphere-ocean heat flux.

Surface flux, and wind stress, values are calculated from mooring data using the COARE 3b bulk algorithm (Fairall et al., 2003).

4.2.2 Enhanced Monitoring Period Data

During an Enhanced Monitoring Period (EMP) from 13 October, 2008 through 17 June, 2009 the mooring was instrumented with a 600 kHz acoustic Doppler current profiler (ADCP), deployed in a downward facing position on the mooring bridle, returning horizontal velocities between 3.75 m - 35 m depth in 0.75 m vertical bins. Hourly means were formed from ensemble averages of 120 1 Hz consecutive samples at the top of the hour in order to limit the effect of mooring motion due to surface waves. Several of the near-surface ADCP bins were biased by side-lobe reflection off instruments on the mooring line. Corrupted bins were identified by visual inspection of echo intensity and vertical profiles of velocity, and were removed from subsequent analysis. ADCP velocity measurements were validated against point current meter observations at several depths, with typical correlation coefficients greater than r=0.98, and root-mean-square differences less than $3.5\,\mathrm{cm\,s^{-1}}$ (see Wenegrat et al. (2014) for additional discussion of ADCP data). An additional upward-facing 150 kHz ADCP was deployed approximately 12.5 km west of the surface mooring, measuring hourly horizontal currents in 8 m vertical bins which were then mapped to a uniform 5 m grid between 150 m and 35 m.

During the EMP the 10 m temperature sensor did not return data, however additional temperature observations were available, including observations at 13 m (Table 4.1). The 1 m salinity sensor returned data for only the first 22 days of the record, and the 5 m observations were flagged while being quality controlled and are excluded from this analysis. Near-surface salinity exhibits limited diurnal variability at this location ($\sim \pm 0.01$ psu, Drushka et al. (2014)), and correlation between the available 1 m and 20 m salinity observations was high (r=0.93). Hence, we fill the missing salinity observations through linear regression using the 20 m values. Our results are not sensitive to this choice, and a variety of alternate approaches for filling missing salinity observations, as well as density calculations based solely on temperature, were tested.

4.3 Seasonal Cycle

SST variance at the diurnal frequency is isolated using complex demodulation. This technique expresses a signal as a linear combination of a component oscillating at the frequency of interest, with slowly varying amplitude and phase, and additional variability at other frequencies which is removed by filtering (Bloomfield, 1976). Complex demodulation is applied to the 1 m temperature observations, $T_{1\,m}$, giving,

$$T_{1\,m}(t) = A(t)cos\,(\omega t - \Phi(t)) + Z(t)$$

where $A(t)$ is the diurnal SST amplitude (dSSTa), ω the diurnal frequency, $\Phi(t)$ the phase, and $Z(t)$ variability at other frequencies. The peak-to-peak diurnal SST range will thus be, 2×dSSTa. Diurnal SST maxima occur near 1400 Local Time (LT) throughout the record, so we do not discuss the phase information, $\Phi(t)$, further. An alternate estimate of dSSTa was formed by directly differencing daily maxima and minima after removing low-frequency trends (following Cronin and McPhaden (1999)). Estimates of monthly averaged dSSTa from the two methods are highly correlated (r=0.99), with regression analysis indicating a slight bias (17%) towards higher values of dSSTa using the differencing method. We thus proceed with complex demodulation as providing a conservative estimate of diurnal SST variability (uncertainty estimates for dSSTa are discussed in Appendix 4.7).

Figure 4.2a shows the clear seasonal cycle in monthly averaged dSSTa. Maximum values are found in boreal winter and spring, with typical diurnal SST ranges of 0.5-0.6 °C (dSSTa of 0.25-0.3 °C), consistent with estimates for this location derived from modeling and remote sensing studies (Stuart-Menteth, 2003; Bernie et al., 2007; Clayson and Weitlich, 2007). In boreal summer and fall the diurnal SST range is reduced to 0.2-0.3 °C (dSSTa of 0.1-0.15 °C). The seasonal cycle of dSSTa covaries inversely with the seasonal cycle of wind stress (Fig. 4.3, Fig. 4.2b), reflecting the mixing of surface heat fluxes through deeper diurnal mixed layers during periods of enhanced wind stress, as discussed in section 4.4 (Price et al., 1986; Brainerd and Gregg, 1993; Cronin and Kessler, 2002).

PIRATA temperature measurements have finer vertical resolution, and are less gappy, than salinity measurements, so for the full time series we define an isothermal mixed layer depth (MLD_T) as the depth at which temperature is $0.4\,°C$ less than the 1 m temperature, which is approximately equivalent to a density change of $0.125\,\mathrm{kg\,m^{-3}}$ (Fig. 4.2d). Alternate definitions of MLD_T were tested with similar results. The calculation of MLD_T is not linear with respect to temporal averaging, so we calculate MLD_T first using daily temperature values linearly interpolated to a 1 m grid, and subsequently take the monthly average. Additional measures of near-surface stratification are the depth of the 20 °C isotherm, a proxy for the thermocline depth (Fig. 4.2d), and the near-surface thermal stratification (ΔT), which we define as the difference between temperature observations at 1 m and 5 m (Fig. 4.2c).

Consistent with the seasonal cycle in dSSTa, these measures of near-surface stratification all exhibit a seasonal cycle driven by seasonal changes in wind stress. Wind speeds are at their maximum in boreal summer and fall, and the near-surface layer is well mixed with deep MLD_T and thermocline, and low ΔT. As the wind speed begins to drop in boreal winter the mixed layer shoals rapidly, and near-surface stratification and dSSTa increase. The thermocline also begins to shoal in boreal winter, however its response is often slower than MLD_T, with minimum thermocline depths occurring later in the seasonal cycle. This time lag reflects the basin scale dynamics involved in setting the depth of the equatorial thermocline, which linear theory predicts will respond to the zonally integrated wind stress (McPhaden, 1993), whereas MLD_T responds rapidly to local forcing.

A monthly climatology, formed from all available data, is shown in Figure 4.3. The annual pattern of monthly averaged wind stress and SWR reflects the seasonal meridional migration of the ITCZ in the Atlantic (Fig. 4.1) (Waliser and Gautier, 1993). As the ITCZ shifts south during late boreal fall and winter, SWR and wind speed both decrease. dSSTa reaches an annual monthly averaged maximum of 0.28 °C in March, despite shortwave radiation (SWR) being $31\,\mathrm{W\,m^{-2}}$ below its October maximum. Later in the year, the ITCZ shifts further north of the equator, leading to clear skies and steady trade wind conditions, associated with low dSSTa. This climatology suggests available surface heat flux is secondary to near-

surface mixing in setting the diurnal SST amplitude, with reduced wind stress, shallow mixed layers, and increased stratification during boreal winter linked to larger near surface diurnal SST signals. The precise mechanisms responsible for variations in dSSTa will be discussed further using data from the EMP in section 4.4.

Interannual variability in the Atlantic is weak compared to the seasonal cycle (Xie and Carton, 2004), and interannual anomalies of dSSTa at 0°, 23°W are of smaller amplitude than those in the Pacific (Clayson and Weitlich, 2007). Using similar moored data at 0°, 110°W, Cronin and Kessler (2002) observed interannual variability of the diurnal SST amplitude on the order of $\pm 0.1\,^{\circ}\mathrm{C}$ associated with the El-Niño Southern Oscillation. The primary modes of interrannual variability in the tropical Atlantic are the Atlantic Meridional Mode and the zonal Atlantic Niño Mode (Servain, 1991; Zebiak, 1993). Although the time-range of observations covers both positive and negative Atlantic Meridional Mode and Atlantic Niño events, we do not observe monthly average dSSTa values exceeding $\pm 0.05\,^{\circ}\mathrm{C}$ from the climatological values.

4.4 Enhanced Monitoring Period

Atmosphere and ocean conditions during the 8-month EMP are summarized in Figure 4.4. The EMP began in October 2008, during a regime characterized by steady southeast trade winds, limited precipitation, and average dSSTa of $0.13\,^{\circ}\mathrm{C}$. In early January, winds became lighter and more variable in direction and there was more frequent rain and cloudiness (Fig. 4.4b, c), with significant variance of dSSTa on sub-monthly timescales. This basic seasonality is consistent with the climatology (Fig. 4.3), although in boreal spring 2009 the ITCZ shifted anomalously far south due to a strong negative AMM event, leading to negative anomalies in wind speed magnitude ($-1\,\mathrm{m\,s^{-1}}$) and SWR ($-30\,\mathrm{W\,m^{-2}}$) at 0°, 23°W, as well as anomalously high sea surface height and SST across the equatorial basin (Foltz and McPhaden, 2010; Foltz et al., 2012). After the period of variable winds, steady trade winds were re-established, followed by a dramatic $5\,^{\circ}\mathrm{C}$ cooling of the cold tongue region between June and August attributed to upwelling dynamics (Foltz and McPhaden, 2010). Conditions

during boreal spring 2009 are thus not entirely representative of a typical year, although the limited dSSTa anomalies during this period (Figure 2) suggests that diurnal variability may not have been as strongly atypical.

Zonal velocity is dominated by the strong eastward flowing undercurrent in the thermocline exceeding $1\,\mathrm{m\,s^{-1}}$, with the westward South Equatorial Current above it in the surface layer. This results in a high shear region on the upper flank of the undercurrent core below the mixed layer (MLD), which is defined during the EMP as the depth at which density first exceeds the 1 m value by $0.01\,\mathrm{kg\,m^{-3}}$. The limited vertical resolution of the PIRATA mooring adds uncertainty to the calculation of MLD, however this criteria was found to best identify the diurnal mixed layer based on visual inspection of density profiles, was highly correlated with other more generous definitions of MLD, and provides consistency with prior work (Brainerd and Gregg, 1995). Meridional velocity is generally small, except during the passage of several tropical instability waves (TIWs) in the early part of the record, evident in the alternating north-south flow with period of approximately 30 days (Legeckis, 1977; Grodsky, 2005). Below the mixed layer, buoyancy frequency squared ($N^2 = -\rho^{-1} g \rho_z$) increases downwards towards the thermocline, with near-surface enhancement during the southward phase of a TIW in November 2008.

To quantify the likelihood of shear driven mixing, we use reduced shear squared, defined as,

$$S^2_{red} = u_z^2 - 4N^2$$

where u_z is the vertical shear of horizontal currents. To account for uneven spacing of temperature, salinity, and velocity observations, S^2_{red} is calculated using first differences with a vertical separation of 5.25 m between 3.75-30 m and 10 m separation below 30 m. Errors in the calculated values of S^2_{red} can arise from a variety of sources, including instrument noise, horizontal separation between the deep ADCP and temperature and salinity measurements, and the coarse vertical resolution. These sources of error are addressed in Appendix 4.8, and while they introduce significant uncertainty into the hourly estimates of S^2_{red}, they do not

alter the basic interpretation of the statistics used in this analysis.

S^2_{red} is simply a rearrangement of the Richardson number ($Ri = N^2 u_z^{-2}$), such that when $S^2_{red} > 0, Ri < 0.25$. Thus, when S^2_{red} is positive it implies flow regimes that are unstable to shear instabilities, whereas negative values imply stability. For our purposes, characterizing the flow as stable or unstable, S^2_{red} is preferable to Richardson number as it linearizes the effect of observational errors in velocity shear, its distribution is less skewed than the Richardson number, and it retains additional information about the kinetic energy of the flow (Hazel, 1972; Kunze et al., 1990; Sun et al., 1998). It is worth noting that the true stability boundary for stratified shear flows is not solely a function of the Richardson number, and may depend on the turbulent Reynolds number, as well as pre-existing turbulence in the flow (Smyth et al., 2013). However, defining a critical value of $Ri = 0.25$ ($S^2_{red} = 0$) is a common and useful first approximation.

Throughout the EMP, S^2_{red} is elevated between the surface and the thermocline, due to high near-surface shear and low near-surface stratification. During steady trade wind conditions there is an approximately 40 m thick layer below the mixed layer where $S^2_{red} \approx 0$, indicating marginal instability and potentially active deep-cycle turbulence (Smyth et al., 2013), which is discussed further in Section 4.5. A thinner marginally stable layer, approximately 15 m thick, persists throughout the variable wind conditions, following the shoaling of the equatorial undercurrent and thermocline (Fig. 4.4i).

A sample 7 day period of hourly data, taken when the trades were relatively steady during the cold phase of a TIW, clearly demonstrates the diurnal cycle of near-surface shear and stratification (Fig. 4.5). The daily cycle of solar insolation leads to rapid morning shoaling of the mixed layer, and increasing thermal stratification that begins at the surface, and penetrates deeper into the water column as the day progresses. This thermal stratification inhibits the vertical transfer of momentum from the wind, leading to intensified near surface shear (Price et al., 1986; Bond and McPhaden, 1995). Beginning between 1200 and 1400 LT, the mixed layer begins to deepen. This occurs before the surface heat flux has changed sign, and is associated with positive values of S^2_{red}, suggesting shear instability as a mechanism

for this deepening. While there is significant temporal and spatial variability, as well as uncertainty, in our hourly estimates of S^2_{red}, this picture is qualitatively similar to recent observations from the Pacific, where descending diurnal shear layers associated with sub-critical Richardson numbers were shown to provide an initiation mechanism for deep-cycle turbulence (Smyth et al., 2013).

In order to further examine the dynamics of the diurnal mixed layer, we divide the EMP into two regimes. The early part of the record is characterized by relatively steady trade winds, clear skies, deep mixed layers and thermocline, and marginal instability of the upper equatorial undercurrent. In contrast, the latter part of the record exhibits weaker and more variable winds, frequent cloudiness and precipitation, shallow mixed layers, and a shoaling of the undercurrent and thermocline. Diurnal composites for these two regimes are described in the following two sections.

4.4.1 Steady Trade Wind Conditions

A composite diurnal cycle over the upper 30 m is formed by phase averaging hourly observations from 13 October 2008 through 6 January 2009. Wind stress and horizontal currents are vector averaged, and horizontal currents referenced to the 20 m values, giving the sheared component of the flow. Temperature observations are phase averaged, and the time-depth mean removed to give the diurnal anomaly. We define an eddy viscosity, A_v, using the shear-stress surface boundary condition, $\rho A_v u_z = \tau$, where ρ is the density of seawater, u_z is the vertical shear magnitude, and τ is the surface wind stress magnitude. This can be rearranged to give an equation for A_v (Santiago-Mandujano and Firing, 1990; Wenegrat et al., 2014),

$$A_v = \frac{\tau}{\rho u_z}, \qquad z = 0$$

We evaluate this using the uppermost valid velocity observations, giving a nominal shear depth of 5.64 m. This approach can be treated as an assumption of uniform stress between the surface and 5.64 m, and thus the value of A_v we infer will be approximate. It can be

considered analogously to the mixing length scaling of Prandtl, which defines a mixing length, l, based on dimensional considerations as the ratio between friction velocity, $u_* = (\tau\rho^{-1})^{1/2}$, and shear, $l = u_* u_z^{-1}$ (Stull, 1950). Thus, $A_v = l^2 u_z$. The distribution of A_v is highly skewed, with a small number of very large values occurring as $u_z \to 0$, and hence values which exceed the 99th percentile ($A_v \geq 0.045\,\mathrm{m^2\,s^{-1}}$), estimated using the bootstrap method (Efron and Tibshirani, 1993), are excluded prior to compositing using the geometric mean.

Figure 4.6 shows the diurnal composite for the steady trade wind period. Surface heat flux becomes positive into the mixed layer shortly after 0600 LT, leading to a rapid shoaling of the mixed layer from 13 m to 3.5 m. Near surface temperature begins to rise, and a diurnal jet develops in the downwind direction. At 1400 LT, SST reaches its maximum diurnal amplitude of 0.18 °C and shortly after, at 1500 LT, surface shears reach $20\,\mathrm{cm\,s^{-1}}$ relative to the 20 m currents. As there is limited diurnal variance in the wind, the afternoon maximum of near-surface shear is associated with a daily minimum of $A_v = 3.3 \times 10^{-3}\,\mathrm{m^2\,s^{-1}}$, reduced more than a factor of 2 from nighttime values (Wenegrat et al., 2014). In the late afternoon the mixed layer begins to deepen, A_v increases, and diurnal temperature anomalies are spread over an increasingly deep mixed layer, limiting the magnitude of the dSSTa, as noted in Section 4.3 (Price et al., 1986; Bond and McPhaden, 1995).

Composites of S^2_{red} are presented in terms of the fraction of hourly observations in each time-depth bin that are unstable to shear instability ($S^2_{red} > 0$, Fig. 4.7) which we denote as $\mathcal{F}(S^2_{red})$. During steady trade wind conditions there is a clear diurnal cycle of S^2_{red}, with an increasingly stable near-surface layer formed at the surface and penetrating deeper into the layer as the day progresses. Minimum daily values of $\mathcal{F}(S^2_{red})$ are found at 1000 LT at 6.37 m depth, and at 1900 LT at 22.12 m depth. $\mathcal{F}(S^2_{red})$ increases throughout the afternoon, and by 1600 LT, shortly before the surface heat flux changes sign, approximately 40% of observations in the upper 20 m have unstable values of S^2_{red}. The deepening of the mixed layer, which begins midday, along with increased $\mathcal{F}(S^2_{red})$, suggest that shear instabilities may be forming in the diurnal shear layer. After the surface heat flux changes sign the mixed layer continues to deepen, and $\mathcal{F}(S^2_{red})$ increases as a result of convective mixing.

4.4.2 Variable Wind Conditions

The diurnal composite formed during the period of variable wind forcing, 7 January 2009 through 24 May 2009 exhibits a very different evolution (Fig. 4.8). Consistent with the climatological pattern (Fig. 4.3) maximum net heat flux is reduced by $128\,\mathrm{w\,m^{-2}}$, and wind speed by $2.7\,\mathrm{m\,s^{-1}}$, compared to the steady trade wind conditions. Diurnal temperature variations are strongly surface trapped, with peak diurnal SST amplitude reaching $0.3\,^{\circ}\mathrm{C}$ at 1400 LT and persisting later in the day than during steady wind conditions. Corresponding to this, the mixed layer remains shallow throughout both day and night, and does not display the rapid afternoon deepening seen in the stronger wind conditions. A_v is reduced to approximately $10^{-3}\,\mathrm{m^2 s^{-1}}$, and lacks a significant diurnal cycle, indicating less near-surface mixing than during steady wind conditions. Despite the absence of strong wind forcing, the near-surface layer remains highly sheared below the mixed layer, resulting from the shallow equatorial undercurrent.

Above 20 m, S^2_{red} undergoes a diurnal cycle (Fig. 4.9) controlled by changes in stratification (Fig. 4.8). During daytime hours the near-surface layer becomes increasingly stable, with the daily minimum $\mathcal{F}(S^2_{red})$ persisting until 1400 LT, much later than during the steady wind conditions. A pre-dawn enhancement of $\mathcal{F}(S^2_{red})$, similar to that observed during the steady trade wind conditions, can be attributed to nighttime convective mixing that decreases near-surface stratification. Below 20 m, isopleths of $\mathcal{F}(S^2_{red})$ show only a slight diurnal cycle, suggesting limited vertical penetration of surface forced diurnal anomalies.

4.4.3 Tropical Instability Waves

After the seasonal cycle, the most prominent timescale of variability during the EMP is that associated with the passage of several TIWs from October through January (Fig. 4.4f). During TIWs, alternating north-south meridional flow with period of approximately 30 days advects the background SST gradient (Fig. 4.1) and modifies near surface S^2_{red} through changes in both u_z and N^2 (Weisberg and Weingartner, 1988; Jochum et al., 2004; Grodsky,

2005; Moum et al., 2009). TIWs are also known to modulate equatorial turbulence (Lien et al., 2008; Moum et al., 2009), with enhanced mixing during the transition from north (cold SST) to south (warm SST) phases (Lien et al., 2008; Inoue et al., 2012). In our data, winds remain relatively steady across TIW phases (see Chelton and Xie (2010) for a discussion of TIW-atmosphere coupling), and while TIWs change the local SST, there is only limited TIW modulation of dSSTa (Fig. 4.4a, and Cronin and Kessler (2002)). However, subsurface conditions differ dramatically by TIW phase, as is evident in Figure 4.10, which shows the passage of a TIW, beginning in the cold (north) phase, progressing into the warm (south) phase around 31 October, and then returning to a cold phase around 16 November.

During the cold phases, diurnal cycling of the MLD is pronounced, with nighttime mixed layers reaching 20-40 m and daytime mixed layers shoaling to less than 5 m. Stratification and shear are enhanced along the base of the mixed layer, and a layer of elevated S^2_{red} extends from the mixed layer towards the core of the undercurrent in the thermocline. In the warm phase of the TIW SST warms by approximately 1.5 °C (Fig. 4.10b), and there is a reduction in net surface heat flux (Fig. 4.10a). During this phase of the TIW the diurnal SST anomaly does not change appreciably from the cold phase. However a subsurface diurnal cycle is less evident, with a consistently shallow mixed layer and a less clearly defined diurnal cycle of S^2, potentially due to our inability to resolve velocity above 3.75 m.

Additionally, during the warm phase the layer of enhanced S^2_{red} below the mixed layer bifurcates into two distinct layers, separated by a thin region of stable S^2_{red} centered at approximately 40 m depth. Moum et al. (2009) first noted this feature in the tropical Pacific, and termed the lower of these layers the upper core layer. They found the upper core layer continued to show enhanced turbulent dissipation, but appeared to be dynamically isolated from the surface-forced diurnal cycle. While qualitatively similar to the upper core layer observed in the Pacific, the layer observed here is thinner, and does not appear as distinctly isolated from the near-surface layer of elevated shear, potentially due to the shallower thermocline at this location or our lower resolution observations (Inoue et al., 2012). We also observe an enhancement of S^2_{red} at the base of the deep-cycle layer during the cold phase,

due in part to enhanced meridional shear.

The composite diurnal cycle of section 4.4.1 will average across TIWs, so here we segment by TIW phase. The 0°, 23°W mooring does not evenly sample all TIW phases, being offset to the south from the center of the TIW wave midline, as determined from satellite SST imagery. Hence, we divide the observations into only two phases, a cold phase on 15 October through 30 October, and a warm phase from 31 October through 15 November.

In the cold phase of the wave, S^2_{red} undergoes a very clearly defined diurnal cycle (Fig. 4.11a). The nighttime near-surface layer has low stratification, and 86% of observations at 5.26 m have $S^2_{red} > 0$ at 0300 LT. Following dawn, the upper water column rapidly stabilizes due to thermal stratification. The afternoon increase of shear, leading to increased $\mathcal{F}(S^2_{red})$, that was discussed in section 4.4.1 is even more clearly defined during the TIW cold phase. At 1300 LT the mixed layer begins to deepen, along with rapidly increasing $\mathcal{F}(S^2_{red})$, suggesting that shear instabilities are eroding the diurnal thermal stratification.

The composite diurnal cycle is very different during the warm phase of the TIW, where the warmer, more strongly stratified, near-surface layer is more stable throughout the diurnal cycle (Fig. 4.11b). $\mathcal{F}(S^2_{red})$ is reduced at all hours, and only a weak diurnal cycle of S^2_{red} is apparent above 15 m depth. However, the low dSSTa during this phase of the TIW suggests that a similar wind-driven mixing is continuing to occur in the shallow mixed layer above our observation depths, with limited vertical penetration of the diurnal shear layers.

4.5 Marginal Instability

Recent work using long moored measurements of dissipation at 0°, 140°W suggests that flows with Richardson numbers distributed around the critical value of 0.25, a form of statistical equilibrium termed marginal instability, may indicate regimes where deep cycle turbulence is active (Thorpe and Liu, 2009; Smyth et al., 2013). While the existence of marginal instability does not quantify the strength of turbulence, it is particularly well suited to evaluation from moored records. Smyth et al. (2013) demonstrate that increasing the vertical separation over which Richardson number is calculated alters the skewness of the resulting distribution, but

does not eliminate the distribution's peak near the critical value. Consequently, marginal instability continues to be clearly identifiable regardless of vertical scale. Deep-cycle turbulence is one of the defining features of the diurnal cycle on the equator and, as we lack direct measurements of dissipation, we can use measures of marginal instability as a proxy for the existence of active deep-cycle turbulence.

Figure 4.12 shows median profiles of S^2_{red} for the two wind forcing regimes, as well as the distribution of observations in the 22-50 m depth range. During steady trade wind conditions there is a 40 m thick layer below the mixed layer where $S^2_{red} \approx 0$, while during variable wind conditions this same layer becomes increasingly stable with depth. This is further illustrated in Figure 4.12b, where the distribution of S^2_{red} is sharply peaked around 0 for the steady trade wind conditions, while it is skewed towards more negative (stable) values when the winds are light and variable. Figure 4.12c shows this same shift in distribution in terms of Richardson number. This shift in the stability of the equatorial undercurrent layer below the mixed layer suggests a seasonal cycle in deep-cycle turbulence, which is discussed further below.

Additional shorter time-scale variability in the stability of the near-surface layer is also distinguishable in Fig. 4.4i. Notably, the thick layer of $S^2_{red} \approx 0$ below the mixed layer during steady wind conditions persists into late January, well after the change in local wind stress, and cessation of the strong diurnal cycle of shear flow. This occurs coincident with the south phase of a TIW (Fig. 4.4f), with a large component of the total shear coming from shear in the 20-40 day period band, including significant contributions from the meridional component. This enhanced shear, along with a deep thermocline, contributes to the persistence of marginal instability above 50 m, despite the absence of strong local surface forcing and diurnal shear layers.

Estimates of the turbulent dissipation rate, ϵ, below the mixed layer can be formed using parameterizations based on S^2_{red}, or Richardson number. While a comparison of dissipation parameterizations is beyond the scope of the present work, for completeness we apply the turbulence parameterization of Kunze et al. (1990) to provide a quantitative estimate of the

turbulent mixing implied by the marginal instability noted above. This parameterization is based on the energetics of Kelvin-Helmholtz instabilities, and gives,

$$\epsilon_{KWB} = \frac{\Delta z^2}{96} \left\langle u_z^2 - \frac{N^2}{Ri_c} \right\rangle \left\langle u_z - \frac{N}{\sqrt{Ri_c}} \right\rangle$$

Where $\langle x \rangle = 0$ if $x \leq 0$ and $\langle x \rangle = x$ for $x > 0$, and Δz is the vertical separation over which u_z and N are calculated (Kunze et al., 1990; Peters et al., 1995; Polzin, 1996). The critical Richardson number, Ri_c, was assumed in Kunze et al. (1990) to be 0.25, however it may also be treated as a free parameter to account for observational constraints such as vertical resolution (Polzin, 1996). We present results for several possible choices of Ri_c (Fig. 13), with $Ri_c = 0.4$ suggested based on the vertical scale of our observations (Polzin, 1996). Ocean turbulence statistics are highly skewed (Peters and Gregg, 1988), hence estimates of average ϵ_{KWB} are formed using the trimmed mean, excluding the highest and lowest 5% of hourly observations before averaging, which provides a robust estimator of central tendency for heavy-tailed distributions (Wilcox, 2010).

Calculated values of ϵ_{KWB} demonstrate a seasonal cycle of turbulence, regardless of choice of Ri_c, with elevated ϵ_{KWB} during the steady trade wind conditions, and values decreasing by 1-2 orders of magnitude during the variable wind regime in boreal spring (Fig. 13). We note that ϵ_{KWB} is enhanced at high S_{red}^2 and thus also follows a diurnal cycle similar to that discussed in Section 4.4. The seasonal modulation of turbulent dissipation, and marginal instability, below the mixed layer indicates a seasonal cycle of deep-cycle turbulence in the central Atlantic broadly consistent with estimates derived from heat budgets at this location (Foltz, 2003; Hummels et al., 2014), and similar to the seasonal cycle of dissipation observed at 0°, 10°W in the eastern Atlantic (Hummels et al., 2013), and at 0°, 140°W in the Pacific (Moum et al., 2013; Smyth et al., 2013). Further, these finding suggests in-phase seasonal variability of the marginally unstable layer and the prominence of diurnal shear layers.

4.6 Summary

We have provided an assessment of diurnal SST, near-surface shear, and stratification at 0°, 23°W in the central equatorial Atlantic using a 15 year time series in conjunction with an 8-month enhanced monitoring period of high-vertical resolution velocity observations. Major results can be summarized as follows:

1) The diurnal cycle of SST in the central equatorial Atlantic is strongly modulated by wind-stress, with climatological monthly mean diurnal SST amplitude reaching 0.28 °C during the light and variable wind conditions prevalent in boreal winter and spring. Climatologically, the highest diurnal range in SST occurs during periods of reduced SWR, suggesting that wind driven mixing determines the seasonal modulation of diurnal SST amplitude. Interannual variability of diurnal SST amplitude at this location is small compared to the seasonal cycle.

2) During relatively steady trade wind conditions, we regularly observe descending diurnal shear layers, corresponding to an increased frequency of $S^2_{red} > 0$ ($Ri < 0.25$). The mixed layer frequently begins to deepen while the surface heat flux is still into the ocean, suggesting that instabilities of the sheared diurnal jets are mixing the near surface layer. This mixing reduces the maximum achievable diurnal SST amplitude by spreading heat over deeper layers. During light and variable wind conditions we see a near-surface diurnal cycle of S^2_{red}, resulting primarily from diurnal variability of N^2. Mixed layers are shallow and diurnal temperature anomalies are strongly surface trapped, resulting in larger diurnal SST signals.

3) TIWs modulate the diurnal cycle in the mixed layer of the tropical Atlantic. During the cold (north) phase, subsurface conditions resemble a more clearly defined version of those described earlier in relation to the steady trade winds period. In the warm (south) phase, the mixed layer shoals and there is not a well defined diurnal cycle of shear flow at our uppermost observation depth of 6.37 m. Negligible TIW modulation of diurnal SST amplitude is found, suggesting that similar wind-driven mixing continues above our observation depth, albeit with limited vertical penetration of the diurnal shear layers.

4) Concurrent with the descending diurnal shear layers observed during steady trade wind conditions, we observe marginal instability of an approximately 40 m thick layer below the mixed layer and above the thermocline. The strength of this layer appears to vary seasonally, tracking the shoaling thermocline and thinning substantially during the period of reduced wind stress in boreal winter. This property of marginal instability, along with the estimated turbulent dissipation rates, suggests a seasonality of deep cycle mixing that agrees with prior estimates of the seasonal cycle of mixing in the equatorial Atlantic (Foltz, 2003; Hummels, 2012; Hummels et al., 2013, 2014) and the equatorial Pacific (Smyth et al., 2013). After the seasonal relaxation of local surface wind stress we observe an approximately two week period where enhanced vertical shear during the south phase of a TIW contributes to the maintenance of a thick marginally unstable layer in the absence of diurnal shear variance.

These findings provide observational confirmation of prior diurnal cycle modeling work (Skielka et al., 2011; Wade et al., 2011), and indicates that many of the same dynamic processes that have been studied in the Pacific may also be active in the Atlantic (Gregg et al., 1985; Moum and Caldwell, 1985; Peters et al., 1994; Sun et al., 1998). In particular, observations of diurnal shear layers descending into the marginally unstable undercurrent layer suggests that we see both a mechanism for the initiation of deep-cycle turbulence (Smyth et al., 2013; Pham et al., 2013), as well as the resulting footprint on the flow stability (Smyth et al., 2013). The regular occurrence of descending diurnal shear layers throughout the 2.5 months of observations during steady trade wind conditions can also be considered as evidence for the suggested role of diurnal shear in initiating deep-cycle turbulence, a finding enabled by the unique long moored-ADCP record of near-surface currents we utilize here. Currently, the limited dissipation measurements in the central equatorial Atlantic have been inconclusive in characterizing the diurnal cycle of turbulence (Crawford and Osborn, 1979; Hummels, 2012; Hummels et al., 2013, 2014). However our findings suggest that future measurements are warranted, and will provide a useful point of comparison and contrast with the existing literature from the Pacific.

4.7 Appendix A: Uncertainty in dSSTa

The good agreement between complex demodulated dSSTa and estimates derived from direct differencing of daily maxima and minima gives us a basic level of confidence in our approach of estimating dSSTa (Section 4.3). Additional uncertainty estimates for the complex demodulated dSSTa can be formulated using Monte Carlo simulation. Complex demodulation was performed on repeated realizations of a synthetic signal, consisting of a diurnal oscillation of known amplitude plus Gaussian white noise with variance scaled to match the SST observations in a spectral window surrounding the diurnal frequency, excluding the diurnal peak (Pawlowicz et al., 2002). Standard errors are then estimated from the synthetic signals using the median absolute deviation, and are found to be a very weak function of amplitude. Hence, 95% confidence intervals on the complex demodulated diurnal SST amplitude are well approximated by a constant value, $\pm 0.031\,^{\circ}\mathrm{C}$ for daily averaged estimates.

4.8 Appendix B: Errors in S^2_{red}

We consider errors in calculated values of S^2_{red} arising from three sources: instrumental noise, the approximately 12.5 km horizontal separation between the deep ADCP mooring and the surface mooring on which temperature and salinity observations were made (Section 4.2.2), and the vertical resolution of the observations.

4.8.1 Instrumental Noise and Horizontal Separation

We assume that instrumental noise, and horizontal separation, can be treated as additive errors, such that $u_{obs} = u + \epsilon_u$, and $\rho_{obs} = \rho + \epsilon_\rho$.

Above 35 m, ϵ_u will result solely from instrumental error, which can be calculated using the published single-ping variance for the 600 kHz ADCP configured as deployed, giving $\epsilon_u = 8.7 \times 10^{-3}\,\mathrm{m\,s^{-1}}$ for ensemble averaged values. Below 35 m, ϵ_u will consist of both instrumental error and errors due to the approximately 12.5 km horizontal separation between the ADCP mooring and the surface mooring. The upward and downward facing ADCPs have

overlapping velocity observations at 35 m depth, and hence we can treat the RMS difference between these observations as representing error due to horizontal separation. Using this approach we find $\epsilon_u = 0.17\,\mathrm{m\,s^{-1}}$. This value is also roughly consistent with alternate estimates derived by adopting Taylor's frozen turbulence hypothesis, equating temporal shifts with horizontal separation (*see also* Smyth et al. (2013)*, their Supplementary Information*).

The value of ϵ_ρ is calculated in a similar manner, using the ATLAS mooring temperature (salinity) sensor accuracy of $\pm 0.02\,^\circ\mathrm{C}$ (± 0.02) (Freitag et al., 2005). A linearized equation of state is used to give $\epsilon_\rho = 6.4 \times 10^{-3}\,\mathrm{kg\,m^{-3}}$ for ensemble hourly averages of 10 minute data. This estimate is likely conservative, as it applies post-deployment sensor drift errors to the entire observational period (Freitag et al., 2005).

The effect of these observational errors on finite difference calculations can be assessed using,

$$\epsilon_z = \frac{\sqrt{2}\epsilon}{\Delta z} \tag{4.1}$$

where we have assumed that errors are uncorrelated across depth bins. Application of 4.1 gives, $\epsilon_{u_z} = 2.3 \times 10^{-3}\,\mathrm{s^{-1}}$ ($\epsilon_{u_z} = 2.4 \times 10^{-2}\,\mathrm{s^{-1}}$), and $\epsilon_{N^2} = 1.7 \times 10^{-5}\,\mathrm{s^{-2}}$ ($\epsilon_{N^2} = 8.7 \times 10^{-6}\,\mathrm{s^{-2}}$) for hourly estimates above (below) 35 m.

These values are then used in the propagation of errors formula to give an estimate of the total error in an hourly calculated value of S^2_{red},

$$\epsilon_{S^2_{red}} \approx \left[\left(\frac{\partial S^2_{red}}{\partial u_z} \epsilon_{u_z} \right)^2 + \left(\frac{\partial S^2_{red}}{\partial N^2} \epsilon_{N^2} \right)^2 \right]^{\frac{1}{2}} = 2 \left[u_z^2 \epsilon_{u_z}^2 + 4\epsilon_{N^2}^2 \right]^{\frac{1}{2}} \tag{4.2}$$

where we have ignored a term involving the covariance between u_z and N^2 as it is found to be small compared to other terms. Using average values for u_z, we find errors in hourly calculated values of S^2_{red} on the order of $1.1 \times 10^{-4}\,\mathrm{s^{-2}}$ ($8.9 \times 10^{-4}\,\mathrm{s^{-2}}$) above (below) 35 m depth. Uncertainties of this magnitude do not alter the interpretation of the statistics used in this analysis.

4.8.2 Vertical Resolution

The effect of the vertical separation between instruments, in particular the coarse resolution of temperature and salinity, cannot be assessed directly using our data. However, previous work suggests that the effect of lowering vertical resolution on the calculation of Richardson number is to alter the skewness of the distribution, rather than fundamentally altering the basic shape of the probability distribution (Smyth et al., 2013). We thus expect that the coarse mooring vertical resolution will shift the calculated S^2_{red} towards more stable values, without qualitatively changing our major findings.

It is possible to estimate the effect of vertical resolution on the calculation of N^2 in the upper 100 m using 38 available CTD casts from the World Ocean Database (Boyer, 2013) within $\pm 1^\circ$ of latitude and longitude of the mooring that have vertical resolution of at least 1 m and the first observation above 40 m depth. To accomplish this, estimates of N^2 are calculated for each CTD profile using the full resolution of the profile, which we treat as representing the true N^2. CTD observations of temperature and salinity are then decimated to observation depths consistent with the mooring sampling scheme, and new N^2_{dec} are calculated. Differences between these values can be considered as errors due to the vertical sampling scheme employed by the PIRATA mooring.

Values of N^2 and N^2_{dec} calculated in this manner are well correlated above 30 m (r=0.78), and over the upper 100 m (r=0.62). We use robust linear regression of the form $N^2_{dec} = \hat{\beta} N^2 + \epsilon$, where ϵ are the errors in N^2_{dec} that we seek to minimize. Applying this to the CTD data between the surface and 100 m depth gives, $\hat{\beta} = 0.84$, suggesting a low bias in N^2_{dec}. We re-ran the analysis of this study after adjusting the observed values of N^2 to account for this bias, and found that the major results are robust to this change. Further, alternate values of $\hat{\beta}$ ranging from 0.5 to 1.5 were tested, and the results were found to be qualitatively robust to these adjustments.

Table 4.1: Summary of 0°, 23°W data.

Surface Observations

Observation	Height (m)	Sampling Frequency
Wind speed/direction	4	10 minute
SWR	3.5	2 minute
LWR	3.5	2 minute
Rain	3.5	10 minute
Air temperature	3	10 minute
Relative Humidity	3	10 minute

Subsurface Observations

Observation	Depth (m)	Sampling Frequency
Temperature	1, 5, 10[b], 13[a], 20,23[a], 40, 60, 80, 100, 120	10 minute
Salinity	1[b], 5[b], 20, 40, 60, 80, 100, 120	10 minute
600 kHz ADCP[a]	3.75 - 35 (0.75 m bins)[a]	Hourly (120×1 Hz ensemble)
150 kHz ADCP[a]	35 - 150 m (8 m bins)	Hourly (45×0.0125 Hz ensemble)

[a] Enhanced Monitoring Period

[b] Partial data availability, see section 4.2.2

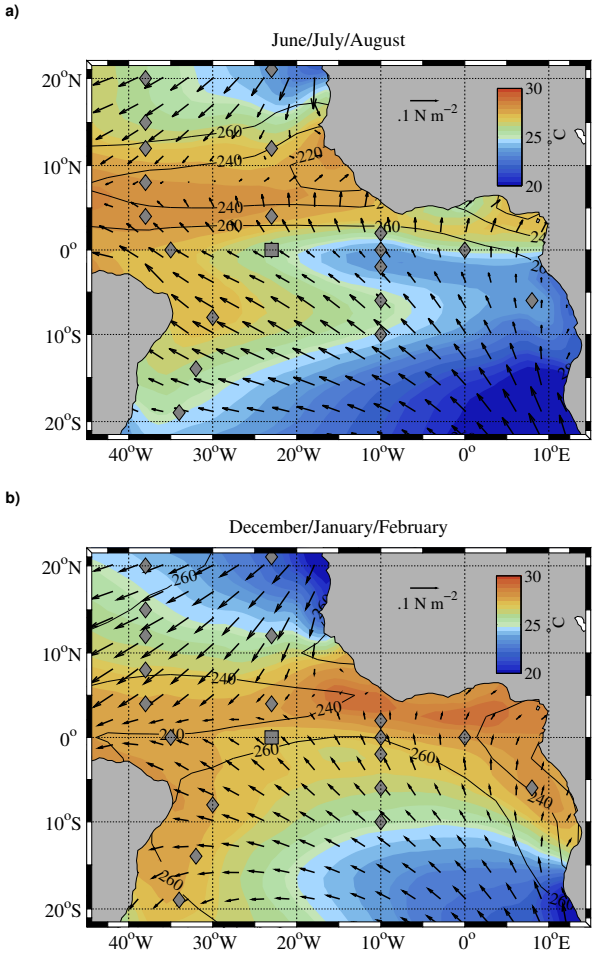

Figure 4.1: Location of the Prediction and Research Moored Array in the Tropical Atlantic moorings (grey diamonds, study location gray square), with seasonal average variables for a) boreal summer (June, July, August) and b) boreal winter (December, January, February). Colorscale: Sea surface temperature (SST) from 1999 to 2014 from NOAA Optimally Interpolated SST version 2 (Reynolds et al., 2002). Vectors: wind stress from 1999 to 2009 from the Scatterometer Climatology of Ocean Winds (Risien and Chelton, 2008), with scale shown on plot. Contours: NOAA interpolated top of atmosphere Outgoing Longwave Radiation (OLR, values shown on contours in units of Wm^{-2}) from 1999 to 2014 (Liebmann, 1996).

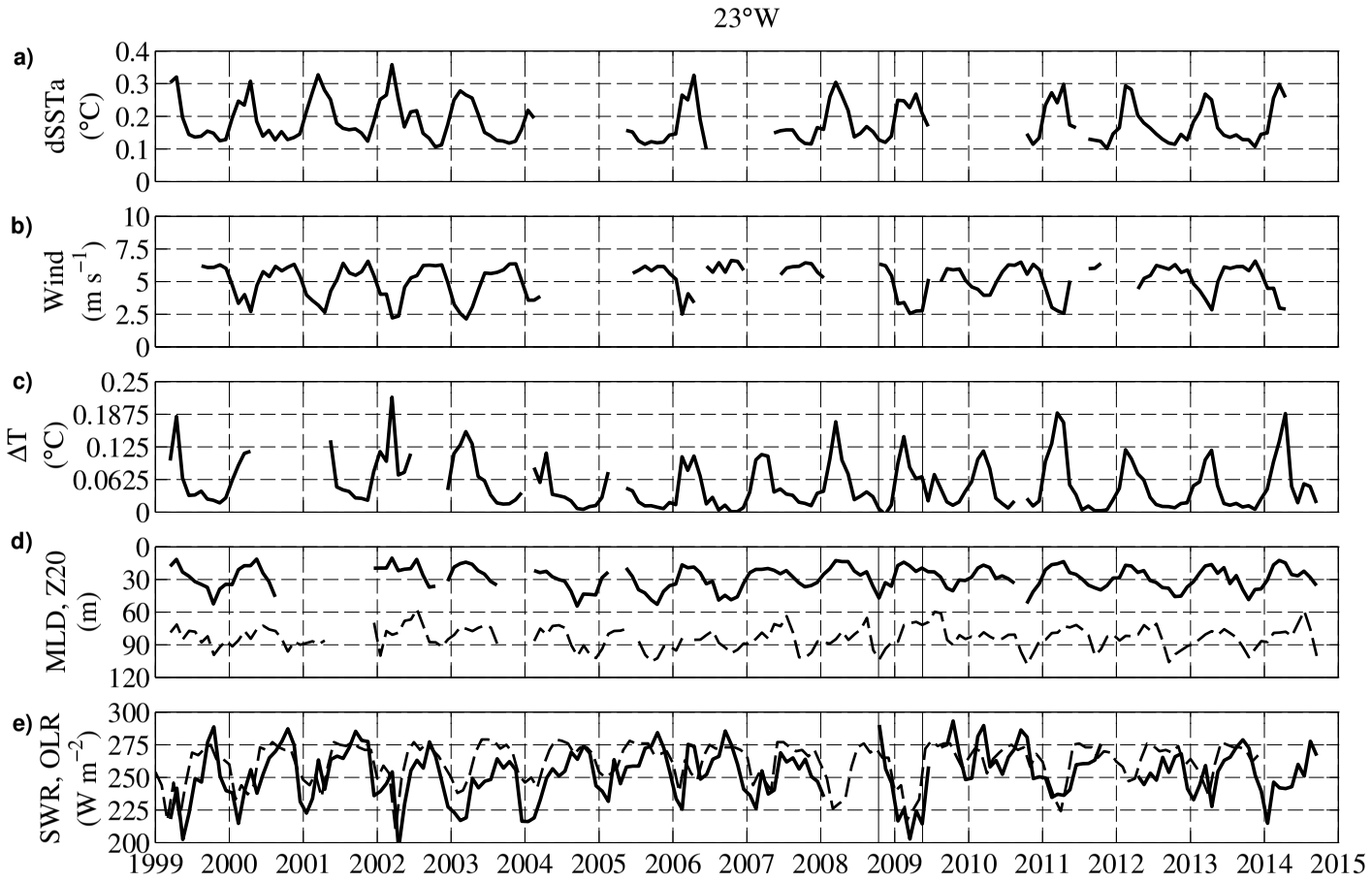

Figure 4.2: Overview of the full monthly averaged timeseries, a) diurnal SST amplitude (dSSTa), b) wind speed, c) thermal stratification ($\Delta T = T_{1\,m} - T_{5\,m}$), d) isothermal mixed layer depth (solid line, $\Delta T = 0.4$°C) and depth of the 20°C isotherm (dashed line), e) downwelling short wave radiation (solid line) and top of atmosphere outgoing longwave radiation (dashed line) (Liebmann, 1996). Solid vertical lines denote the enhanced monitoring period (section 4.4).

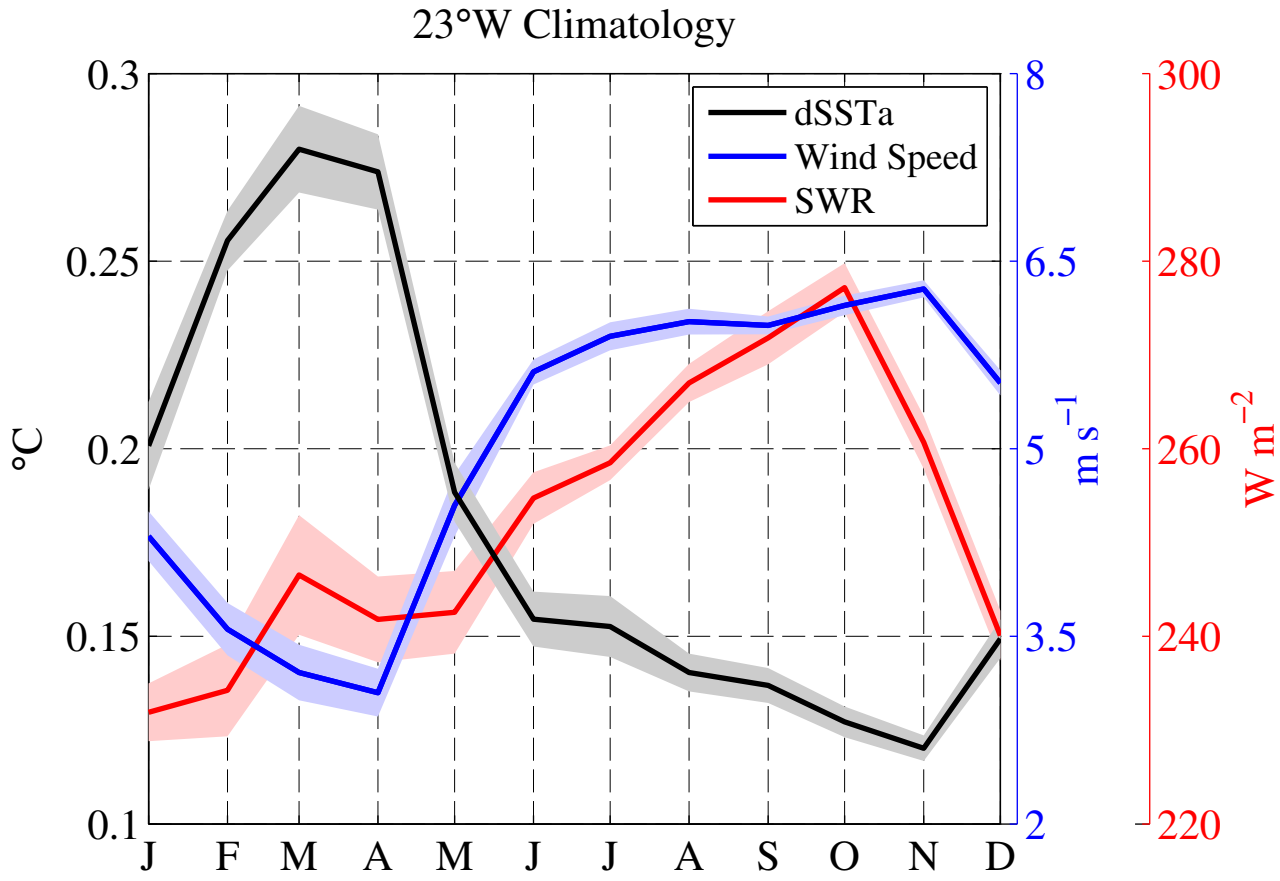

Figure 4.3: Monthly averaged climatology for diurnal SST amplitude (black line), wind speed (blue line), and short wave radiation (red line). Shading denotes ± one standard error of the mean.

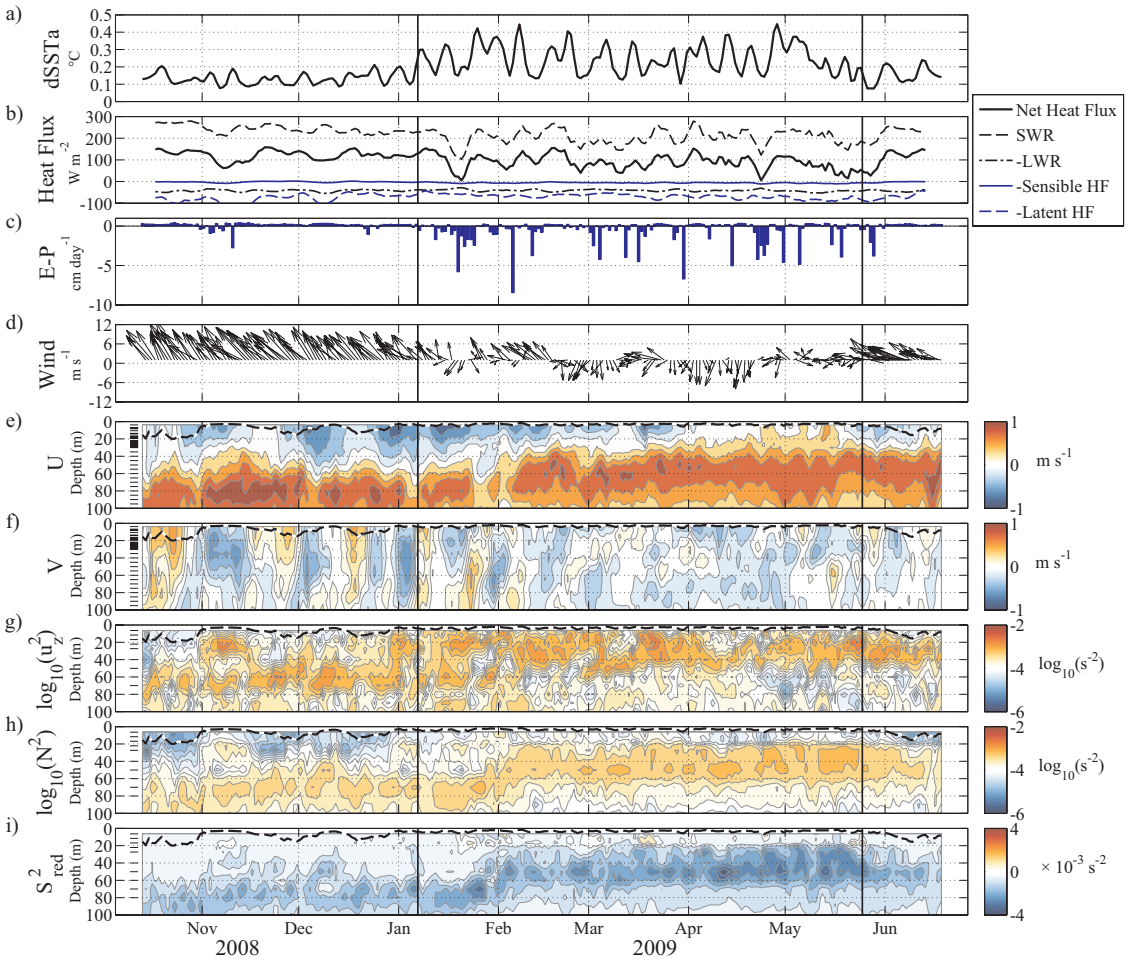

Figure 4.4: Overview of atmosphere and ocean conditions during the EMP using daily averaged data. a) Diurnal SST amplitude (dSSTa) smoothed with a 5-day moving average, b) smoothed net surface heat flux (solid black line) defined positive into the mixed layer with components as indicated in the legend, c) evaporation minus precipitation, d) wind vectors (magnitude indicated by vector length with scale on the ordinate, direction indicated by vector orientation with north up), e) zonal velocity, f) meridional velocity, g) $log_{10}(u_z^2)$, h) $log_{10}(N^2)$, i) median daily S_{red}^2. For plots e-i, dashed black line shows MLD, and measurement depths are indicated by tick marks inside the left axis. Vertical black lines indicate the two compositing regimes discussed in section 4.4.

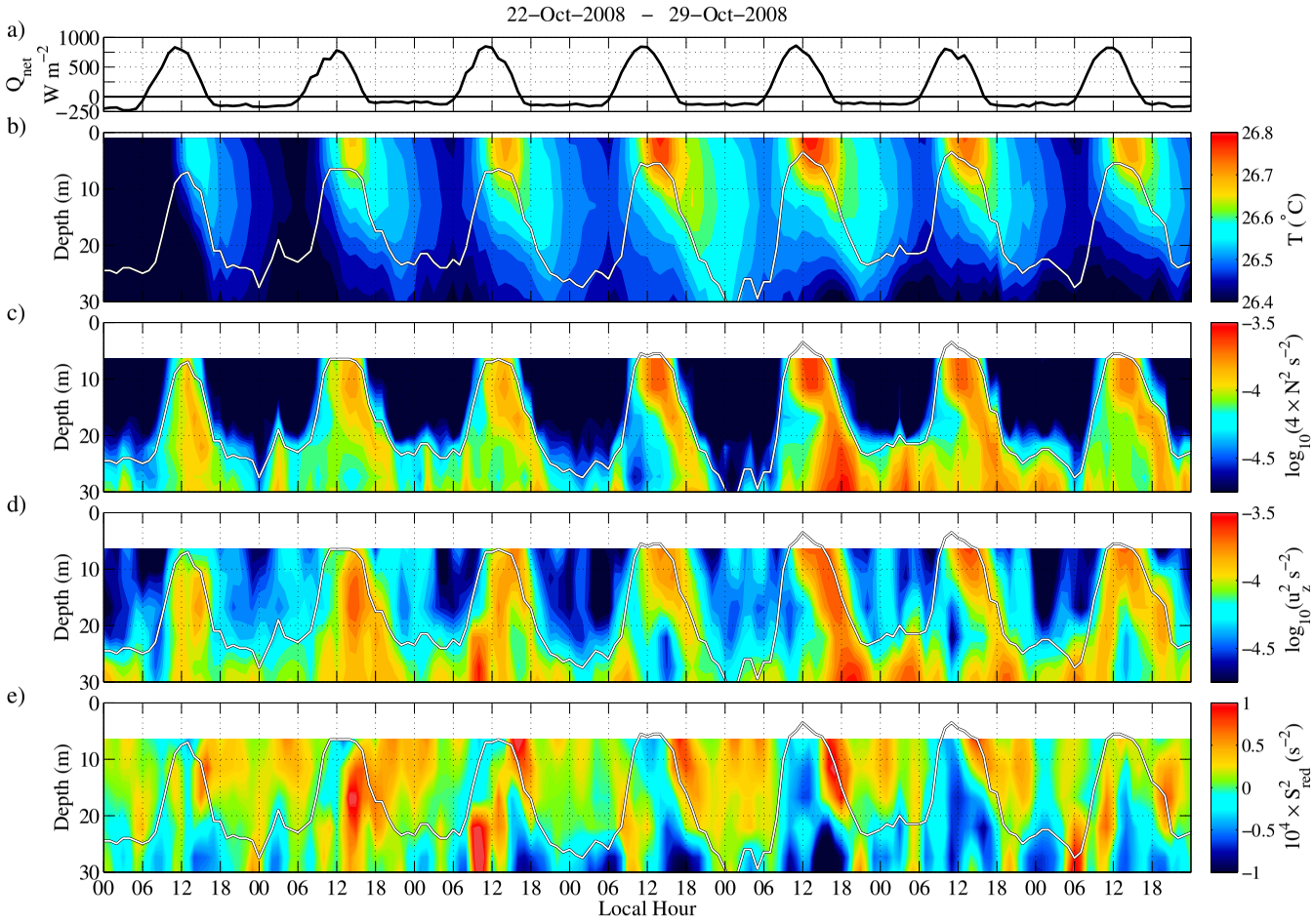

Figure 4.5: Sample hourly timeseries of the diurnal shear layer. a) Net surface heat flux, b) subsurface temperature, c) $log_{10}(4 \times N^2)$ multiplied to facilitate comparison with shear, d) $log_{10}(u_z^2)$, e) S^2_{red}. Plots d,e are smoothed with a 1-2-1 filter in time and depth to improve presentation clarity, solid line in b-e denotes the MLD.

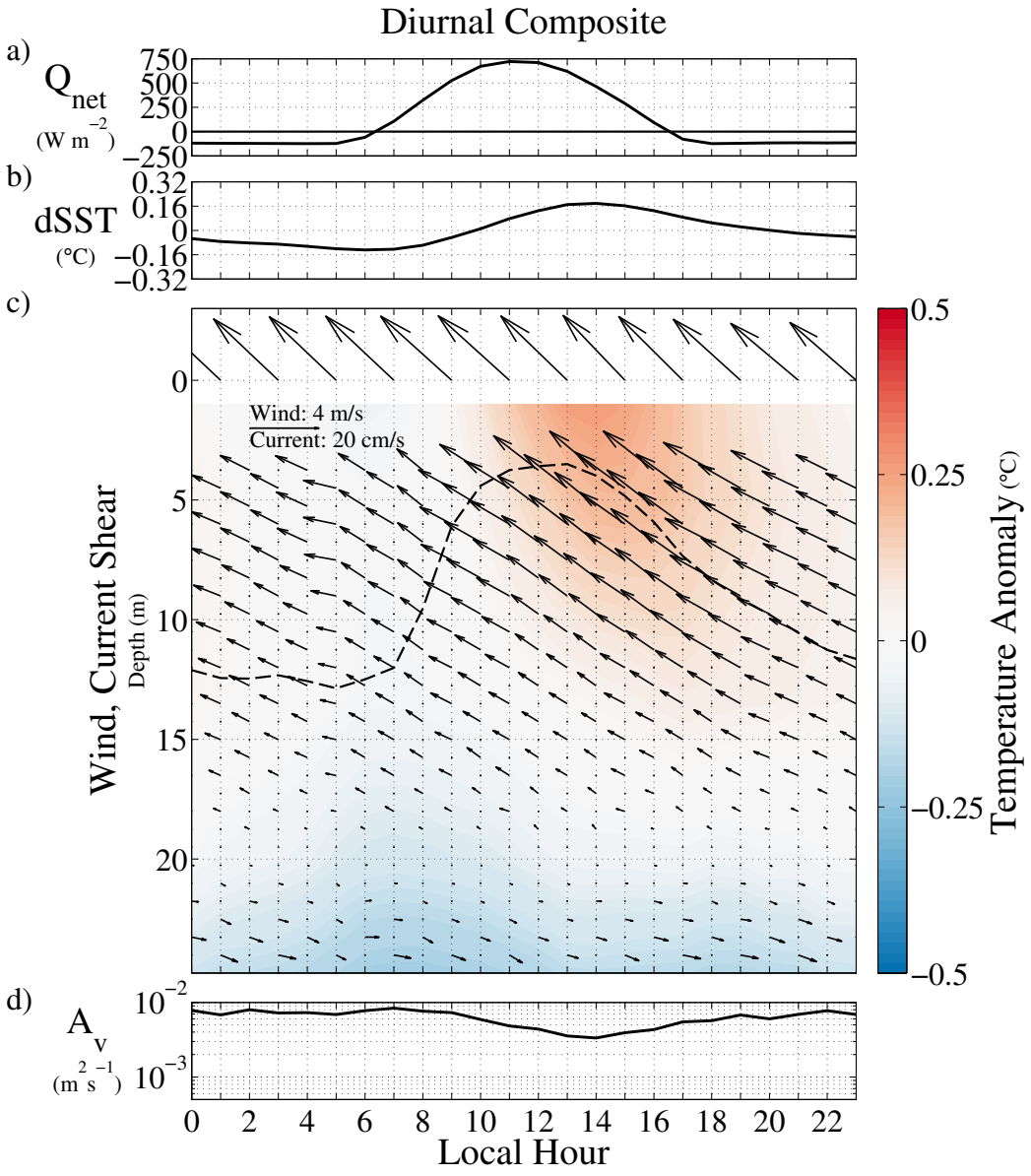

Figure 4.6: Composite diurnal cycle during steady trade wind conditions (section 4.4.1). a) net surface heat flux, b) SST anomaly, c) wind vectors plotted along the z=0 line, current vectors (relative to the 20 m currents) plotted at their observation depths (vectors are oriented with North up, and magnitude scale is shown in upper left), also plotted are the temperature anomaly (relative to the time-depth average, color scale), and MLD (dashed line), d) eddy viscosity, calculated as discussed in section 4.4.1.

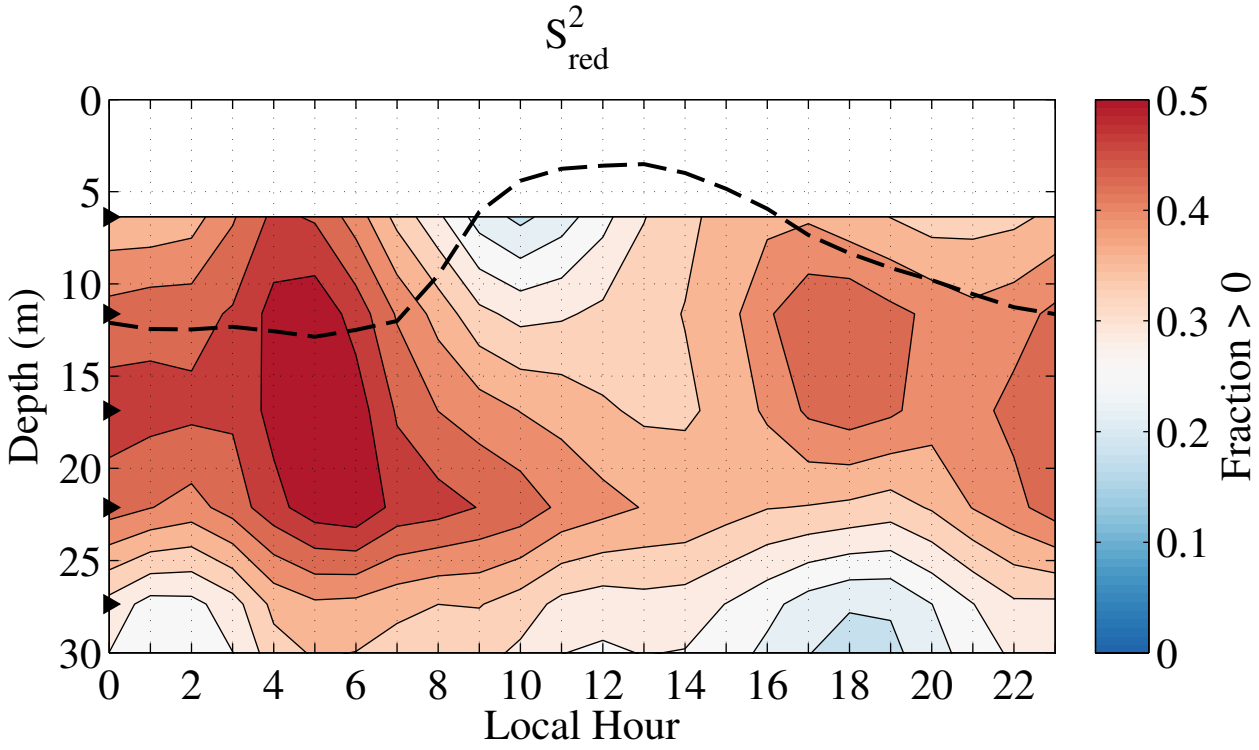

Figure 4.7: Fraction of diurnal composite observations during the steady trade wind conditions (section 4.4.1) for which $S^2_{red} > 0$, indicating flow unstable to shear instabilities. S^2_{red} bin center-points are indicated with black triangles on the ordinate, and average MLD is plotted with the dashed line. Bins are smoothed with a 1-2-1 filter in time and depth to improve presentation clarity.

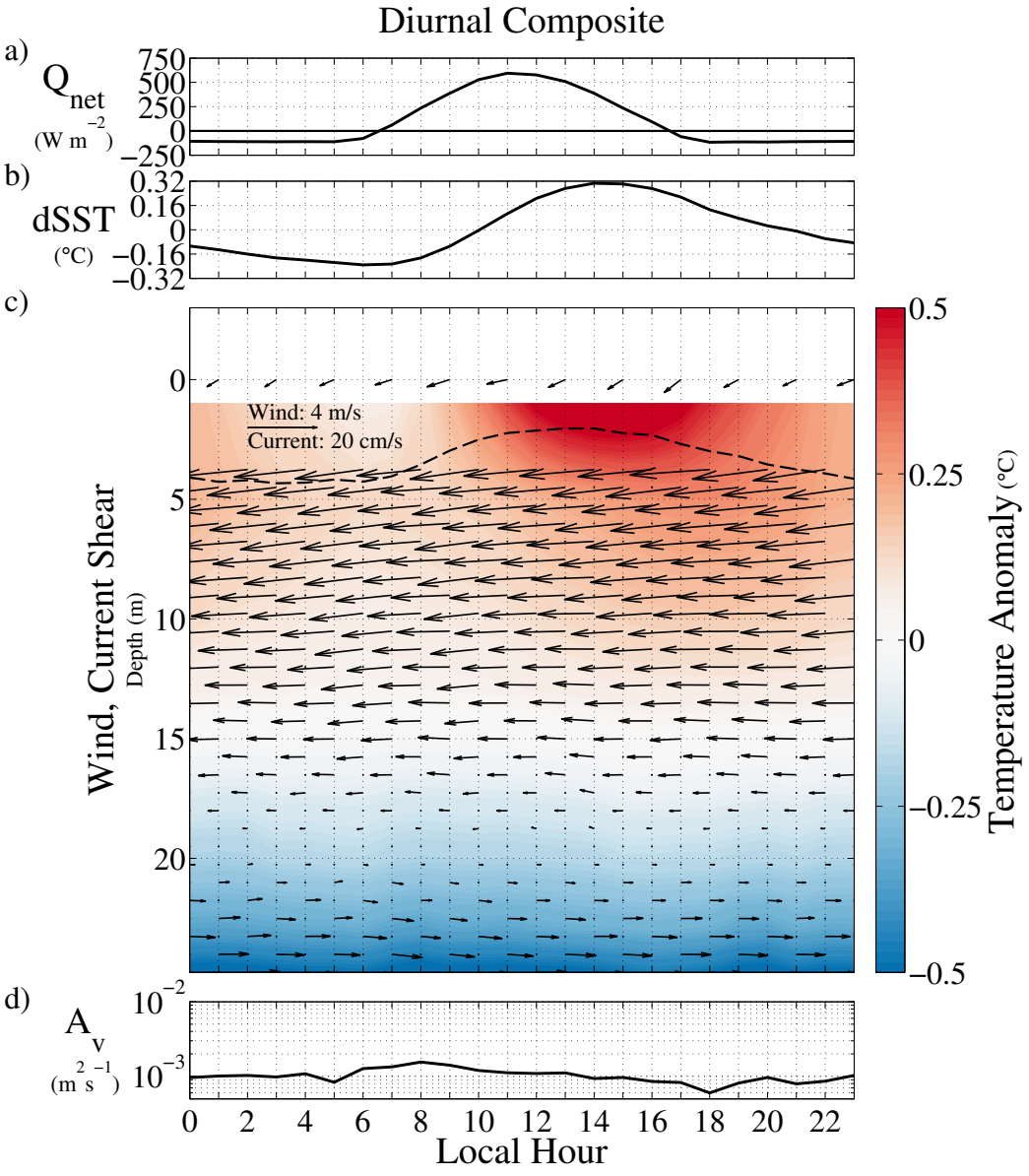

Figure 4.8: As in Figure 4.6, for the variable wind period (section 4.4.2).

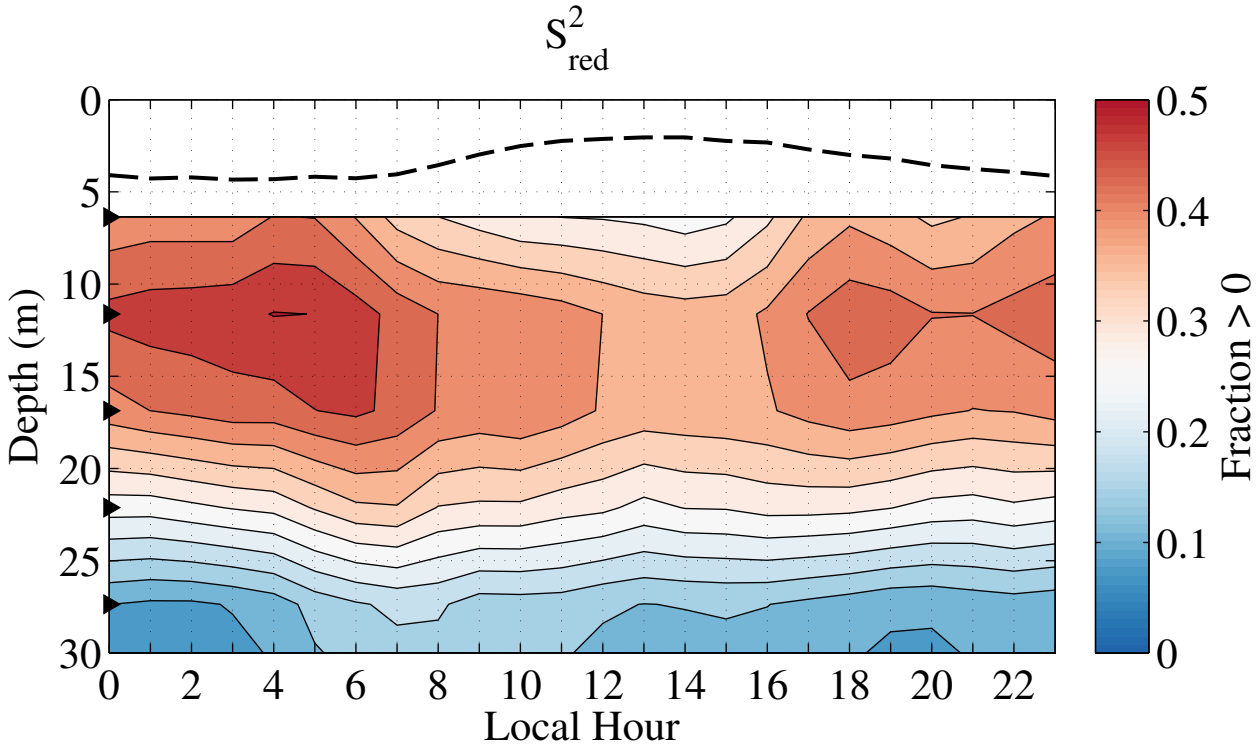

Figure 4.9: As in Figure 4.7, for the variable wind period (section 4.4.2).

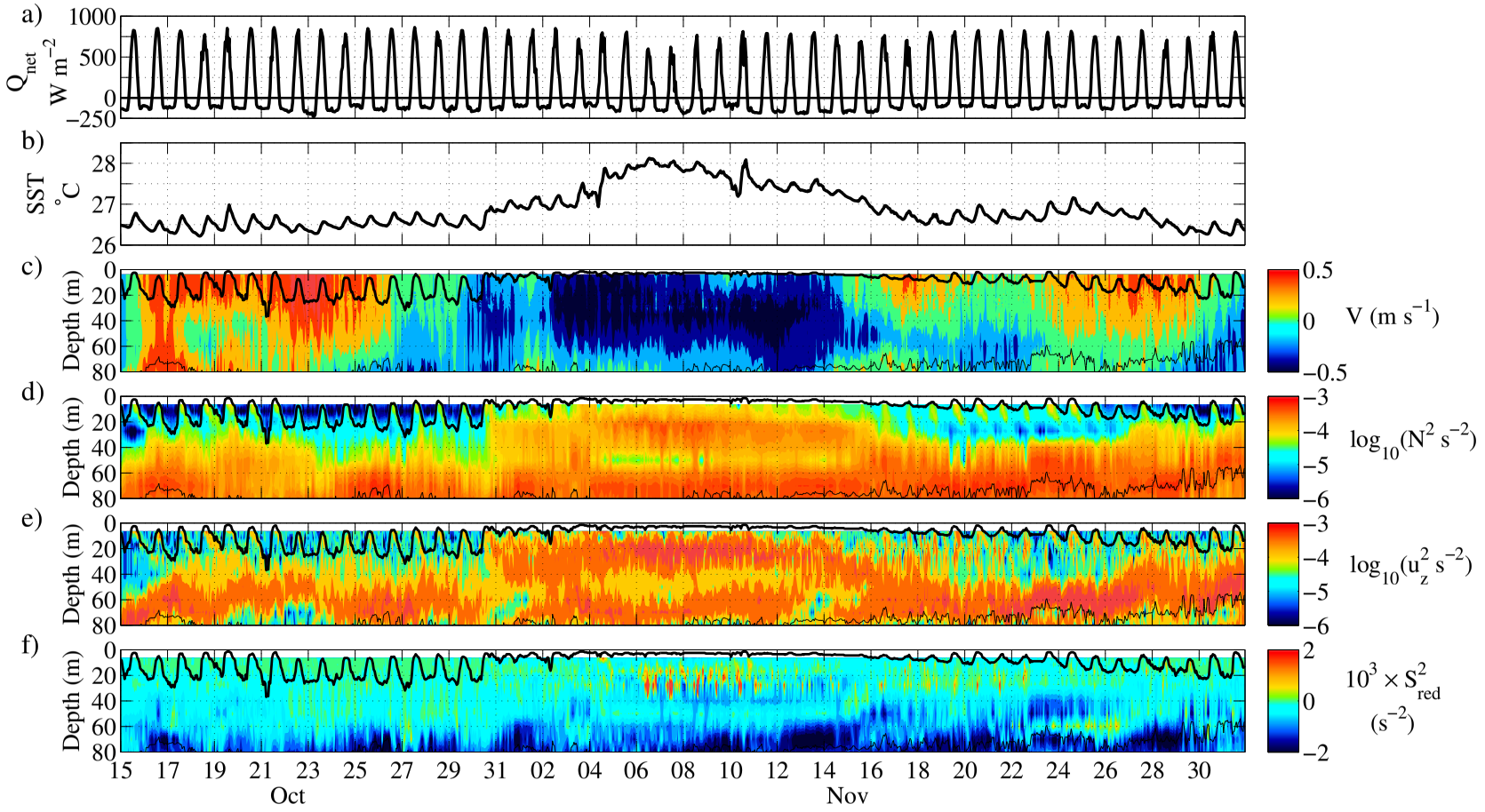

Figure 4.10: Overview of hourly observations during the passage of a TIW. a) Net surface heat flux, b) SST, c) meridional velocity, d) $log_{10}(N^2)$, e) $log_{10}(u_z^2)$, f) S^2_{red}. For plots c-f the MLD is shown in heavy black line, and the depth of the 1025 kg m^{-3} isopycnal is shown in light black line.

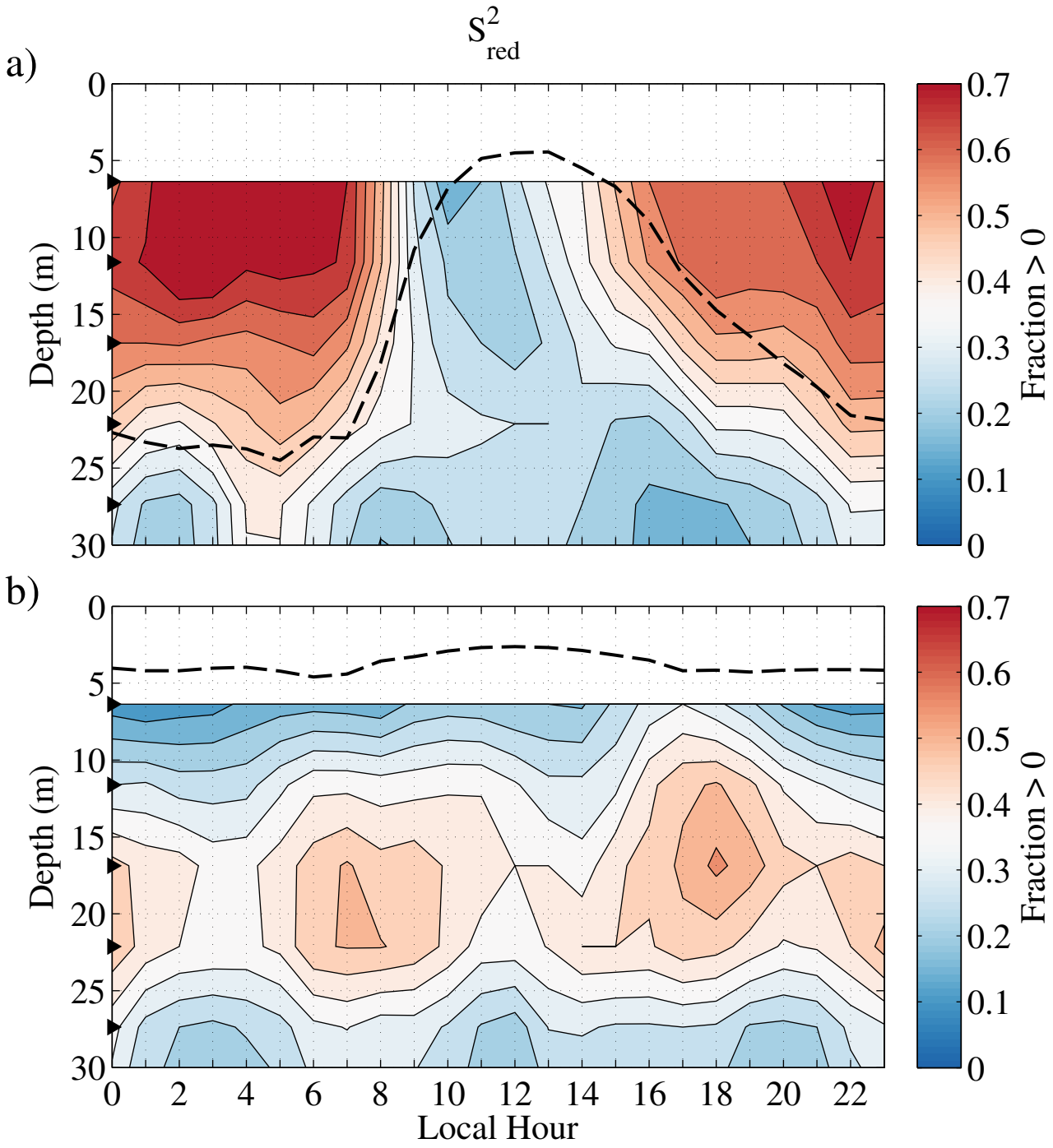

Figure 4.11: As in Figure 4.7, for a) TIW cold phase from 15 October through 30 October, b) TIW warm phase from 31 October through 15 November. Note modified colorscale relative to Figure 4.7.

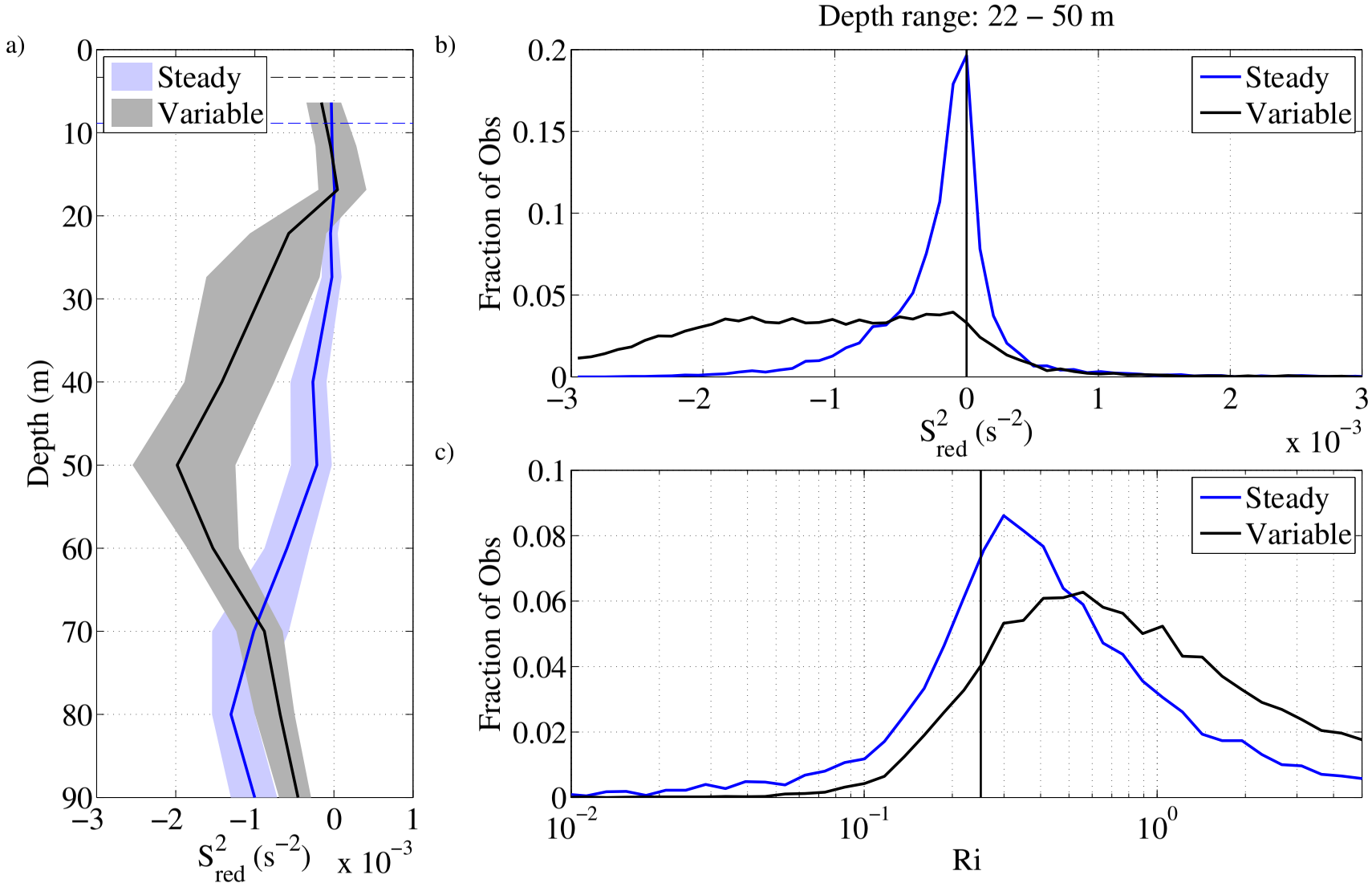

Figure 4.12: Marginal instability (MI) by time period. a) Median S^2_{red} (solid line) with interquartile range (shaded), b) distribution of S^2_{red} for observations between 22-50 m depth, c) as in b, but for Richardson number ($Ri = N^2 u_z^{-2}$). Dashed horizontal lines in (a) indicate the mean MLD, solid vertical lines in (b) and (c) indicate the critical value for stability.

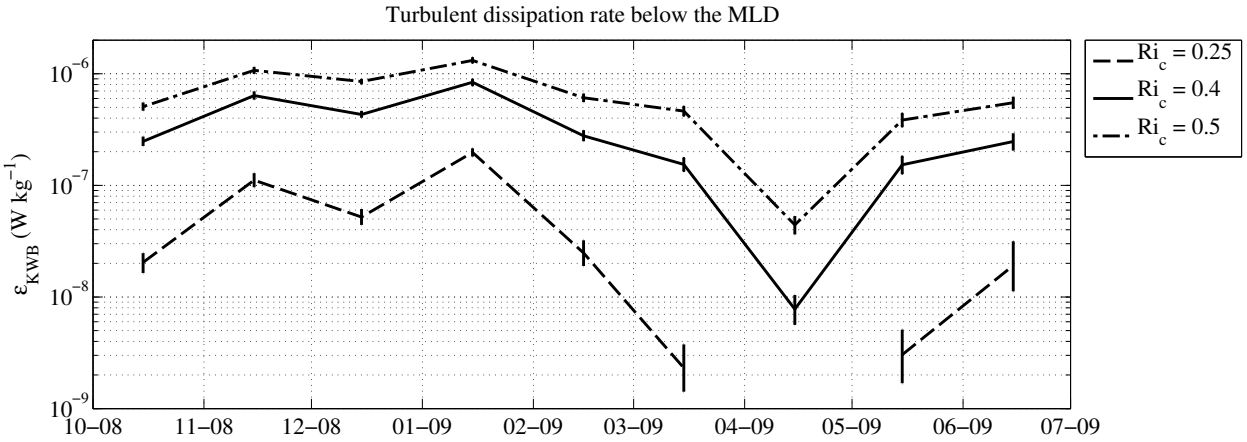

Figure 4.13: Monthly averaged (5% trimmed) turbulent dissipation rates, ϵ_{KWB} (W kg^{-1}), over the layer 20-50 m below the hourly MLD. Estimates are calculated for 3 different values of Ri_c as indicated in the legend. The trimmed mean for April ($Ri_c = 0.25$) equals 0 and is not plotted. This results from the definition of the Kunze et al. (1990) parameterization, which equals zero whenever the instability criteria are not met (Section 4.5). Vertical error bars indicate 95% confidence intervals on the trimmed mean, estimated using the bootstrap method.

Chapter 5

SIMPLE MODELS OF WIND-DRIVEN OCEAN CURRENTS WITH TIME-VARYING VISCOSITY: FROM SPIN-UP TO RECTIFICATION

The effects of time-varying turbulent viscosity on horizontal currents in the ocean surface boundary layer are considered using two simple analytic models of the time-dependent Ekman layer. First, the time-dependent transfer function for wind-forced velocity is derived, demonstrating how monochromatic variability in eddy viscosity leads to modification of the vertical structure of velocity across all frequency bands. A dependence in the transfer function on the phase of the time-varying eddy viscosity, relative to the surface wind stress, is illustrated physically by the early response of a motionless ocean to an impulsively started wind stress. Next, a simple periodic model, which allows both vertical and temporal variability in eddy viscosity, is formulated. This analytic model is shown to reproduce major aspects of the near-surface ocean diurnal cycle in velocity and shear, while retaining direct parallels to the steady-state Ekman solution, providing a useful conceptual tool. The parameter dependence of this model is explored qualitatively, and quantitative measures of the low-frequency rectification of velocity and shear are derived. Results demonstrate that time-variability in eddy viscosity leads to significant changes to the time-averaged velocity and shear fields, with important implications for the interpretation of observations. These findings mirror those of more complex numerical modeling studies, suggesting that some of the rectification mechanisms active in those studies may not require feedbacks between near-surface shear and viscosity, which are absent in the analytic models considered here.

5.1 Introduction

The daily transit of the sun causes a daily cycle in surface heat flux that is a principal forcing of upper ocean variability. This diurnal cycle in surface heat flux initiates a diurnal cycle in temperature, stratification, and near-surface mixing (Smyth, 1854; Stommel et al., 1969; Brainerd and Gregg, 1993). The effects of these changes have been the subject of widespread study, both from the oceanographic perspective, where, beyond the purely physical implications, a host of bio-physical interactions on the diurnal scale have been identified (McCreary et al., 2001; Kawai and Wada, 2007), and from the atmospheric perspective, where diurnal sea-surface temperature variability is critical to boundary layer moisture content and convection, which respond non-linearly to temperature (Chen and Houze, 1997; Clayson and Chen, 2002; Dai and Trenberth, 2004). The ability of the diurnal cycle in surface heat flux to modify low-frequency ocean temperature variability, a process termed rectification, has also been widely studied in the context of models, where it is shown that diurnal variability modifies the mean state on intraseasonal and longer timescales (Shinoda, 2005; Danabasoglu et al., 2006; Bernie et al., 2007, 2008).

While the thermodynamic response has been the subject of much work, the dynamic response remains less well understood. Observations have established that diurnal variability in stratification can serve to inhibit turbulent vertical momentum flux, causing the near-surface convergence of wind-driven momentum, and leading to the creation of a downwind diurnal jet (Price et al., 1986). These jets are highly sheared, lowering the flow Richardson number, allowing the development of shear instabilities that deepen the mixed layer before the surface heat flux has changed sign, suggesting the dynamics of the ocean response are intertwined with the thermodynamic response (Cronin and Kessler, 2009; Smyth et al., 2013; Wenegrat and McPhaden, 2015a). Diurnal variability of mixing has also been implicated in departures of time-averaged velocity fields from the predictions of classic Ekman theory (Price and Sundermeyer, 1999), although the observational evidence alone has not been conclusive in this regards (Lewis and Belcher, 2004; Rascle and Ardhuin, 2009).

Much of the theoretical work on the dynamics of the ocean diurnal cycle has focused on the use of slab layer models, which while useful in their simplicity, by construction do not offer any insight into the vertical structure of the flow. Further, observations suggest that Ekman theory provides a more consistent description of low-frequency variability than slab layer models do (Davis et al., 1981; Weller and Plueddemann, 1996; Kim et al., 2014), and hence utilizing slab layer physics to understand rectification effects may not be appropriate. Thus, despite the recognized importance of the diurnal cycle, questions remain about the dynamical response, in particular regarding the possible routes to dynamical rectification.

Important work on this topic was undertaken by McWilliams and Huckle (2006), and McWilliams et al. (2009), in the context of idealized numerical models. In these works, transient winds, surface buoyancy fluxes, and interior eddy fluxes were all shown to result in rectification to the time-mean flow, attributed principally to modifications of the turbulent boundary layer depth and nonlinearities in the parameterized eddy viscosity (McWilliams and Huckle, 2006; McWilliams et al., 2009). These findings are significant contributions to our understanding of dynamical rectification effects, particularly in their ability to elucidate the terms controlling changes in turbulent mixing under different forcing regimes. However, as is often the case, the greater physical realism enabled by the numerical model comes at the expense of additional complexity, and thus the parameter dependence and underlying physics are not as clearly illuminated as with theoretical approaches.

Here we take a simpler approach, situated in complexity between analytic slab layer models and more realistic numerical models, and consider two models of the time-dependent Ekman layer. In both cases the eddy viscosity is allowed to vary in time, approximating the known time-variability of mixing by making an ad hoc assumption that it can be separated from the wind-driven shear without feedbacks. This is at best a crude first-order approximation (cf. McWilliams et al., 2009), however the ability of the resulting models to reproduce major aspects of the diurnal cycle in the near-surface ocean, as well their analytic tractability and possibility for insight into the underlying physical processes suggest it is a worthwhile exercise. In this respect, aspects of this work are similar to approaches used extensively in

the study of the dynamics of low-level jets in the atmospheric boundary layer (Buajitti and Blackadar, 1957; Singh et al., 1993; Tan and Farahani, 1998; Zhang and Tan, 2002), which to our knowledge have not yet been applied to the oceanographic problem.

We begin in section 5.2 with consideration of the response of an ocean with time-varying eddy viscosity to an impulsively started wind-stress. This model is used to examine the initial formation process of near-surface currents. Results from this section suggest that a time-periodic model is reasonable for the case of steady wind stress, and in section 5.3 we formulate an analytic model of a time-periodic Ekman layer with periodically varying turbulent viscosity. This model allows for a simple expository discussion of the parameter dependence, and the expected low-frequency rectification effects of time-dependent mixing (section 5.4).

5.2 Time-Dependent Ekman Formulation

We consider a linearized model of time-dependent horizontal flow, written using complex notation as $\vec{u} = u + iv$. The horizontal momentum equations are thus given by,

$$\vec{u}_t + if\vec{u} = -\frac{1}{\rho}\nabla p + (A_v(z,t)\vec{u}_z)_z, \tag{5.1}$$

with subscript t, and z, denoting differentiation with respect to time and the vertical coordinate, respectively. It is assumed that the horizontal pressure gradient, ∇p, is independent of z, allowing separation into geostrophic and ageostrophic components. The focus of this work is on the wind-driven flow, hence for the remainder we set $\nabla p = 0$, although we caution that baroclinic pressure gradients can be expected to significantly modify ageostrophic flows in the real ocean (Wenegrat and McPhaden, 2015b). For simplicity we also begin with an assumption that the turbulent eddy viscosity, A_v, is vertically constant. This assumption will be removed in section 5.3. We thus seek a solution to,

$$\vec{u}_t + if\vec{u} = A_v(t)\vec{u}_{zz}. \tag{5.2}$$

Transforming $\vec{u} = e^{-ift}\vec{w}$ reduces (5.2) to the one-dimensional heat equation with a time-varying coefficient,

$$\vec{w}_t = A_v(t)\vec{w}_{zz}. \tag{5.3}$$

This equation arises in the study of a wide-range of physical phenomenon, including non-Newtonian fluids where the viscosity is a function of the shear-stress (Lister and Stone, 1996), diffusion in porous materials such as concrete (Mangat and Molloy, 1994), and heat conduction in radioactive materials (Cannon, 1984). For arbitrary $A_v(t)$ it is possible to find a unique transformation of the time coordinate such that (cf. Cannon, 1984, 13.1.1-13.1.8),

$$\vec{w}_\zeta = \vec{w}_{zz}, \tag{5.4}$$

where

$$\zeta(t) = \int_0^t A_v(T)\,\mathrm{d}T. \tag{5.5}$$

Here we are interested in solutions corresponding to an impulsively started wind stress, with no initial velocity distribution $\vec{u}(z,0) = 0$. The boundary conditions are given by,

$$\vec{u_z}(0,t) = \frac{\vec{\tau}(t)}{\rho A_v(t)}, \tag{5.6}$$

$$\vec{u} \to 0, \quad z \to -\infty, \tag{5.7}$$

which are the standard boundary conditions on the Ekman problem. The solution to (5.2) is thus,

$$\vec{u} = \int_0^t \frac{e^{-if(t-\eta)}}{\sqrt{\pi Q(\eta)}} e^{-\frac{z^2}{4Q(\eta)}} \frac{\vec{\tau}(\eta)}{\rho}\,\mathrm{d}\eta, \tag{5.8}$$

$$Q(y) = \int_{t-y}^t A_v(T)\,\mathrm{d}T. \tag{5.9}$$

This solution was considered briefly by Csanady and Shaw (1980), in regards to a constant wind-stress and an exponentially asymptotic $A_v(t)$, and we expand upon that work here.

An intuitive way to write (5.8) is as a convolution between a transfer function and the time-dependent wind stress,

$$\vec{u} = h(t) * \frac{\vec{\tau}(t)}{\rho}, \tag{5.10}$$

where

$$h(t) = Y(t)\frac{e^{-ift}}{\sqrt{\pi Q(t)}}e^{-\frac{z^2}{4Q(t)}}, \tag{5.11}$$

and $Y(t)$ is the Heaviside step-function. Equation (5.11) thus represents the surface currents generated in response to an impulsive wind-forcing, a combination of decaying inertial oscillations, and diffusive momentum transfer over a time-dependent depth scale of $2\sqrt{Q(t)}$ (Lewis and Belcher, 2004). In the case that A_v is constant in time, this reduces to the Fredholm solution given by Ekman (1905), and considered further by Gonella (1971, 1972),

$$\hat{h}(t) = Y(t)\frac{e^{-ift}}{\sqrt{\pi A_v t}}e^{-\frac{z^2}{4A_v t}}. \tag{5.12}$$

While the solution (5.8) is fully general in regards to the time-dependence of A_v, we are particularly interested in the role of time-periodic A_v. This is motivated by observations of the diurnal cycle of the upper ocean, where an increase in afternoon thermal stratification modulates mixing (Brainerd and Gregg, 1993; Bond and McPhaden, 1995; Smyth et al., 2013; Wenegrat et al., 2014), and leads to the acceleration of a sheared diurnal jet (Price et al., 1986; Cronin and Kessler, 2009). This diurnal jet has been shown to play an important role in modulating air-sea interaction, as it can lead to shear-instability mixing of the near-surface layer, limiting diurnal sea surface temperature anomalies (Wenegrat and McPhaden, 2015a), thus coupling the dynamic and thermodynamic response.

Our focus for the remainder of this section is thus on eddy viscosities of the form,

$$A_v(t) = A_{v0}(1 + \delta cos(\omega t + \psi)), \tag{5.13}$$

where A_{v0} is the time-mean eddy viscosity, $\delta \in [0, 1)$, $\omega = \frac{2\pi}{1\,day}$, and ψ is the phase of A_v relative to the onset of the wind forcing.

Insight into the dynamics of (5.11) can be had by examining the transfer function in the spectral domain. The Fourier transformed (5.11), which we denote $H(\sigma)$, gives the ocean velocity response to rotary wind stress at each frequency, with positive (negative) frequencies representing anti-clockwise (clockwise) rotation (Gonella, 1972). The amplitude of the theoretical response function is infinite at $\sigma = -f$, the resonant inertial frequency (figure 5.1), and decays rapidly outside the inertial band. The phase of the transfer function, relative to the rotating surface wind stress gives information about the vertical structure of the forced currents, as shown in figure 5.2, with a frequency dependent Ekman depth defined as $h_{Ek}(\sigma) = \sqrt{|2A_{v0}/(f + \sigma)|}$. In the constant A_v solution surface phase is always $\pm 45°$, with a 90° phase shift across the negative inertial frequency, representing the lead-lag relationship of the currents to the rotating wind stress (Gonella, 1972; Elipot and Gille, 2009).

Notably, although the time dependence in A_v considered here, as given by (5.13), does not change the time-mean value, it introduces a complex modulation of the Ekman transfer function across all frequencies bands, including as $\sigma \to 0$. Particularly significant changes in vertical structure are also evident at the frequencies $\sigma = -(f \pm \omega)$. The sensitivity at these frequencies can be best understood in a frame of reference following the rotating surface wind stress vector. In this frame, the wind stress remains constant in direction, and inertial oscillations will appear to be rotating at frequency $\sigma_{Eff} = \mp|\omega|$. The time-varying A_v is thus phase-locked with the apparent inertial oscillation, introducing significant modifications to the vertical structure of the currents, as well as small variations in amplitude (figure 5.1). At the diurnally resonant latitudes 30°, where $f = \pm\omega$, this modulation will occur for a steady-wind stress forcing, suggesting the low-frequency vertical structure of currents at these latitudes may be particularly sensitive to diurnal variations in mixing. This mechanism is distinct from the resonance of local inertial oscillations with diurnally varying winds. Similar effects might also be expected at other latitudes due to physical processes, such as baroclinic tides or inertial shear, which modulate near-surface mixing at different frequencies. This

finding, and the nonlinear dependence of (5.8) on (5.9), suggests that time-variability in A_v will give rise to a low-frequency rectification, the focus of section 5.4.3 below.

The sensitivity to the phase of A_v in the transfer function can be best understood by examining the early formation of an Ekman layer in response to an impulsively started steady wind stress (figure 5.3). This process can be divided conceptually into three regions (Pollard et al., 1973; Lewis and Belcher, 2004). The first region falls between the depth scale of diffusive momentum penetration (red line, $z_{Diff}(t) = -\sqrt{4Q(t)}$), and the arrest of the flow by rotation (solid black line, $z_{Rot}(t) = -fth_{Ek}$). In this region the flow is accelerated by the turbulent momentum flux convergence, which is sensitive to the early values of $A_v(t)$. Later, for $z > z_{Rot}$ and $t < 2f^{-1}$ the flow begins to be turned by Coriolis. When $t > 2f^{-1}$ the solution consists of a surface Ekman layer and decaying inertial oscillations. An alternate definition of the Ekman depth thus arises as simply the depth scale of diffusive penetration before arrest by rotation at half a pendulum day, $h_{Ek} = z_{Diff}(2f^{-1})$, hence, $h_{Ek} = \int_0^{2/f} A_v(T)dT$, which is sensitive to the initial values of A_v .

The characteristics of the initial surface velocity response to rotary wind forcing at different frequencies can be seen in figure 5.4, where orange lines indicate the standard time-dependent Ekman solution (Gonella, 1972), $\delta = 0$, and blue lines indicate $\delta = 0.8$. The modulation at $\sigma = -(f + \omega)$, as discussed above, is evident, as is the inertial resonance which is not affected by the time varying A_v. At $\sigma = -\omega$ there is evident hysteresis, with the time-mean currents dependent on the early spin-up trajectory. For steady-state forcing the initial spin-up is as discussed in regards to figure 5.3, with the phase dependence disappearing on the timescale of the initial transients, $t \sim f^{-1}$. Of particular interest is the oscillatory steady-state response to the steady-wind forcing, which alters the time-mean flow, hence rectifying the diurnal cycle of mixing to the steady-state solution. We can take advantage of the oscillatory nature of the response, along with the independence from the initial phase during spin-up, to seek periodic solutions for the case of steady-wind forcing which further clarify these dynamics.

5.3 Time-Periodic, Steady Forcing

As in section 5.2, the linearized wind-driven component of the flow will satisfy,

$$\vec{u}_t + if\vec{u} = (A_v(z,t)\vec{u}_z)_z, \tag{5.14}$$

considered here subject to the following conditions,

$$\vec{u}(z,t) = \vec{u}(z, t + \frac{2\pi}{\omega}), \tag{5.15a}$$

$$\vec{u}_z(0,t) = \frac{\vec{\tau}_w}{\rho A_v(0,t)}, \tag{5.15b}$$

$$\vec{u} \to 0, \quad z \to -\infty. \tag{5.15c}$$

Equation (5.15a) expresses the periodic-time boundary condition, with frequency ω. As above, we will identify this with the diurnal cycle, although the solution is valid generally for any ω. The surface boundary condition, (5.15b), is the standard shear-stress boundary condition, as used in (5.6), however here the wind stress is assumed constant in time, and the eddy viscosity is allowed to be a function of both time and space, $A_v(z,t)$. The results of this section are not sensitive to the particular bottom boundary condition, hence for simplicity we use, (5.15c), the standard Ekman bottom boundary condition. The derivation given can easily be applied to alternate boundary conditions.

$A_v(z,t)$ is assumed to be a known parameter, and we require that it be separable in time and space, $A_v(z,t) = A(z)K(t)$. The dimensional vertical structure, $A(z)$, can take any form that satisfies the requirements of a Wentzel-Kramers-Brillouin-Jeffreys approximation (WKBJ, Bender and Orszag, 1978), discussed below. However, we require that the time dependence take a particular form (Buajitti and Blackadar, 1957),

$$K(t) = 1 + \delta cos(\omega t), \tag{5.16}$$

with $\delta \in [0, 1)$, determining the strength of the periodic cycle of mixing. These mathemati-

cally expedient requirements on A_v are not expected to accurately reflect the diurnal cycle of near-surface mixing, which remains an active area of observational work. Notably, parameterizations based on similarity theory with time varying boundary layer depth, such as the K-Profile Parameterization (Large et al., 1994), result in A_v where space-time dependence is not separable. However, the idealized form of A_v we use here can be justified in part based on observations of the diurnal cycle of near-surface A_v which suggests that a sinusoidal time dependence is a reasonable first approximation (Wenegrat and McPhaden, 2015a). An example composite diurnal cycle, estimated indirectly from ~ 3 months of moored observations following the method given in Wenegrat et al. (2014), is shown in figure 5.5, demonstrating the essentially sinusoidal time-dependence. Further support for this idealized time-dependence of A_v comes from a posteriori comparisons of the theory with more complete numerical models (section 5.4.1, and Appendix A). Note also that the periodic time-variability in (5.16) introduces no change to the diurnally averaged A_v, which simplifies comparison to the steady ($\delta = 0$) solution.

Similar to the approach taken in section 5.2, we define $\vec{w}(z,t) = e^{ift}\vec{u}(z,t)$, and rewrite equation (5.14) as,

$$\vec{w}_t(z,t) = [A(z)K(t)\vec{w}(z,t)_z]_z \tag{5.17}$$

Transforming the time coordinate, such that $\zeta = t + \delta/\omega sin(\omega t)$, gives,

$$\vec{w}_\zeta = [A(z)\vec{w}_z]_z \tag{5.18}$$

In the new coordinate system the periodic boundary condition can be written as, $\vec{w}(z,\zeta + \frac{2\pi}{\omega}) = \vec{w}(z,\zeta)e^{if\frac{2\pi}{\omega}}$ (Zhang and Tan, 2002), which is true of,

$$\vec{w}(z,\zeta) = w_0 \sum_{n=-\infty}^{\infty} \vec{w}_n(z)e^{i(f+n\omega)\zeta}. \tag{5.19}$$

Substituting Eq. 5.19 into equation 5.18 gives a series of ordinary differential equations,

$$[A(z)(\vec{w}_n)_z]_z - i(f + n\omega)\vec{w}_n = 0. \tag{5.20}$$

Each of the n-equations defined by Eq. 5.20 can be approximated using the WKBJ method (Grisogono, 1995), which assumes,

$$w_n \propto e^{\frac{1}{\epsilon}\left(S_0+\epsilon S_1+\epsilon^2 S_{2\ldots}\right)}. \tag{5.21}$$

Non-dimensionalizing gives,

$$Ek_n\left[\hat{A}(z)(\hat{w}_n)_{\hat{z}\hat{z}} + \hat{A}(v)_{\hat{z}}\hat{w}_{\hat{z}}\right] - i\hat{w} = 0, \tag{5.22}$$

where the hat notation indicates non-dimensional quantities, $Ek_n = \frac{A_0}{(f+n\omega)D^2}$, and A_0 is a representative scale value of A_v. We identify D with the depth scale over which $A(z)$ varies, as per the discussion in Wenegrat and McPhaden (2015b). Ek_n thus characterizes the ratio of the depth scale of the n^{th} mode boundary layer to the depth scale over which $A(z)$ varies. Using (5.21) in (5.22) gives $\epsilon \sim Ek_n^{\frac{1}{2}}$, and the WKBJ balance equations,

$$S_0 = \sqrt{i}\int_z^0 \hat{A}(Z)^{-\frac{1}{2}}\,\mathrm{d}Z, \tag{5.23}$$

$$S_1 = -\frac{1}{4}\log\hat{A}(z). \tag{5.24}$$

Use of the WKBJ approximation requires that,

$$\frac{Ek_n^{\frac{1}{2}}S_1}{S_0} \ll 1, \qquad Ek_n^{\frac{1}{2}} \to 0, \tag{5.25}$$

$$Ek_n^{\frac{1}{2}}S_2 \ll 1, \qquad Ek_n^{\frac{1}{2}} \to 0, \tag{5.26}$$

which physically can be understood as requiring slow variation of A_v relative to the boundary

layer thickness of the n^{th} mode. The constraint this places on the validity of the WKBJ approximation will be strongest for the $n = 0$ mode, as higher modes become rapidly surface trapped. We also require that $A(z) > 0$, so as to not violate (5.25), although this restriction can be removed by patching an appropriate inner solution as in Wenegrat and McPhaden (2015b). A specific case where this WKBJ expansion is formally incorrect is the case of $f = \pm n\omega$, where mode $\mp n$ will have $Ek_n \to \infty$. However, these modes are zeros of the Bessel functions used in the solutions below, so do not contribute to the total solution.

The solution for an arbitrary mode after application of the bottom boundary condition is thus,

$$w_n(z) = C_n A(z)^{-\frac{1}{4}} e^{-\sqrt{2i}\int_z^0 h_{nEk}^{-1}(Z)\,\mathrm{d}Z}, \tag{5.27}$$

such that h_{nEk} defines the mode's depth dependent Ekman depth, $h_{nEk}(z) = \sqrt{2A(z)/(f + n\omega)}$.

The upper BC can be considered by returning to the series expansion Eq. (5.19), in terms of $w_z(z, \zeta)$.

$$\sum_{n=-\infty}^{\infty} C_n \sqrt{2i}\chi_n(0) h_{nEk}^{-1}(0) A(0)^{-\frac{1}{4}} e^{[i(f+n\omega)\zeta]} = \frac{e^{ift(\zeta)}}{A(0)K(t(\zeta))}, \tag{5.28}$$

where we have set $w_0 = \frac{\tau_w}{\rho}$, and,

$$\chi_n(z) = 1 - \frac{\sqrt{-2i}}{8}\frac{A(z)_z}{A(z)} h_{nEk}(z). \tag{5.29}$$

Transforming back to the original time coordinate,

$$\sum_{n=-\infty}^{\infty} C_n \sqrt{2i}\chi_n(0) h_{nEk}^{-1}(0) A(0)^{-\frac{1}{4}} e^{i(f+n\omega)t + i\delta(\frac{f}{\omega}+n)sin(\omega t)} = \frac{e^{ift}}{A(0)K(t)}. \tag{5.30}$$

Writing $K(t)$ as $K(t) = 1 + \delta/2(e^{i\omega t} + e^{-i\omega t})$, and dividing through by the right-hand side

gives,

$$\sum_{n=-\infty}^{\infty} C_n\sqrt{2i}\chi_n(0)h_{nEk}^{-1}(0)A(0)^{\frac{3}{4}} \left[e^{in\omega t+i\delta(\frac{f}{\omega}+n)sin(\omega t)}+\frac{\delta}{2}e^{i(n+1)\omega t+i\delta(\frac{f}{\omega}+n)sin(\omega t)}+\frac{\delta}{2}e^{i(n-1)\omega t+i\delta(\frac{f}{\omega}+n)sin(\omega t)}\right]=1 \quad (5.31)$$

Note that if integrated in time each of the exponential terms takes the form of a Bessel function of the first kind (Temme, 1996; Zhang and Tan, 2002), thus,

$$\sum_{n=-\infty}^{\infty} (-1)^n C_n\sqrt{2i}\chi_n(0)h_{nEk}^{-1}(0)A(0)^{\frac{3}{4}} \left[J_n(\delta(\frac{f}{\omega}+n))-\frac{\delta}{2}J_{n+1}(\delta(\frac{f}{\omega}+n))-\frac{\delta}{2}J_{n-1}(\delta(\frac{f}{\omega}+n))\right]=1. \quad (5.32)$$

Such that the surface boundary condition is satisfied if,

$$C_n=(-1)^n\frac{\sqrt{-2i}J_n(\delta(\frac{f}{\omega}+n))h_{nEk}(0)}{2\chi_n(0)A(0)^{\frac{3}{4}}}. \quad (5.33)$$

For simplicity in presentation we assume that A does not vary significantly at $z=0$ relative to the mode Ekman depth, ie. $\chi_n(0)\sim 1$, although we retain this factor in subsequent calculations.

The full approximate solution is thus given by,

$$\vec{u}(z,t)=\frac{\vec{\tau}_w}{\rho\sqrt{fA(0)}}e^{-i\frac{\pi}{4}}\sum_{n=-\infty}^{\infty}\left[(-1)^n\underbrace{\frac{\sqrt{f}}{\sqrt{f+n\omega}}J_n(\gamma_n)}_{\text{I}}\underbrace{\Omega_n(z)}_{\text{II}}\underbrace{e^{i(n\omega t+\gamma_n sin(\omega t))}}_{\text{III}}\right], \quad (5.34a)$$

where

$$\Omega_n(z) = \left(\frac{A(0)}{A(z)}\right)^{\frac{1}{4}} e^{-(1+i)\int_z^0 h_{nEk}^{-1}(Z)\,\mathrm{d}Z}, \tag{5.34b}$$

$$\gamma_n = \delta(\frac{f}{\omega} + n), \tag{5.34c}$$

and where J_n is the n^{th} Bessel function of the first kind (Temme, 1996).

The term outside the summation defines the standard Ekman velocity scale, as arises in the steady-state problem. This amplitude term then multiplies an infinite series of oscillating vertical modes, with vertical structure determined by the boundary layer ordinary differential equation (5.20). Term II (eq. 5.34b) defines the vertical structure of each individual mode, each of which is a solution to a steady-state Ekman problem with a modified rotational frequency of $f + n\omega$. Thus, higher modes are progressively more surface trapped, with boundary layer depth scale h_{nEk}. The extent of the vertical trapping of higher modes can be noted by considering that for the diurnal period considered here, mode $n = 2$ has a vertical depth scale less than that of a traditional Ekman layer at latitude 90°. It follows from this that, in the time-periodic problem, oscillating A_v leads to a shoaling of the mean flow relative to the constant A_v solution.

By construction the vertical derivative of the full summation in (5.34a) will always equal unity for $z = 0$. However for a given value of δ some modes will be excited more than others. Term I of (5.34a) thus can be considered as determining how efficiently the wind stress projects onto each mode, with higher values of δ leading to more significant excitation of higher modes (figure 5.6), with rapid roll-off for increasing n. The ratio f/ω in γ determines the symmetry of modes that are excited, with $f/\omega \to 0$ leading to a symmetric excitation of positive and negative modes, whereas larger values of f/ω are skewed towards positive modes (figure 5.6). For $\delta = 0$, $J_0(0) = 1$, such that only the zeroth Bessel function is excited, and the steady state Ekman solution is recovered.

The time-dependence in (5.34a) is a complex modulated oscillation (figure 5.7). Mathematically the time-dependence takes the form of a frequency-modulated signal, ω, with

carrier frequency $n\omega$. This similarity can be exploited to rewrite (5.34a) with a simpler time-dependence, at the expense of a more complex expression for the mode amplitude and depth dependence,

$$\vec{u}(z,t) = \frac{\vec{\tau}_w}{\rho\sqrt{fA(0)}} e^{-i\frac{\pi}{4}} \sum_{l=-\infty}^{\infty} \sum_{n=-\infty}^{\infty} \left[(-1)^n \frac{\sqrt{f}}{\sqrt{f+n\omega}} J_n(\gamma_n) J_{l-n}(\gamma_n) \Omega_n(z) \right] e^{il\omega t}. \quad (5.35)$$

5.4 Discussion of Results

In this section several pertinent aspects of the time-periodic solution (5.34a) will be explored, including a quantitative formulation of the rectification of velocity and shear in the time-averaged solution.

5.4.1 Qualitative Solution Characteristics

Figure 5.8 shows an example solution hodograph, where it assumed that A_v is elevated between $1800-0600$ hours, with the daily minimum occuring at 1200 hours. Velocity vectors trace closed contours over a 24 hour period, the time average of which is shown (heavy black), and which can be compared to the steady-state Ekman solution (dashed black). Differences between these lines represent rectification of the diurnal variability in A_v to the low-frequency velocity. Understanding and quantifying these rectification effects is the focus of section 5.4.3 below.

Further insight into the solution comes from considering the solution in the time-depth plane. Figure 5.9 shows an example solution for a mid-latitude Ekman layer forced by a constant zonal wind stress. In the early morning hours A_v is high, and the Ekman layer is at its deepest. As A_v decreases towards its mid-day minimum the Ekman layer begins to shoal, most clearly evident in the shoaling of the zero zonal velocity line from $\sim -1h_{Ek0}$ to $\sim -0.5h_{Ek0}$. A surface intensified diurnal jet develops (Price et al., 1986), associated with a highly sheared near surface layer. Below this high shear region, weak anticyclonic oscillations, with upward propagating phase, begin. In the near-surface ocean, near-inertial variability

with upward propagating phase is often attributed to inertial waves with downward energy propagation. However the one-dimensional nature of the solution considered here precludes the existence of inertial waves, and instead suggests these features should be interpreted as inertial oscillations, with phase propagation determined by the diurnal cycle in viscosity, as discussed further below.

The primary zonal momentum balance throughout the diurnal evolution is between the Coriolis acceleration, $-fv$, and the turbulent momentum flux convergence, $(A_v u_z)_z$, consistent with Ekman layer dynamics (figure 5.10). Near-the surface there is an alternating acceleration and deceleration of the flow on either side of the diurnal jet maximum, with weaker, upward propagating signals below. These signals are balanced largely by Coriolis acceleration, particularly in the deeper portion of the layer, a signature of inertial oscillations. These signals can thus be interpreted as inertial oscillations initiated by the loss of Ekman balance caused by the decreasing mid-day A_v. In this manner they are similar to the inertial oscillations observed in simple models of the nocturnal low-level jet in the atmospheric boundary layer, where it is found that a layer which abruptly transitions from viscid to inviscid dynamics, representing the change between daytime and nighttime dynamics, causes inertial oscillations around the mean state solution (Blackadar, 1957; Van de Wiel et al., 2010). In the model considered here the reduced A_v, as contrasted to a full transition to inviscid dynamics, leads to inertial oscillations which progressively shoal, following the shoaling Ekman layer.

Figure 5.11 compares a more realistic simulation from a 1D model forced by a diurnal cycle in surface buoyancy fluxes (Appendix A), utilizing the KPP parameterization (Large et al., 1994). The right panels represent the time-periodic solution, forced by the same surface wind stress, using values of A_v diagnosed from the KPP model output. Major features are well reproduced, including the near-surface diurnal jet, mid depth minima in zonal velocity, descending shear layers, suppressed nighttime shear, and enhancement of shear near the base of the turbulent boundary layer. Other features which are not well reproduced are the stronger inertial oscillations below the boundary layer evident in KPP, arising in part from

the slow decay of initial transients associated with the lack of internal wave radiation in the 1D model configuration, as well as the deep evolution of the descending diurnal shear layers, whose descent slows in the KPP model relative to the theoretical prediction, likely due to the space-time coupling of turbulent viscosity in KPP.

5.4.2 Parameter Dependence

In this section the parameter dependence of the solution (5.34a) will be explored to illustrate how the dynamics evolve across different regimes. The aspects of the solution unique to the diurnal cycle are evidently controlled by only two parameters, δ the strength of the diurnal A_v cycle, and f/ω, the ratio between the local inertial frequency and the period of the viscosity. Figure 5.12 illustrates the modification of boundary layer currents as δ is varied. Increasing δ increases the strength of the near-surface diurnal jet, as expected from the momentum balance discussed above. The strength, and location, of the inertial oscillations are also effected, with increasing δ leading to higher velocities, occurring closer to the surface and slightly later in the day. Similarly, with higher δ the enhanced near-surface shear persists later in the day, with evident subsurface maxima occurring several hours after the minimum A_v.

Figure 5.13 compares the effect of varying latitude, holding δ constant. At low latitudes an afternoon deepening of the sheared diurnal jet is evident, whereas the shear response becomes increasingly symmetric around the mid-day minimum in A_v as latitude increases. Upward phase propagation is evident only for 45°, which may arise from the inability of the periodic domain considered here to support inertial oscillations for latitudes $< 30°$, where the inertial period exceeds 1 day. This evolution is also affected by the vertical structure of A_v (figure 5.14), with lines of constant phase more nearly horizontal for values of A_v which decay away from the surface.

5.4.3 Rectification

Diurnal variability poses a challenge for the interpretation of observational data in terms of Ekman dynamics, as observations are frequently averaged in time in order to improve the signal to noise ratio and remove other forms of variability. Understanding the effect of time variability in A_v is thus critical to understanding time-averaged observations. Integrating the time-dependent solution (5.34a) over one diurnal cycle allows for comparison with the steady state solution ($\delta = 0$), which can be used to examine the rectification effects of the diurnal cycle in mixing. We define a diurnal average of a quantity $X(t)$ as,

$$\langle X \rangle = \frac{\omega}{2\pi} \int_0^{\frac{2\pi}{\omega}} X(t) \mathrm{d}t. \tag{5.36}$$

The solution for velocity averaged over one diurnal cycle is given by,

$$\langle \vec{u}(z) \rangle = \frac{\vec{\tau}_w}{\rho\sqrt{fA(0)}} e^{-i\frac{\pi}{4}} \sum_{n=-\infty}^{\infty} \left[\frac{\sqrt{f}}{\sqrt{f+n\omega}} J_n \left(\gamma_n\right)^2 \Omega_n(z) \right] \tag{5.37}$$

This takes on a particularly simple form at the surface where,

$$\langle \vec{u}(0) \rangle = \frac{\vec{\tau}_w}{\rho\sqrt{fA(0)}} e^{-i\frac{\pi}{4}} \sum_{n=-\infty}^{\infty} \left[\frac{\sqrt{f}}{\sqrt{f+n\omega}} J_n \left(\gamma_n\right)^2 \right] \tag{5.38}$$

As discussed above, the squared projection coefficients, J_n^2, roll off quickly with increasing mode number, particularly with the $(f+n\omega)^{-\frac{1}{2}}$ dependence. Thus, the time average solution for velocity will be dominated by the low modes. Similarly, the solution for surface shear averaged over one diurnal cycle can be found by vertically differentiating (5.37) and evaluating at $z = 0$,

$$\langle \vec{u}_z(0) \rangle = \frac{\vec{\tau}_w}{\rho A(0)} \sum_{n=-\infty}^{\infty} J_n \left(\gamma_n\right)^2 \tag{5.39}$$

The higher modes will contribute more to the time average shear solution, which will lead to larger rectification effects, emphasizing how surface velocity and shear will have different

responses to diurnal cycle in mixing, a result which is independent of the vertical structure of A_v.

A simple normalized measure of rectification, for a variable, X, can be defined as,

$$\hat{X}_R = \frac{||\langle X \rangle| - |\overline{X}||}{|\overline{X}|}, \tag{5.40}$$

where angle brackets as before represent averaging over the diurnal cycle and the bar notation represents the steady state solution, assuming no time variability in A_v ($\delta = 0$). This measure of rectification, (5.40), can then be applied to modeled and theoretical values of velocity and shear to assess the degree of rectification. This is shown for velocity and shear in figure 5.15 as functions of the controlling parameters. Velocity rectification increases with increasing δ, with reduced rectification effects at low-latitudes, due in part to the enhanced total velocities in the Ekman solution as $f \to 0$. Shear rectification is essentially latitude independent, which can be anticipated from (5.39), with a rapid increase at high δ and maximum values of $\widehat{U_{zR}} > 3$ as $\delta \to 1$. Thus while both velocity and shear are subject to rectification effects at all latitudes, the vertical structure of the time-averaged currents are more sensitive to time-variability in A_v than their magnitude, consistent with the findings from section 5.2.

As a basic confirmation of this parameter dependence we compare the approximate theory to a numerical solution which does not impose the same constraints on periodicity. To do this we numerically solve (5.2), subject to the boundary conditions (5.6) and (5.7). This initial-boundary value problem is initiated from a state of rest with a constant zonal wind stress, and the solution found for a sinusoidally varying A_v using a finite element Galerkin method (Skeel and Berzins, 1990). Model integrations are carried out for 50 days, and averages are taken over the last half of the integration. Rectification in this idealized model can be seen to follow closely to the theoretical prediction (figure 5.16), with only slight deviations for the predictions of shear rectification at high δ, potentially due to the finite difference estimates of shear we employ here. This result holds regardless of latitude, suggesting the time-periodic domain is not unduly influencing this result. Comparisons to a more complete model are

presented in Appendix A.

One additional consequence of the changes in the time-mean solution introduced by time-variability in A_v, (5.37), is that the time-mean current no longer directly satisfies a steady state Ekman solution. It can thus be anticipated directly from the solution that in order to effectively fit a steady Ekman layer solution to the resulting currents it will be necessary to define an 'effective' A_v which may differ significantly from the mean of the time-varying values, a result familiar from previous work on Ekman layer rectification (McWilliams et al., 2009).

Following McWilliams et al. (2009, equations 19-21) we can find a complex, depth-dependent, effective eddy viscosity A_v^{Eff} that fits the time-rectified diurnal solution to a steady-state Ekman model. This is shown for a diurnal cycle of A_v that is uniform in depth, which more clearly illustrates the modifications arising solely from diurnal variability (figure 5.17). The diurnal cycle of A_v leads to a reduction in near-surface A_v^{Eff}, necessary to generate the enhanced near-surface shears. In all cases there is a mid-depth maximum of A_v^{Eff} which moves deeper for increasing values of δ (off vertical scale for $\delta = 0.9$). The effective viscosity is rotated cyclonically relative to the mean shear, consistent with observations (Price and Sundermeyer, 1999), and numerical models (McWilliams et al., 2009). These results can be compared to those from McWilliams et al. (2009, their figure 20) which follow a similar overall structure, suggestive that the rectification mechanisms captured here are relevant to the more complete model physics considered therein.

5.5 Summary

In this work we have presented two simple models of the time-dependent Ekman layer with time-varying eddy viscosity, intended as a basic approximation of the complex and interdependent processes governing the real evolution of the ocean surface boundary layer under time-varying forcing. These models have the advantage of simplicity, illustrating the basic physics of how time-variability in mixing changes the ocean response to impulsively started wind forcing (section 5.2), and rectifies to the time-mean solution (section 5.3). This simplic-

ity comes at the trade-off of physical realism, particularly so in the constraints placed on the vertical structure of eddy viscosity, and that the turbulent viscosity is not allowed to evolve as a function of the resulting near-surface shear flows. The utility of these models can thus be viewed principally as a means of building physical insight and isolating processes which do not rely on these feedback mechanisms to occur, as for instance is discussed in regards to the time-mean effective eddy viscosity found in section 5.4.3. In this regards they can be considered similar to approaches adopted in the atmospheric sciences literature on the dynamics of nocturnal low-level jets (Blackadar, 1957; Buajitti and Blackadar, 1957; Sheih, 1972).

As guidance for the interpretation of observations, several conclusions can be drawn directly from the work presented here. The discussion of section 5.2 hints at the complexity of trying to infer the true A_v from measurements of interior velocities or boundary flux values (Wenegrat et al., 2014), which in general will require solution of a non-linear equation, the subject of a large body of literature on inversion techniques for the one-dimensional heat equation (cf. Cannon, 1984). The common approach of fitting steady-state Ekman models to time-averaged fields can be expected to result in values of A_v, possibly complex, which depart significantly from the true values, complicating their interpretation. This follows directly from changes in the mean vertical structure of the time-dependent solution, without requiring any feedback mechanism between shear flow and A_v, providing a simple explanation of observations (Price and Sundermeyer, 1999), that differs in interpretation from previous investigations (McWilliams et al., 2009).

Time-variability in A_v modifies both the early establishment of ocean currents and rectifies to the low-frequency flow. Velocity shear is more strongly rectified than velocity, and in both cases the magnitude of the rectification is only weakly dependent on latitude and dominated by the strength of the periodic variations in mixing. Finally, we note the upward propagating inertial oscillations which appear in our solution (figure 5.10), forced by the diurnal cycle in viscosity, and with vertical phase propagation speed determined by the rate at which the diffusive boundary layer shoals. The dynamics of these oscillations are exactly

those implicated in the creation of atmospheric nocturnal jets (Van de Wiel et al., 2010), however their presence in the oceanic boundary layer is less clearly documented, and hence deserves further investigation.

5.6 Appendix A: Numerical Model

In addition to the basic numerical solution discussed in section 5.4.3, we utilize the MITgcm (Marshall et al., 1997), run in an idealized one-dimensional configuration with 2 m vertical resolution, spanning from $z = -500$ to $z = 0$. This resolution is sufficient to resolve the Ekman layer in all simulations used. The model is initiated from a state of rest with a weak, vertically uniform, temperature stratification, equivalent to $N^2 = 2 \times 10^{-5}\,\mathrm{s}^{-2}$ ($T_z = 0.01\,\mathrm{C\,m}^{-1}$). A two-component surface buoyancy flux is imposed, consisting of incoming short-wave radiation which is absorbed in the surface layer using a Jerlov Type II absorption profile (Jerlov, 1976), and an outgoing surface flux, held steady in time. The idealized diurnal cycle is thus a repeating cycle of a function given by,

$$Q_{SWR}(t) = -Q_0 e^{-\left(\frac{(\hat{t}-0.5)}{0.25}\right)^2}, \tag{5.41}$$

where $Q_0 = 900\,Wm^{-2}$, and $\hat{t}$ ranges from $0-1$ daily. A constant outgoing surface heat flux is given by $Q_{LW} = 125\,Wm^{-2}$ This particular profile leads to ~ 12 hours of heat flux into the mixed layer (figure 5.18), which is an idealization taken to facilitate comparison between the model results and theory. These surface fluxes are held constant in time and latitude, which ignores variations in solar heat flux as a function of latitude and season, which will result in variability at frequencies other than the diurnal. Also important to note is that this forcing profile leads to a net heat flux into the ocean, which in the 1D configuration utilized here can only lead to increasing temperature stratification at the base of the turbulent boundary layer, affecting the evolution of the boundary layer depth. This can be accounted for by imposition of a restoring interior heat flux (as in McWilliams et al., 2009), however here we are simply comparing the basic theory to the model based on diagnosed fields, and are not

concerned with the detailed evolution of the turbulent boundary layer depth, and hence we do not impose additional sources of interior cooling.

Surface wind stress is taken to be purely zonal, with magnitude varied to affect variations in the strength of the diurnal mixing cycle. Turbulent viscosity is parameterized using KPP (Large et al., 1994), with parameters as in Large and Gent (1999), and calculated viscosities are output at every time step. The calculation of surface layer viscosities in KPP couples vertical structure and time-dependence, providing a more realistic model of near-surface turbulence than the simple dependence we require in section 5.3. All model integrations are performed for 100 days with a 20 minute integration time step.

The model output is principally useful as a point of qualitative comparison, as in figure 5.11. However, it is also possible to provide at least a basic assessment of the rectification effects discussed in section 5.4.3. To do this we run the above model repeatedly, varying latitude from $5^\circ - 90^\circ$ in 5° increments, and wind stress $\tau = 0.1 - 0.4\,\mathrm{N\,m^{-2}}$, holding the diurnal surface buoyancy flux profiles constant across runs. In KPP the coupling of space-time variability in A_v means there is no principled manner to effect the decomposition in order to estimate a steady-state solution for calculation of rectification values. Here we make the simple ad hoc assumption that the vertical structure can be taken as the time average $A_v(z)$ over the last-half of the integration period. We then estimate δ by fitting a diurnally periodic sine function to the average A_v in the turbulent surface boundary layer. Using these two estimates it is possible to compare the estimated rectification to the theory, shown in figure 5.19.

Velocity rectification is reproduced remarkably well, however shear rectification is greatly overestimated for values of $\delta > 0.8$. Several reasons for this are suggested. One, the method of estimating δ is somewhat arbitrary, as the coupling of spatial structure and time-dependence in KPP means that near-surface A_v is generally subject to smaller diurnal fluctuations than deeper in the boundary layer. Shear rectification is particularly sensitive at high δ (figure 5.15), and hence may be particularly sensitive to incorrect estimates of this parameter. Secondly, higher vertical modes contribute more strongly to shear rectification than velocity

rectification. These higher modes, with their small vertical scale and the associated strong shear, may be damped in a more realistic turbulence closure such as KPP, where wind-driven shear feeds back into the determination of A_v. Finally, the cases of high δ tend to occur at low latitudes, associated with the deeper boundary layers in KPP generated in response to periodic buoyancy forcing (McWilliams et al., 2009), which results in increasingly non-sinusoidal time-variability of A_v. Hence, some of the departure of the model results from the theory may implicate the time-varying structure of A_v as departing from the basic theoretical assumptions.

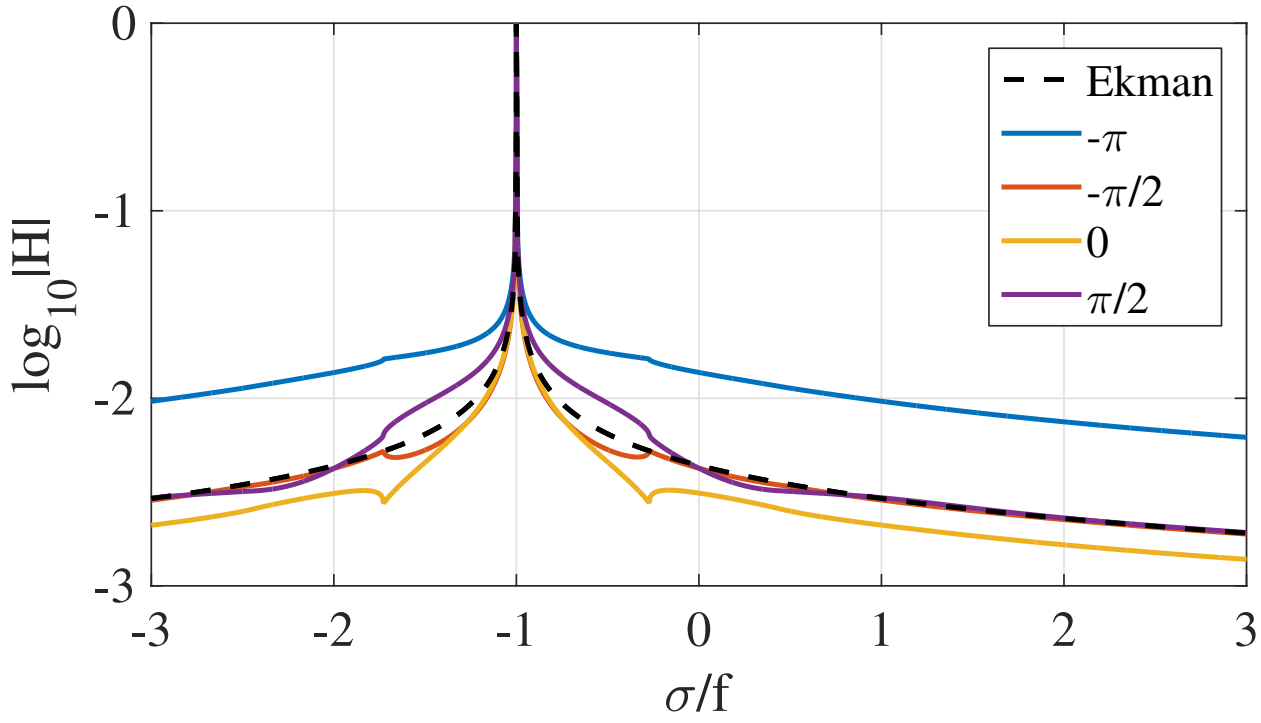

Figure 5.1: Estimated transfer function amplitude, by phase. The theoretical constant viscosity Ekman transfer function (dashed black) is unbounded at $\sigma = -f$. All values shown are estimated numerically for consistency, and normalized by the maximum estimated value of the constant viscosity solution.

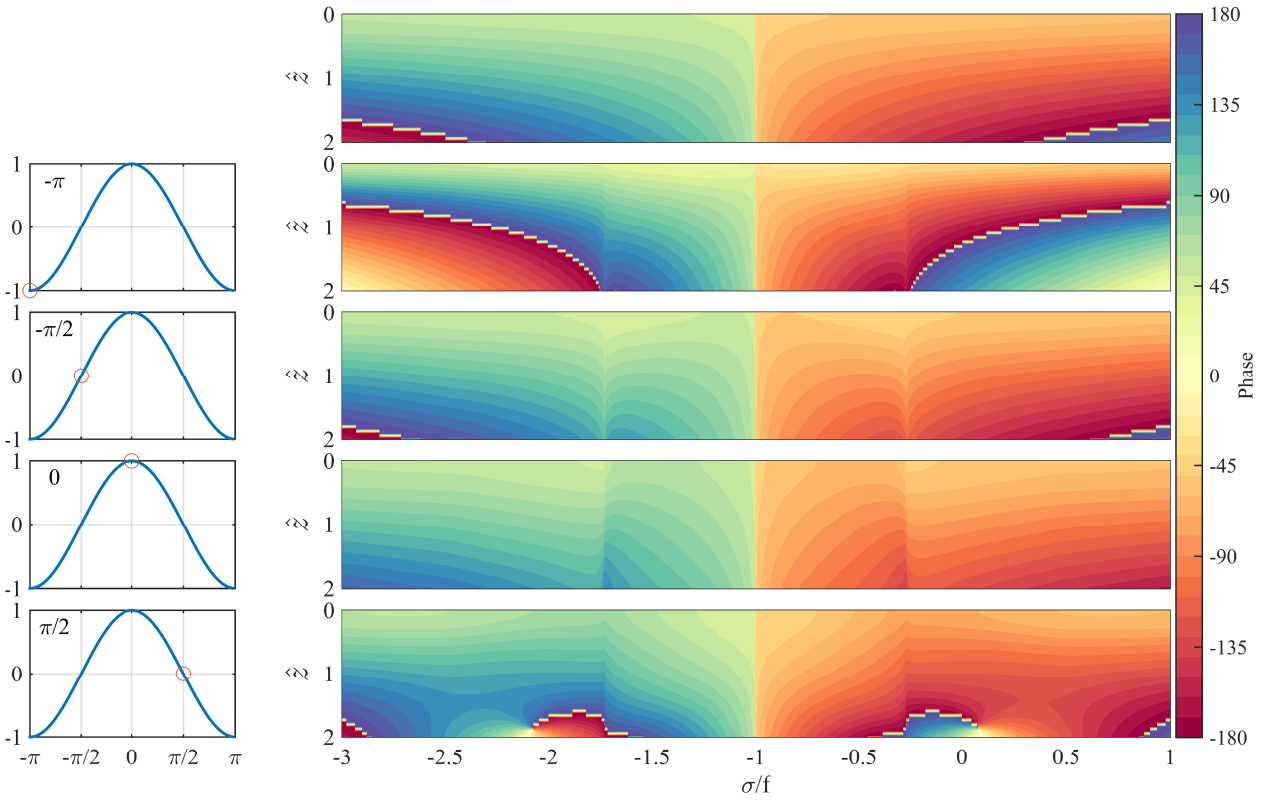

Figure 5.2: Rotary spectral phase of the velocity transfer function, as a function of depth (normalized by the steady state Ekman depth). Top: Steady Ekman solution. Following panels, $H(\sigma)$ defined by the Fourier transform of (5.11), with initial A_v phase as indicated in the left column.

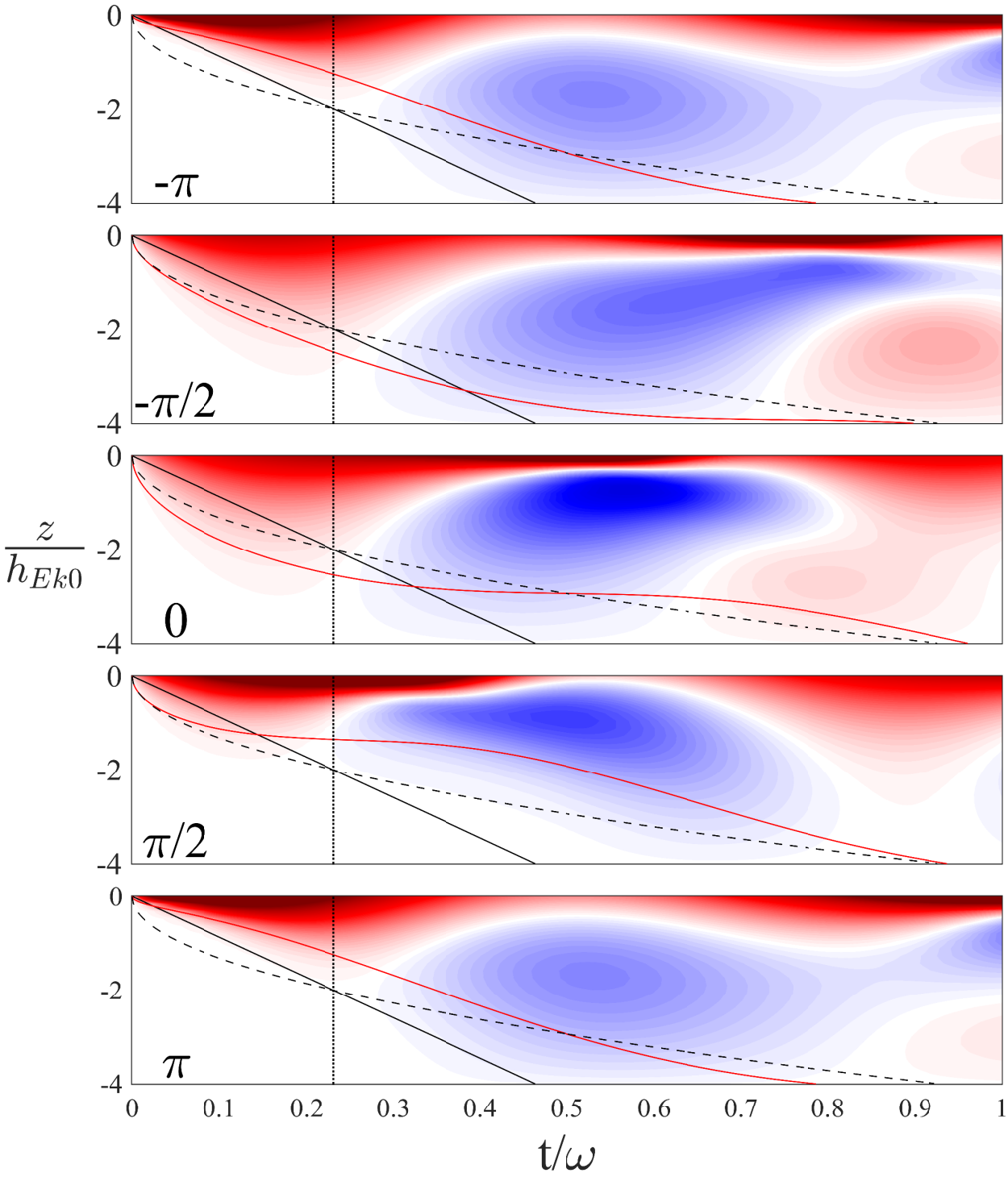

Figure 5.3: Zonal current response to impulsively started steady zonal wind stress, with $\delta = 0.9$, and phase, ψ, as indicated on each panel. The diffusive depth scale $-2\sqrt{Q(t)}$ is shown in red, the constant A_v diffusive scale $-2\sqrt{A_{v0}t}$ is dashed black, and the rotational depth scale $-fth_{Ek0}$ in solid black. The dotted black line indicates the half-pendulum day, $t = 2f^{-1}$.

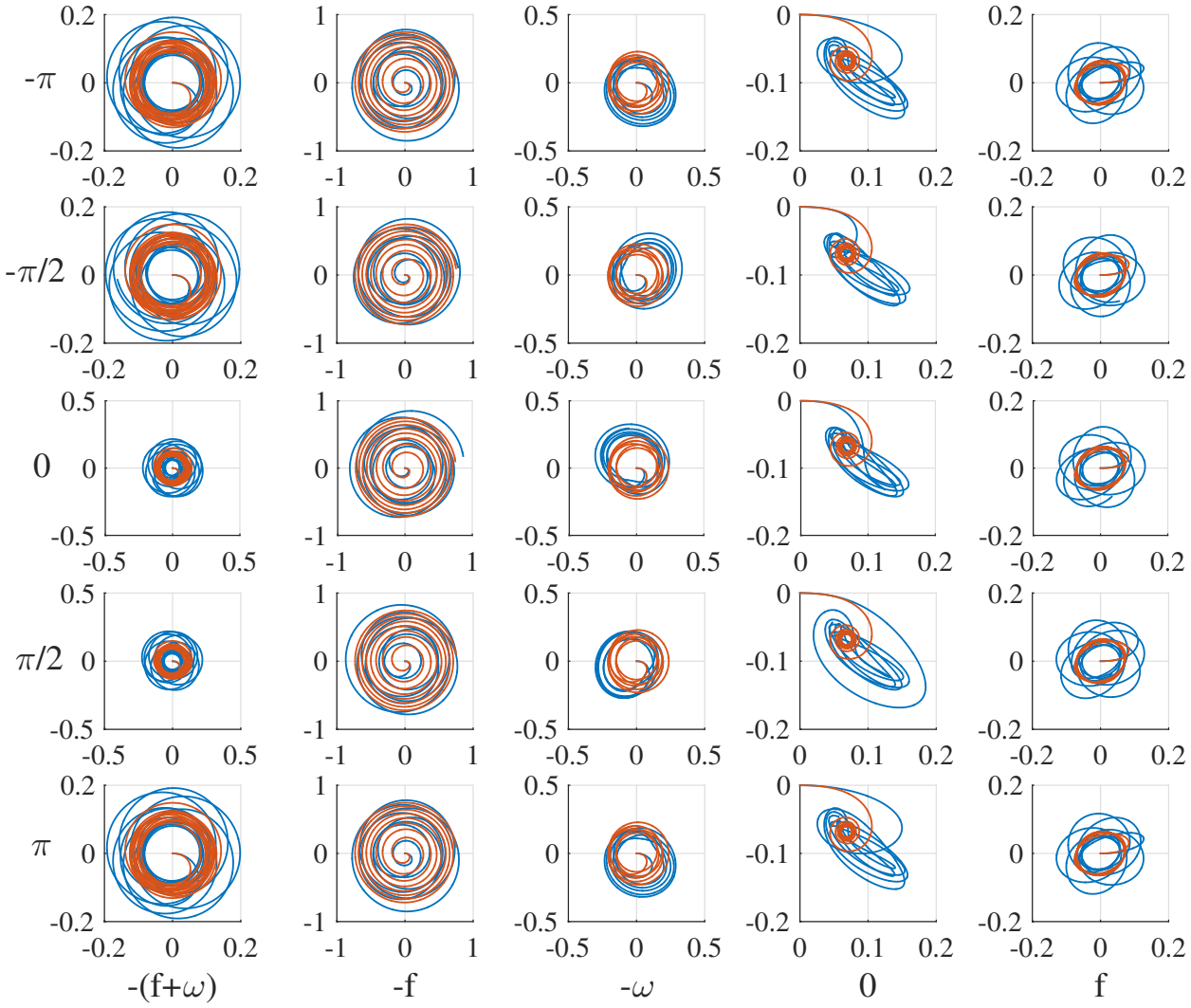

Figure 5.4: Hodographs of the menagerie of spin-up problems resulting from rotary wind stress forcing, with rotary frequency indicated along the bottom row, and A_v phase indicated at left. In each plot, zonal velocity is along the x-axis ($m\,s^{-1}$), meridional velocity along the y-axis ($m\,s^{-1}$), and orange lines indicate the $\delta = 0$ solution, blue lines the solution for $\delta = 0.8$. The solution is shown for 8 inertial periods, with problem parameters: $|\vec{\tau}| = 0.1\,\mathrm{N\,m^{-2}}$, $f = 1 \times 10^{-4}\,\mathrm{s^{-1}}$, and $A_{v0} = 1 \times 10^{-2}\,\mathrm{m^2\,s^{-1}}$.

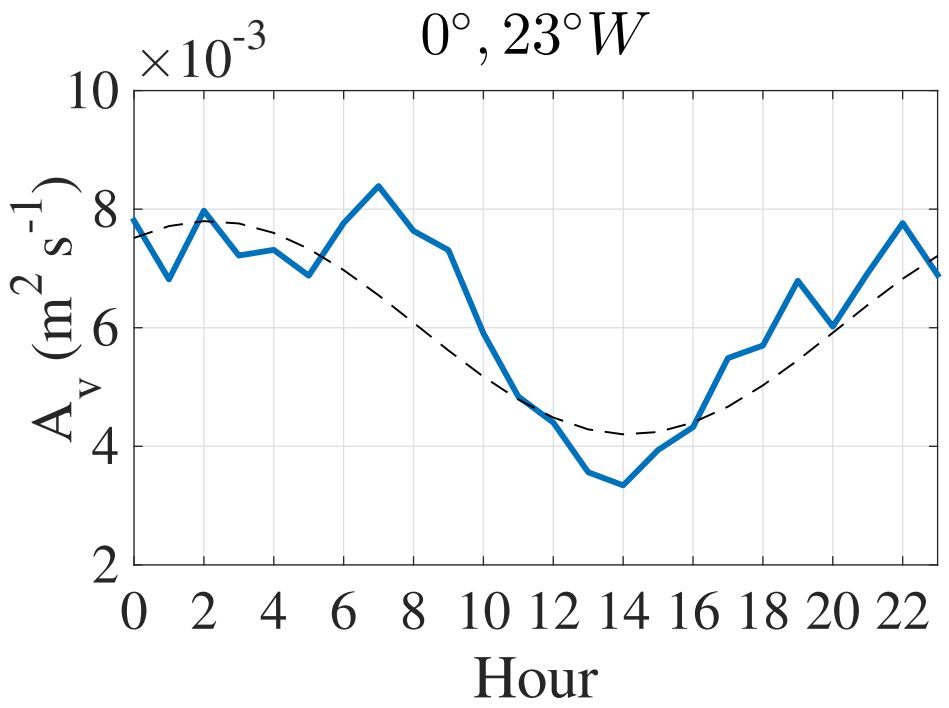

Figure 5.5: Composite diurnal cycle in A_v at 0°, 23°W, $z = -5.6\,\mathrm{m}$, inferred from observations (blue), and a sinusoidal fit (dashed), with $\delta = 0.35$. These observations are discussed in detail in Wenegrat and McPhaden (2015a, their section 4.1).

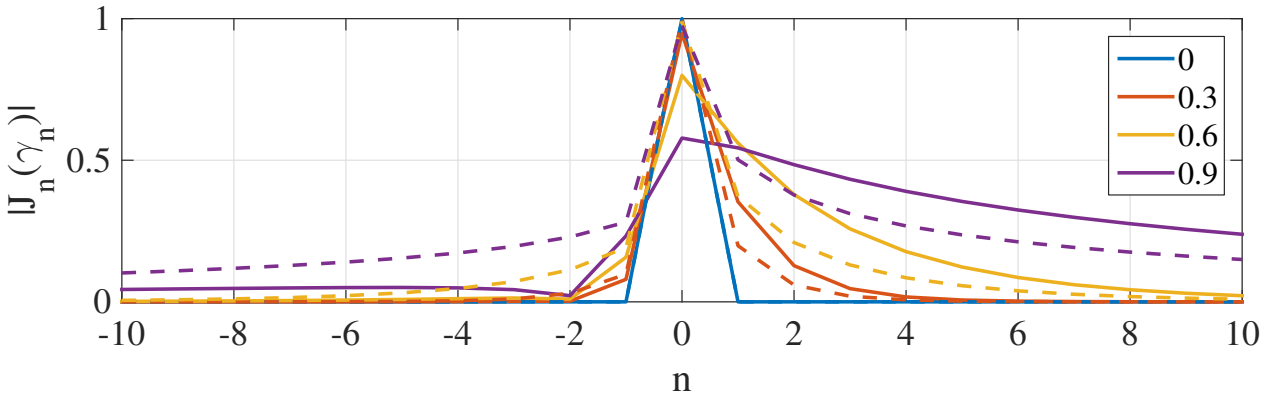

Figure 5.6: Bessel function wind-stress coupling coefficients for the first ±10 modes at 10° (dashed) and 50° (solid), for values of δ as indicated

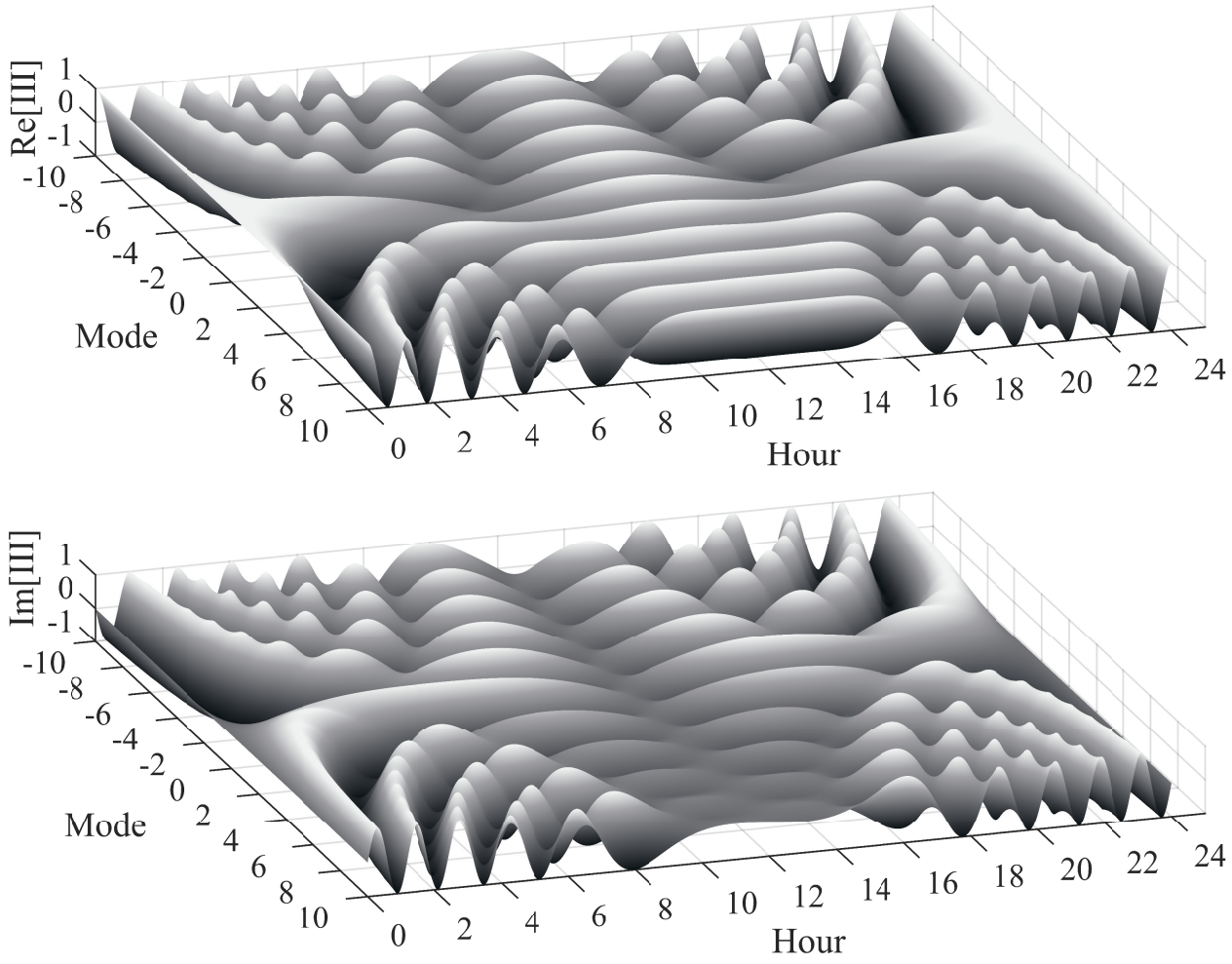

Figure 5.7: Time dependence for the first ± 10 modes, assuming $\delta = 0.9$, and latitude 50°. Top, real components, bottom: imaginary components.

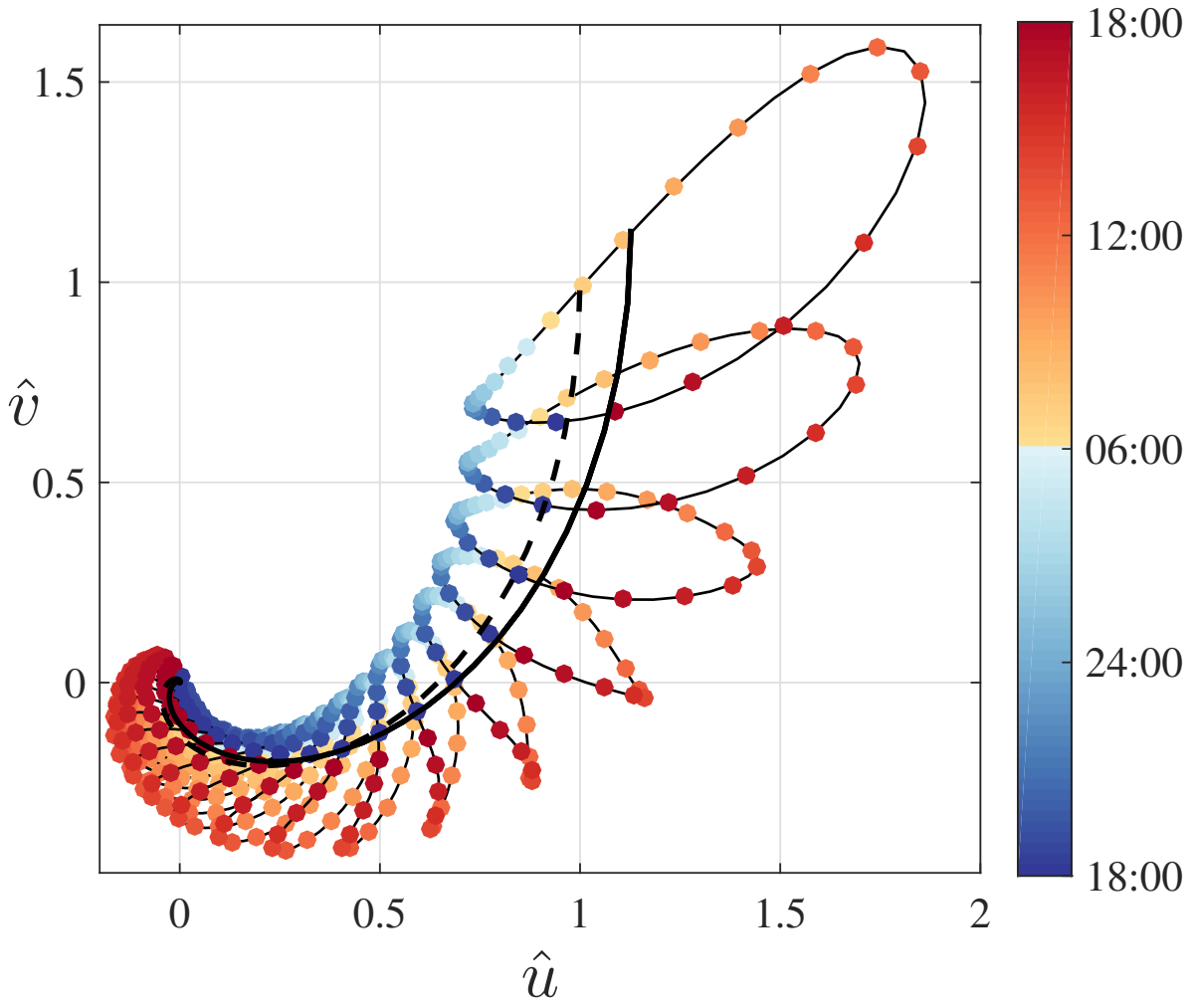

Figure 5.8: Example diurnal cycle velocity hodograph, with $h_{Ek} = 14\,\mathrm{m}$ and $\delta = 0.7$. At each depth the velocity vector traces a closed contour over one 24 hour period, plotted for selected depths, beginning at $z = 0$ and decreasing in increments of 2 m (thin lines, with color scale indicating hour of day). The time averaged diurnal velocity is shown (heavy black), as is the steady state solution (dashed black). All velocities are normalized by the steady-state Ekman surface velocity.

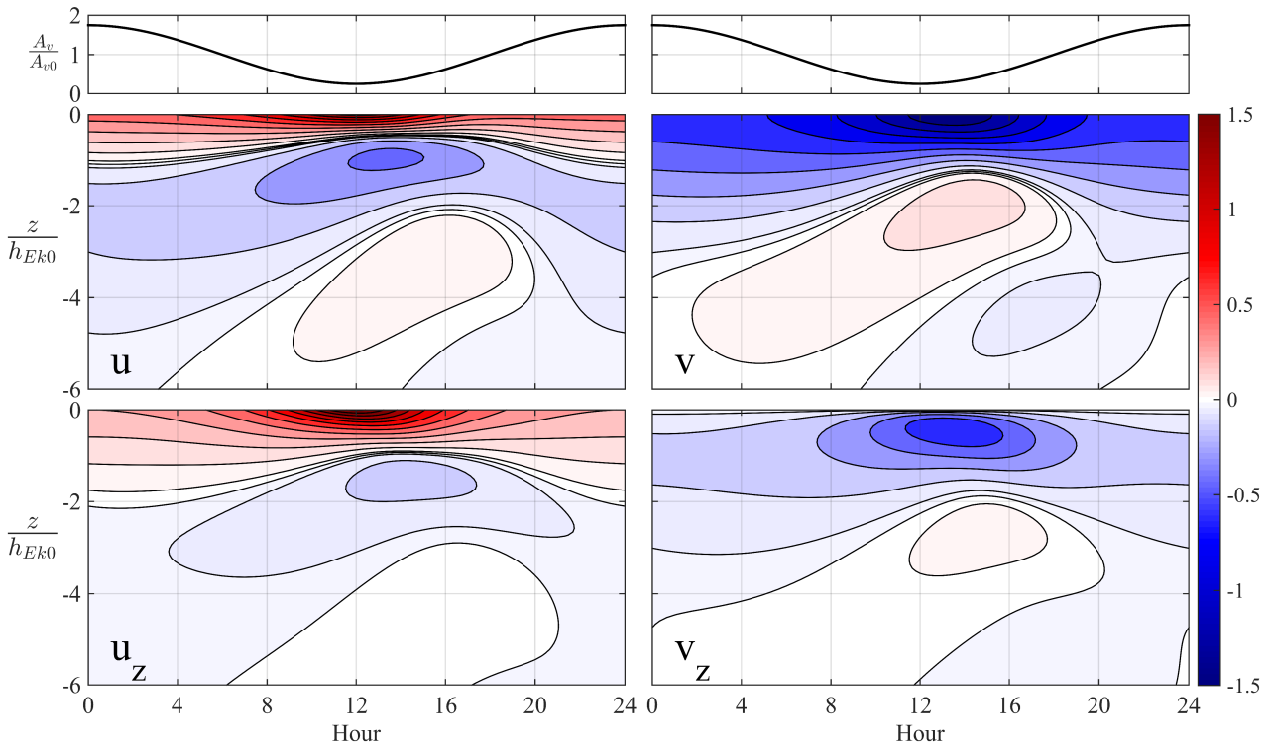

Figure 5.9: Modeled diurnal cycle at $45°N$, for vertically uniform A_v, and $\delta = 0.75$. Velocities are normalized by $\tau/(\rho\sqrt{fA_{v0}})$, and shear normalized by $2\tau/(\rho A_{v0})$, twice the surface shear for the constant viscosity solution. Contours are non-linearly spaced to capture the deep variability.

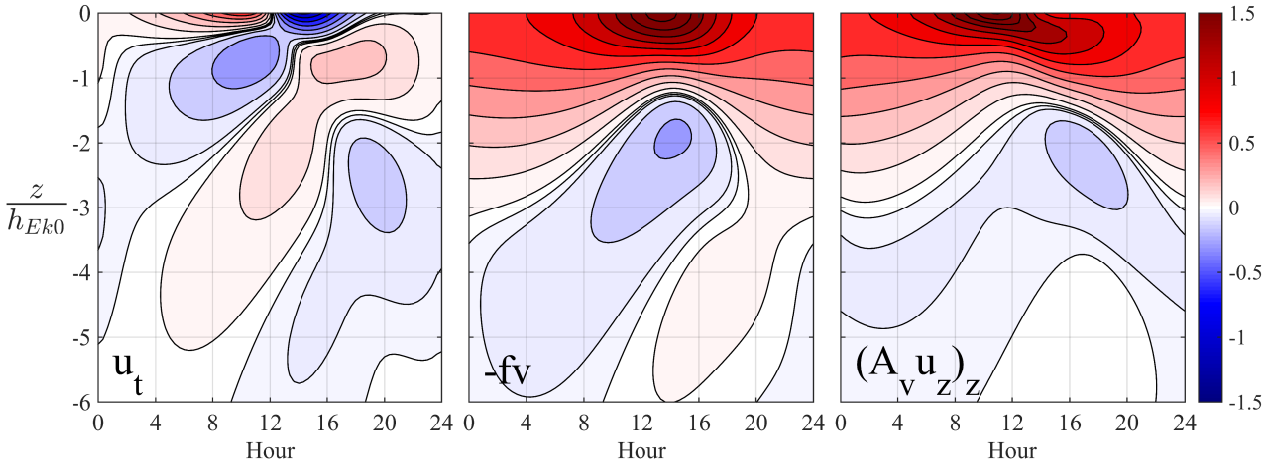

Figure 5.10: Momentum balance terms for the same case considered in figure 5.9, with values normalized by $\tau/(\rho h_{Ek0})$.

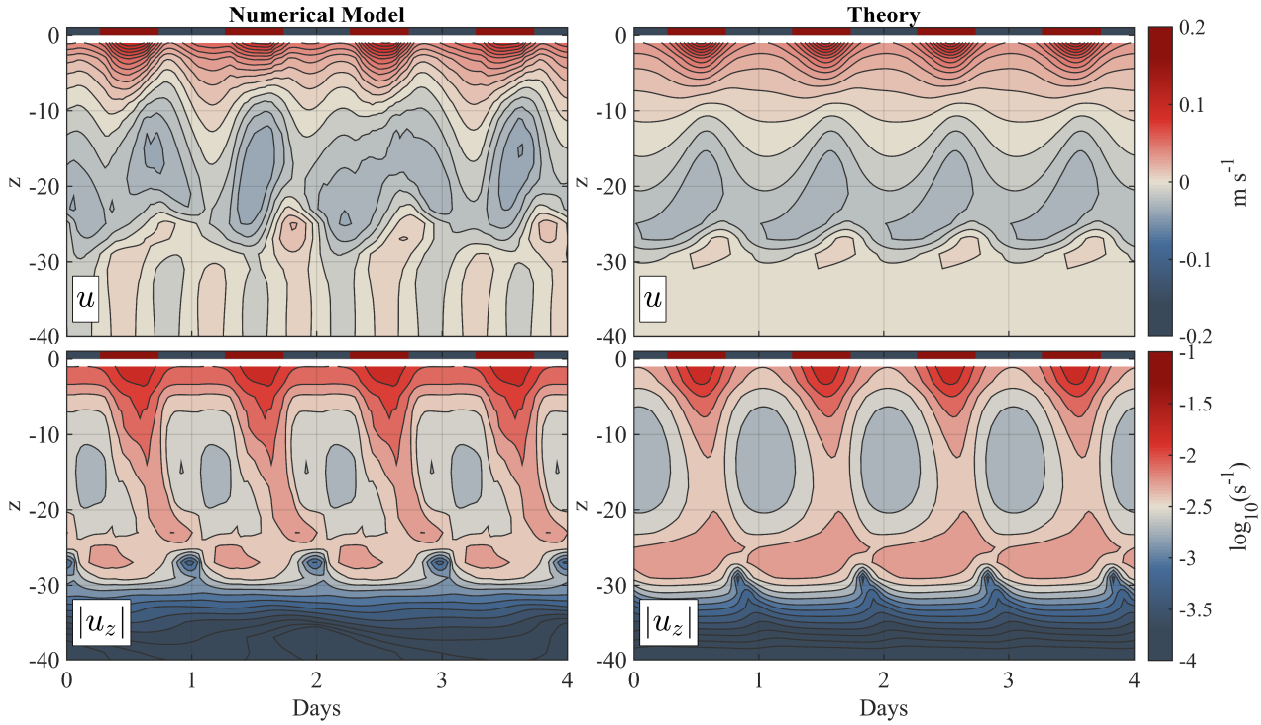

Figure 5.11: Comparison of numerical model and theoretical solution for $45°N$, with $\tau = 0.1\,\mathrm{N\,m^{-2}}$. Parameters for the theoretical solution are diagnosed from the numerical solution following the discussion in Appendix A, and the boundary value problems (5.20) are solved numerically rather than utilizing the WKBJ approximate solution. Times of negative (red) and positive (blue) net surface buoyancy flux are indicated in each plot for $z > 0$.

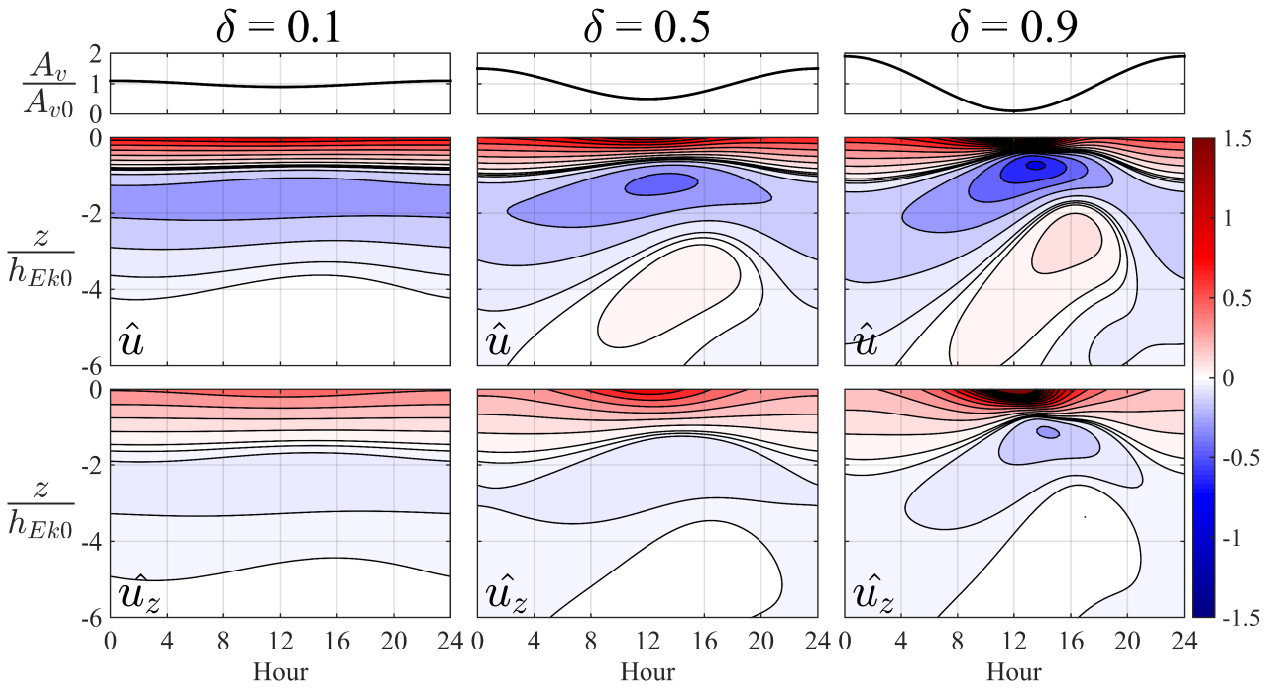

Figure 5.12: Effect of varying δ with parameters and normalization as given for figure 5.9.

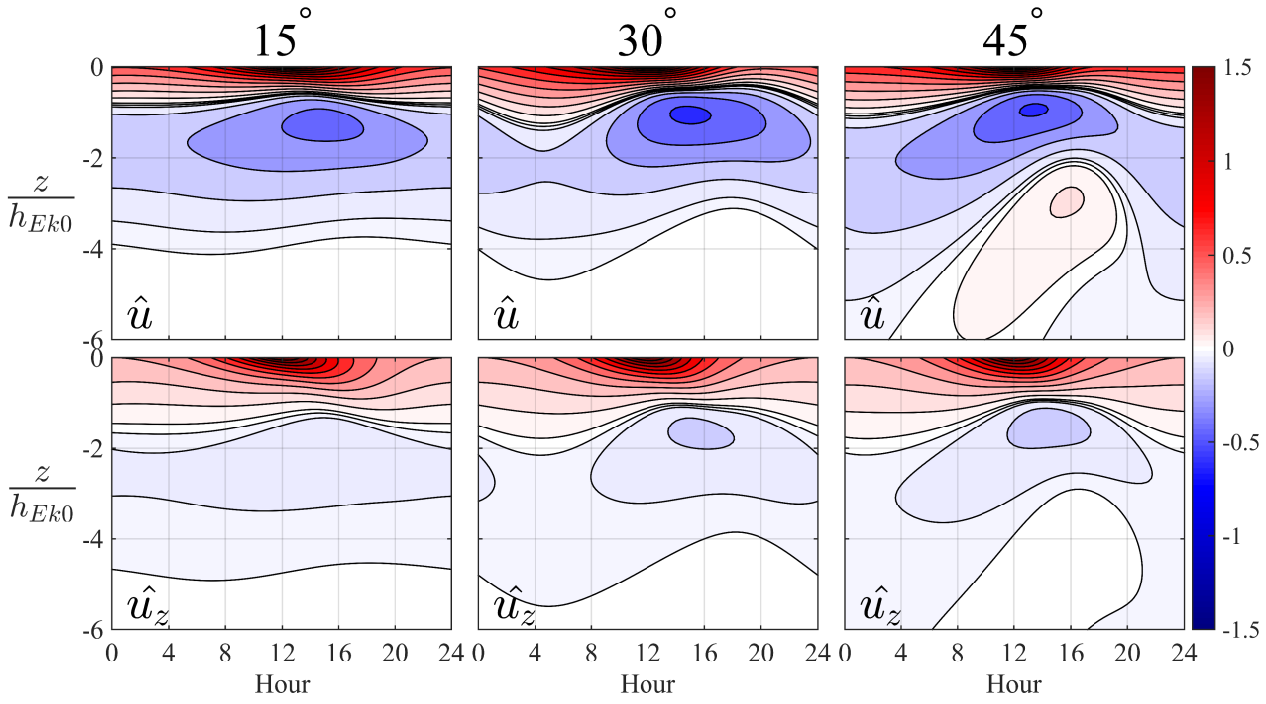

Figure 5.13: Effect of varying latitude, with parameters and normalization as given for figure 5.9. Note both the velocity and depth normalizations are a function of latitude.

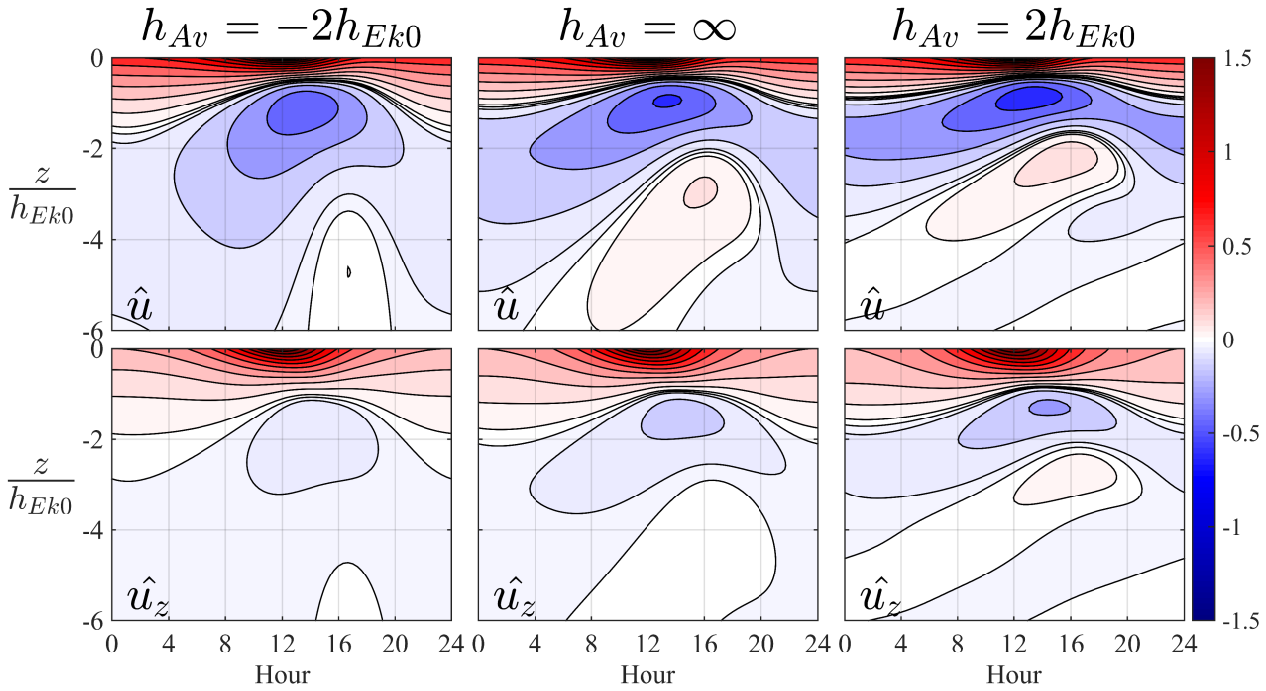

Figure 5.14: Effect of vertically varying A_v, such that $A(z) = A_{v0}e^{z/h_{Av}}$, with parameters and normalization as given for figure 5.9. Negative (positive) values imply A_v that increases (decreases) downwards. Solutions are found numerically.

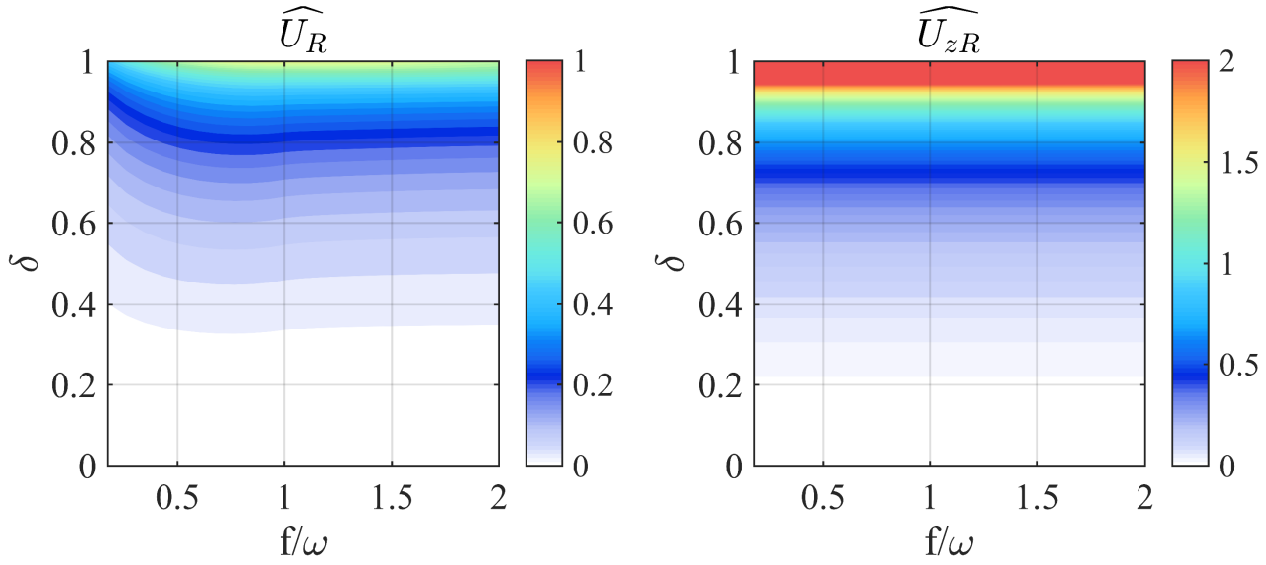

Figure 5.15: Parameter dependence of the theoretical rectification solution (5.40) for velocity (left) and shear (right).

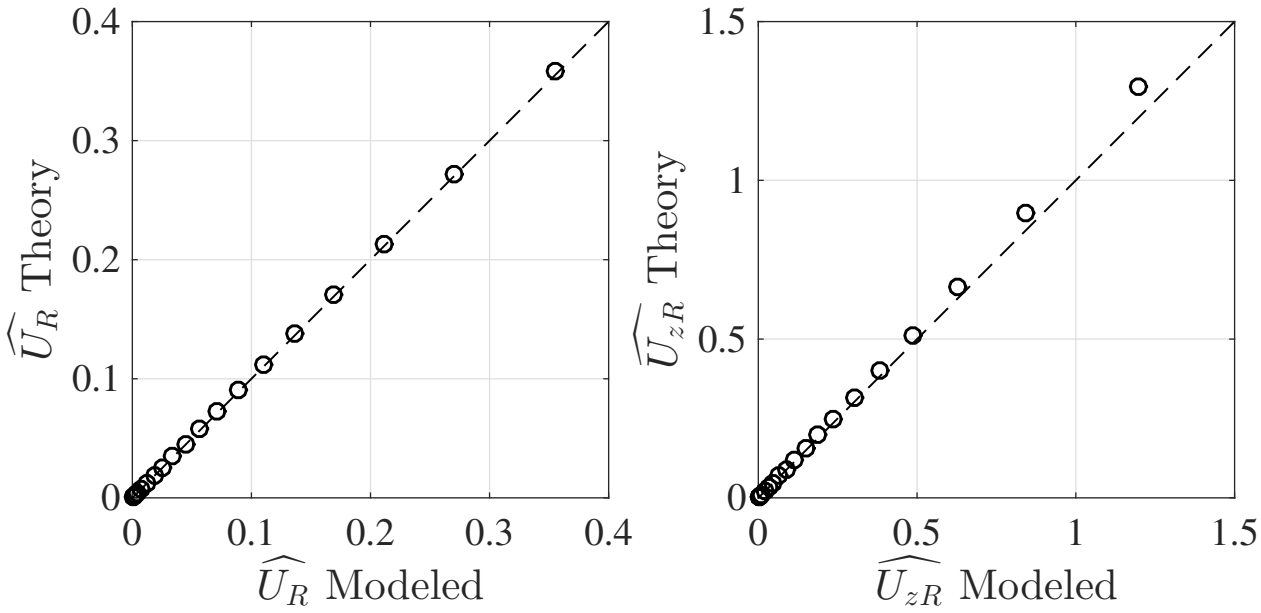

Figure 5.16: Validation of the rectification implied by the time-periodic solution against a numerical solution of the initial-boundary-value problem as discussed in section 5.4.3.

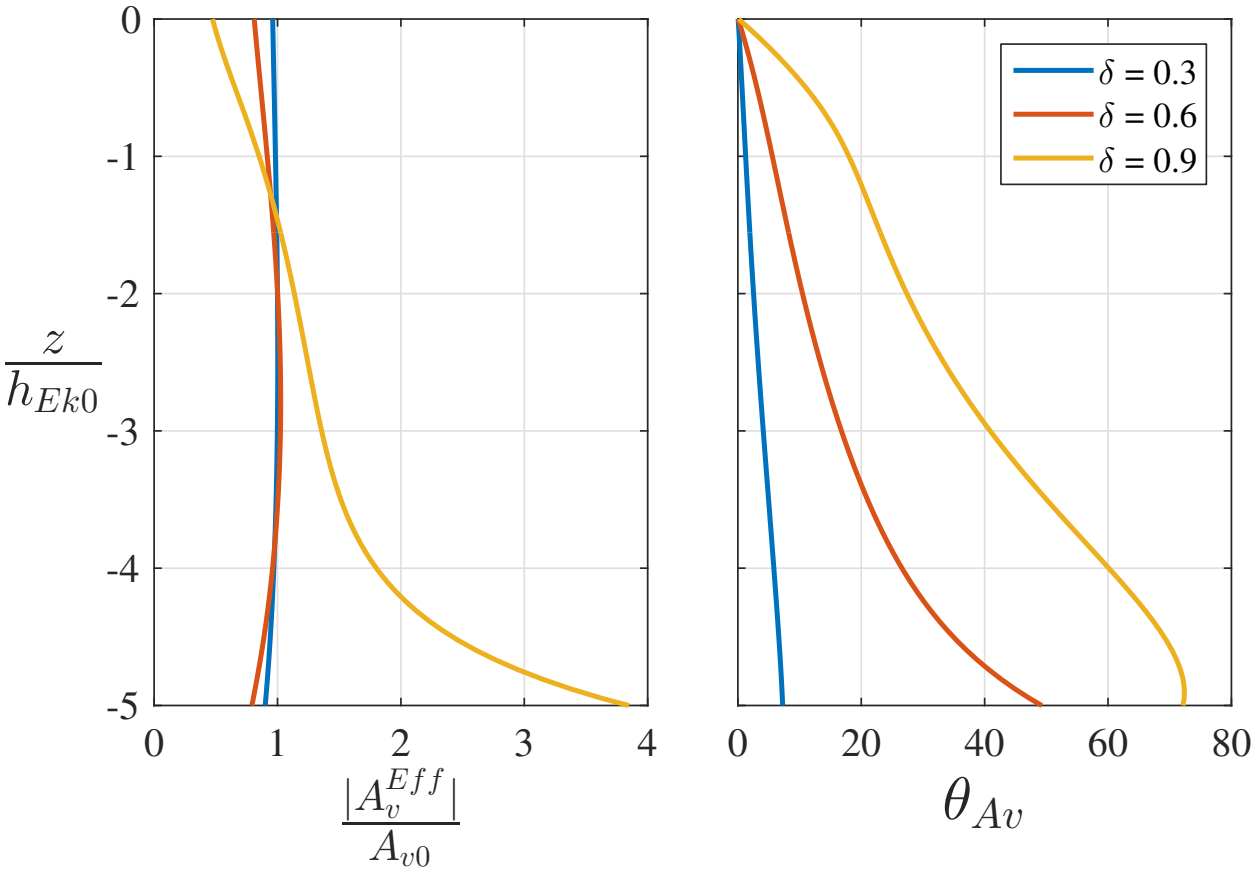

Figure 5.17: Effective eddy viscosities inferred from the time mean solution for vertically uniform A_v and various δ values as shown in the legend. A_v^{Eff} magnitudes are normalized by the true A_v, angles (°) are relative to the local mean-shear direction.

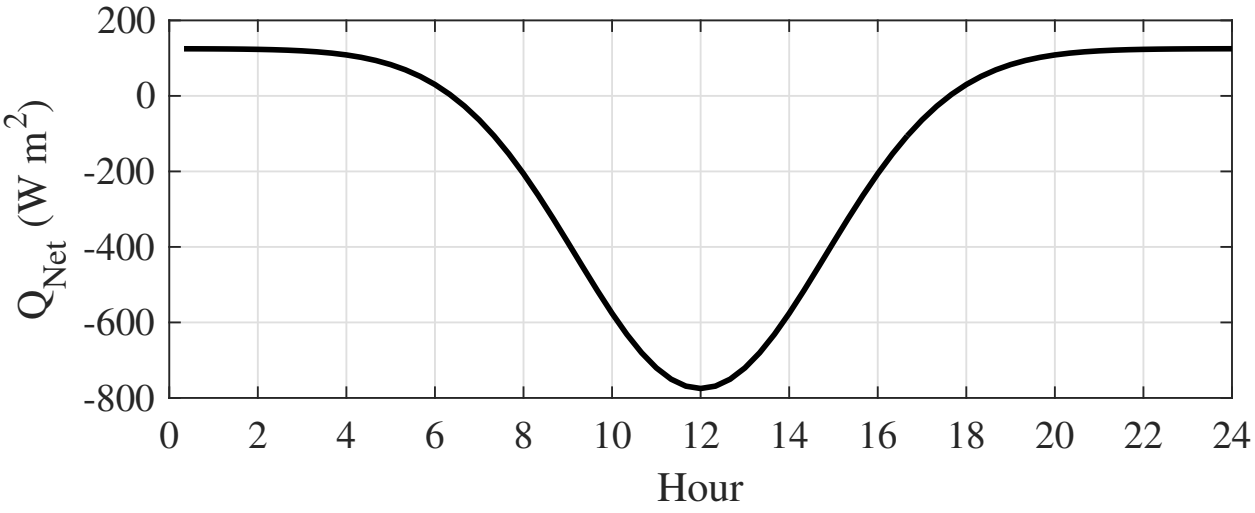

Figure 5.18: Idealized diurnal cycle of net surface heat flux used to force the numerical model discussed in Appendix A.

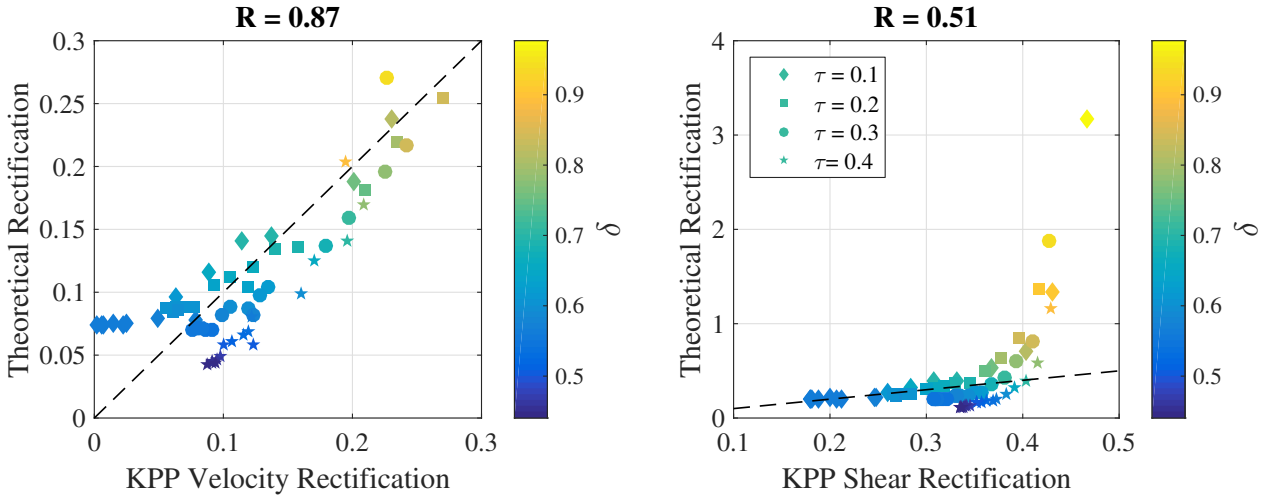

Figure 5.19: Comparison of inferred rectification in the KPP model against theoretical predictions for velocity (left) and shear (right). In each plot, colorscale gives the inferred δ, symbol shape gives the magnitude of the surface wind-stress as shown in the legend, and the dashed line indicates the 1-1 line. Correlation coefficients are shown above each plot.

Chapter 6

CONCLUSION

The results presented in this thesis further our understanding of the dynamics of the upper ocean, with an emphasis on how ocean dynamical processes affect the upper ocean response to atmospheric forcing. Ocean sources of shear in the presence of viscosity act as sources of stress, modifying boundary layer flows. Shear variability modifies the near-surface eddy viscosity, with important implications for parameterizations. The dynamical response of the wind-forced mixed layer to the diurnal cycle of surface buoyancy flux leads to a diurnal cycle of turbulent mixing, associated with equatorial deep-cycle turbulence. Rectification of time-varying mixing modifies the low-frequency boundary layer flow.

Understanding of the upper ocean response to surface forcing is thus predicated on an understanding of the feedbacks and interactions between physical processes which occur in the boundary layer. Many of these interactions and physical processes remain poorly understood compared to the basic theoretical conceptual model of an ocean responding passively to surface forcing. The broad range of spatial and temporal scales over which these dynamics are active, as well as the intrinsic difficulty of observing this near-surface layer, make this an ongoing challenge for the oceanographic community. However, the broad importance of understanding these boundary layer dynamics suggests that it should remain a focus for future theoretical, numerical, and observational work.

BIBLIOGRAPHY

Abramowitz, M., and I. A. Stegun, Eds., 1964: *Handbook of mathematical functions: with formulas, graphs, and mathematical tables*. Dover books on mathematics, Dover Publications, New York, NY.

Aiki, H., and R. J. Greatbatch, 2012: Thickness-Weighted Mean Theory for the Effect of Surface Gravity Waves on Mean Flows in the Upper Ocean. *Journal of Physical Oceanography*, **42 (5)**, 725–747, doi:10.1175/JPO-D-11-095.1.

Belcher, S. E., and Coauthors, 2012: A global perspective on Langmuir turbulence in the ocean surface boundary layer: FRONTIER. *Geophysical Research Letters*, **39 (18)**, n/a–n/a, doi:10.1029/2012GL052932.

Bender, C. M., and S. A. Orszag, 1978: *Advanced mathematical methods for scientists and engineers*. Springer, New York.

Berger, B. W., and B. Grisogono, 1998: The baroclinic, variable eddy viscosity Ekman layer. *Boundary-Layer Meteorology*, **87 (3)**, 363–380.

Bernie, D. J., E. Guilyardi, G. Madec, J. M. Slingo, and S. J. Woolnough, 2007: Impact of resolving the diurnal cycle in an oceanatmosphere GCM. Part 1: a diurnally forced OGCM. *Climate Dynamics*, **29 (6)**, 575–590, doi:10.1007/s00382-007-0249-6.

Bernie, D. J., E. Guilyardi, G. Madec, J. M. Slingo, S. J. Woolnough, and J. Cole, 2008: Impact of resolving the diurnal cycle in an oceanatmosphere GCM. Part 2: A diurnally coupled CGCM. *Climate Dynamics*, **31 (7-8)**, 909–925, doi:10.1007/s00382-008-0429-z.

Blackadar, A. K., 1957: Boundary layer wind maxima and their significance for the growth of nocturnal inversions. *Bull. Amer. Meteor. Soc*, **38 (5)**, 283–290.

Bloomfield, P., 1976: *Fourier Decomposition of Time Series: An Introduction*. John Wiley, New York, NY.

Boccaletti, G., R. Ferrari, and B. Fox-Kemper, 2007: Mixed Layer Instabilities and Restratification. *Journal of Physical Oceanography*, **37 (9)**, 2228–2250, doi:10.1175/JPO3101.1.

Bond, N. A., and M. J. McPhaden, 1995: An indirect estimate of the diurnal cycle in upper ocean turbulent heat fluxes at the equator, 140W. *Journal of Geophysical Research*, **100 (C9)**, 18 369, doi:10.1029/95JC01592.

Bonjean, F., and G. S. E. Lagerloef, 2002: Diagnostic Model and Analysis of the Surface Currents in the Tropical Pacific Ocean. *Journal of Physical Oceanography*, **32 (10)**, 2938–2954, doi:10.1175/1520-0485(2002)032⟨2938:DMAAOT⟩2.0.CO;2.

Bourlès, B., and Coauthors, 2008: The Pirata Program: History, Accomplishments, and Future Directions. *Bulletin of the American Meteorological Society*, **89 (8)**, 1111–1125, doi:10.1175/2008BAMS2462.1.

Boyer, T., 2013: World Ocean Database 2013. *NOAA Atlas NESDIS 72*, National Oceanic and Atmospheric Administration, Silver Spring, MD.

Brainerd, K. E., and M. C. Gregg, 1993: Diurnal restratification and turbulence in the oceanic surface mixed layer: 1. Observations. *Journal of Geophysical Research*, **98 (C12)**, 22 645, doi:10.1029/93JC02297.

Brainerd, K. E., and M. C. Gregg, 1995: Surface mixed and mixing layer depths. *Deep Sea Research Part I: Oceanographic Research Papers*, **42 (9)**, 1521–1543, doi:10.1016/0967-0637(95)00068-H.

Buajitti, K., and A. K. Blackadar, 1957: Theoretical studies of diurnal wind-structure variations in the planetary boundary layer. *Quarterly Journal of the Royal Meteorological Society*, **83 (358)**, 486–500, doi:10.1002/qj.49708335804.

Buckingham, E., 1914: On Physically Similar Systems; Illustrations of the Use of Dimensional Equations. *Physical Review*, **4 (4)**, 345–376, doi:10.1103/PhysRev.4.345.

Caldwell, D. R., C. W. Van Atta, and K. N. Helland, 1972: A laboratory study of the turbulent Ekman layer. *Geophysical Fluid Dynamics*, **3 (1)**, 125–160, doi:10.1080/03091927208236078.

Cannon, J. R., 1984: *The one-dimensional heat equation*, Encyclopedia of mathematics and its applications, Vol. 23. Cambridge University Press, Cambridge, U.K.

Chelton, D., and S.-P. Xie, 2010: Coupled Ocean-Atmosphere Interaction at Oceanic Mesoscales. *Oceanography*, **23 (4)**, 52–69, doi:10.5670/oceanog.2010.05.

Chelton, D. B., R. A. de Szoeke, M. G. Schlax, K. El Naggar, and N. Siwertz, 1998: Geographical Variability of the First Baroclinic Rossby Radius of Deformation. *Journal of Physical Oceanography*, **28 (3)**, 433–460, doi:10.1175/1520-0485(1998)028⟨0433:GVOTFB⟩2.0.CO;2.

Chen, S. S., and R. A. Houze, 1997: Diurnal variation and life-cycle of deep convective systems over the tropical Pacific warm pool. *Quarterly Journal of the Royal Meteorological Society*, **123 (538)**, 357–388, doi:10.1002/qj.49712353806.

Chereskin, T. K., 1995: Direct evidence for an Ekman balance in the California Current. *Journal of Geophysical Research*, **100 (C9)**, 18 261, doi:10.1029/95JC02182.

Chereskin, T. K., and D. Roemmich, 1991: A Comparison of Measured and Wind-derived Ekman Transport at 11N in the Atlantic Ocean. *Journal of Physical Oceanography*, **21 (6)**, 869–878, doi:10.1175/1520-0485(1991)021⟨0869:ACOMAW⟩2.0.CO;2.

Chu, P. C., 2015: Ekman Spiral in a Horizontally Inhomogeneous Ocean with Varying Eddy Viscosity. *Pure and Applied Geophysics*, doi:10.1007/s00024-015-1063-4.

Clayson, C. A., and A. Chen, 2002: Sensitivity of a Coupled Single-Column Model in the Tropics to Treatment of the Interfacial Parameterizations. *Journal of Climate*, **15 (14)**, 1805–1831, doi:10.1175/1520-0442(2002)015⟨1805:SOACSC⟩2.0.CO;2.

Clayson, C. A., and J. A. Curry, 1996: Determination of surface turbulent fluxes for the Tropical Ocean-Global Atmosphere Coupled Ocean-Atmosphere Response Experiment: Comparison of satellite retrievals and in situ measurements. *Journal of Geophysical Research*, **101 (C12)**, 28 515, doi:10.1029/96JC02022.

Clayson, C. A., and D. Weitlich, 2007: Variability of Tropical Diurnal Sea Surface Temperature. *Journal of Climate*, **20 (2)**, 334–352, doi:10.1175/JCLI3999.1.

Corless, R. M., G. H. Gonnet, D. E. G. Hare, D. J. Jeffrey, and D. E. Knuth, 1996: On the Lambert W function. *Advances in Computational Mathematics*, **5 (1)**, 329–359, doi:10.1007/BF02124750.

Crawford, W., and T. Osborn, 1979: Microstructure measurements in the Atlantic equatorial undercurrent during GATE. *Deep Sea Res., Part A*, **26 (suppl. 2)**, 285–308.

Cribari-Neto, F., 2004: Asymptotic inference under heteroskedasticity of unknown form. *Computational Statistics & Data Analysis*, **45 (2)**, 215–233, doi:10.1016/S0167-9473(02)00366-3.

Cronin, M. F., and W. S. Kessler, 2002: Seasonal and interannual modulation of mixed layer variability at 0, 110W. *Deep Sea Research Part I: Oceanographic Research Papers*, **49 (1)**, 1–17, doi:10.1016/S0967-0637(01)00043-7.

Cronin, M. F., and W. S. Kessler, 2009: Near-Surface Shear Flow in the Tropical Pacific Cold Tongue Front. *Journal of Physical Oceanography*, **39 (5)**, 1200–1215, doi:10.1175/2008JPO4064.1.

Cronin, M. F., and M. J. McPhaden, 1999: Diurnal cycle of rainfall and surface salinity in the Western Pacific Warm Pool. *Geophysical Research Letters*, **26 (23)**, 3465–3468, doi:10.1029/1999GL010504.

Cronin, M. F., and T. Tozuka, 2015: Ekman ocean response to wind forcing in extratropical frontal regions. *19th Conference on Air-Sea Interaction*, Phoenix, AZ.

Csanady, G., 1982: Frictional Secondary Circulation Near An Upwelled Thermocline. Woods Hole Oceanog. Inst. Tech. Rept. WHOI-82-52.

Csanady, G. T., and P. T. Shaw, 1980: The evolution of a turbulent Ekman layer. *Journal of Geophysical Research*, **85 (C3)**, 1537, doi:10.1029/JC085iC03p01537.

Dai, A., and K. E. Trenberth, 2004: The Diurnal Cycle and Its Depiction in the Community Climate System Model. *Journal of Climate*, **17 (5)**, 930–951, doi:10.1175/1520-0442(2004)017⟨0930:TDCAID⟩2.0.CO;2.

Danabasoglu, G., W. G. Large, J. J. Tribbia, P. R. Gent, B. P. Briegleb, and J. C. McWilliams, 2006: Diurnal Coupling in the Tropical Oceans of CCSM3. *Journal of Climate*, **19 (11)**, 2347–2365, doi:10.1175/JCLI3739.1.

Davis, R., R. de Szoeke, and P. Niiler, 1981: Variability in the upper ocean during MILE. Part II: Modeling the mixed layer response. *Deep Sea Research Part A. Oceanographic Research Papers*, **28 (12)**, 1453–1475, doi:10.1016/0198-0149(81)90092-3.

Dewey, R. K., and J. N. Moum, 1990: Enhancement of fronts by vertical mixing. *Journal of Geophysical Research*, **95 (C6)**, 9433, doi:10.1029/JC095iC06p09433.

Dillon, T. M., J. N. Moum, T. K. Chereskin, and D. R. Caldwell, 1989: Zonal Momentum Balance at the Equator. *Journal of Physical Oceanography*, **19 (5)**, 561–570, doi:10.1175/1520-0485(1989)019⟨0561:ZMBATE⟩2.0.CO;2.

Donlon, C. J., P. J. Minnett, C. Gentemann, T. J. Nightingale, I. J. Barton, B. Ward, and M. J. Murray, 2002: Toward Improved Validation of Satellite Sea Surface Skin Temperature Measurements for Climate Research. *Journal of Climate*, **15 (4)**, 353–369, doi:10.1175/1520-0442(2002)015⟨0353:TIVOSS⟩2.0.CO;2.

Drushka, K., S. T. Gille, and J. Sprintall, 2014: The diurnal salinity cycle in the tropics. *Journal of Geophysical Research: Oceans*, **119 (9)**, 5874–5890, doi:10.1002/2014JC009924.

Efron, B., and R. Tibshirani, 1993: An introduction to the bootstrap. *Monographs on Statistics and Applied Probability*, Vol. 57, Chapman and Hall, New York, NY.

Eisenhauer, J. G., 2003: Regression through the Origin. *Teaching Statistics*, **25 (3)**, 76–80, doi:10.1111/1467-9639.00136.

Ekman, V., 1905: On the Influence of the Earth's Rotation on Ocean-Currents. *Ark. Mat. Astron. Fys.*, **2**, 1–53.

Elipot, S., and S. T. Gille, 2009: Ekman layers in the Southern Ocean: spectral models and observations, vertical viscosity and boundary layer depth. *Ocean Science*, **5 (2)**, 115–139, doi:10.5194/os-5-115-2009.

Fairall, C. W., E. F. Bradley, J. E. Hare, A. A. Grachev, and J. B. Edson, 2003: Bulk Parameterization of AirSea Fluxes: Updates and Verification for the COARE Algorithm. *Journal of Climate*, **16 (4)**, 571–591, doi:10.1175/1520-0442(2003)016⟨0571:BPOASF⟩2.0.CO;2.

Flato, G., and e. al, 2013: Evaluation of climate models. *Climate Change 2013: The Physical Science Basis. Contribution of Working Group I to the Fifth Assessment Report of the Intergovernmental Panel on Climate Change*, T. Stocker, Ed., Cambridge Univ. Press, Cambridge, U.K.

Foltz, G. R., 2003: Seasonal mixed layer heat budget of the tropical Atlantic Ocean. *Journal of Geophysical Research*, **108 (C5)**, doi:10.1029/2002JC001584.

Foltz, G. R., and M. J. McPhaden, 2010: Abrupt equatorial wave-induced cooling of the Atlantic cold tongue in 2009. *Geophysical Research Letters*, **37 (24)**, n/a–n/a, doi:10.1029/2010GL045522.

Foltz, G. R., M. J. McPhaden, and R. Lumpkin, 2012: A Strong Atlantic Meridional Mode Event in 2009: The Role of Mixed Layer Dynamics. *Journal of Climate*, **25 (1)**, 363–380, doi:10.1175/JCLI-D-11-00150.1.

Freitag, H., T. Sawatzky, K. Ronnholm, and M. J. McPhaden, 2005: Calibration procedures and instrumental accuracy estimates of next generation ATLAS water temperature and pressure measurements. *NOAA Tech. Memo. OAR PMEL-128, NTIS: PB2008-101764*, NOAA/Pacific Marine Environmental Laboratory, Seattle, WA.

Garrett, C. J. R., and J. W. Loder, 1981: Dynamical Aspects of Shallow Sea Fronts. *Philosophical Transactions of the Royal Society A: Mathematical, Physical and Engineering Sciences*, **302 (1472)**, 563–581, doi:10.1098/rsta.1981.0183.

Gill, A. E., 1982: *Atmosphere-ocean dynamics*. International geophysics series, Academic Press, New York.

Gonella, J., 1971: A local study of inertial oscillations in the upper layers of the ocean. *Deep Sea Research and Oceanographic Abstracts*, **18 (8)**, 775–788, doi:10.1016/0011-7471(71)90045-3.

Gonella, J., 1972: A rotary-component method for analysing meteorological and oceanographic vector time series. *Deep Sea Research and Oceanographic Abstracts*, **19 (12)**, 833–846, doi:10.1016/0011-7471(72)90002-2.

Grant, A. L. M., and S. E. Belcher, 2009: Characteristics of Langmuir Turbulence in the Ocean Mixed Layer. *Journal of Physical Oceanography*, **39 (8)**, 1871–1887, doi:10.1175/2009JPO4119.1.

Gregg, M. C., H. Peters, J. C. Wesson, N. S. Oakey, and T. J. Shay, 1985: Intensive measurements of turbulence and shear in the equatorial undercurrent. *Nature*, **318 (6042)**, 140–144, doi:10.1038/318140a0.

Grisogono, B., 1995: A generalized Ekman layer profile with gradually varying eddy diffusivities. *Quarterly Journal of the Royal Meteorological Society*, **121 (522)**, 445–453, doi:10.1002/qj.49712152211.

Grodsky, S. A., 2005: Tropical instability waves at 0N, 23W in the Atlantic: A case study using Pilot Research Moored Array in the Tropical Atlantic (PIRATA) mooring data. *Journal of Geophysical Research*, **110 (C8)**, doi:10.1029/2005JC002941.

Gula, J., M. J. Molemaker, and J. C. McWilliams, 2014: Submesoscale Cold Filaments in the Gulf Stream. *Journal of Physical Oceanography*, **44 (10)**, 2617–2643, doi:10.1175/JPO-D-14-0029.1.

Halpern, D., and R. K. Reed, 1976: Heat Budget of the Upper Ocean Under Light Winds. *Journal of Physical Oceanography*, **6 (6)**, 972–975, doi:10.1175/1520-0485(1976)006⟨0972:HBOTUO⟩2.0.CO;2.

Hazel, P., 1972: Numerical studies of the stability of inviscid stratified shear flows. *Journal of Fluid Mechanics*, **51 (01)**, 39, doi:10.1017/S0022112072001065.

Hebert, D., J. N. Moum, C. A. Paulson, D. R. Caldwell, T. K. Chereskin, and M. J. McPhaden, 1991: The role of the turbulent stress divergence in the equatorial Pacific zonal momentum balance. *Journal of Geophysical Research*, **96 (C4)**, 7127, doi:10.1029/91JC00271.

Hidaka, K., 1955: Wind circulation in a two-layer zonal ocean. *Jap. J. Geophys*, **1**.

Huang, N. E., 1971: Derivation of Stokes drift for a deep-water random gravity wave field. *Deep Sea Research and Oceanographic Abstracts*, **18 (2)**, 255–259, doi:10.1016/0011-7471(71)90115-X.

Huang, N. E., 1979: On surface drift currents in the ocean. *Journal of Fluid Mechanics*, **91 (01)**, 191, doi:10.1017/S0022112079000112.

Hummels, R., 2012: On the variability of turbulent mixing within the upper layers of the Atlantic cold tongue region. Ph.D. thesis, Universittsbibliothek Kiel, Kiel, Germany.

Hummels, R., M. Dengler, and B. Bourles, 2013: Seasonal and regional variability of upper ocean diapycnal heat flux in the Atlantic cold tongue. *Progress in Oceanography*, **111**, 52–74, doi:10.1016/j.pocean.2012.11.001.

Hummels, R., M. Dengler, P. Brandt, and M. Schlundt, 2014: Diapycnal heat flux and mixed layer heat budget within the Atlantic Cold Tongue. *Climate Dynamics*, **43 (11)**, 3179–3199, doi:10.1007/s00382-014-2339-6.

Inoue, R., R.-C. Lien, and J. N. Moum, 2012: Modulation of equatorial turbulence by a tropical instability wave. *Journal of Geophysical Research*, **117 (C10)**, doi:10.1029/2011JC007767.

Jenkins, A. D., 1986: A Theory for Steady and Variable Wind-and Wave-Induced Currents. *Journal of Physical Oceanography*, **16 (8)**, 1370–1377, doi:10.1175/1520-0485(1986)016⟨1370:ATFSAV⟩2.0.CO;2.

Jerlov, N. G., 1976: *Marine Optics*. Elsevier, Amsterdam.

Jochum, M., P. Malanotte-Rizzoli, and A. Busalacchi, 2004: Tropical instability waves in the Atlantic Ocean. *Ocean Modelling*, **7 (1-2)**, 145–163, doi:10.1016/S1463-5003(03)00042-8.

Kawai, Y., and A. Wada, 2007: Diurnal sea surface temperature variation and its impact on the atmosphere and ocean: A review. *Journal of Oceanography*, **63 (5)**, 721–744, doi:10.1007/s10872-007-0063-0.

Kim, S. Y., P. M. Kosro, and A. L. Kurapov, 2014: Evaluation of directly wind-coherent near-inertial surface currents off Oregon using a statistical parameterization and analytical

and numerical models. *Journal of Geophysical Research: Oceans*, **119 (10)**, 6631–6654, doi:10.1002/2014JC010115.

Kirincich, A. R., 2013: Long-Term Observations of Turbulent Reynolds Stresses over the Inner Continental Shelf. *Journal of Physical Oceanography*, **43 (12)**, 2752–2771, doi:10.1175/JPO-D-12-0153.1.

Komen, G. J., Ed., 1996: *Dynamics and modelling of ocean waves*. 1st ed., Cambridge Univ. Press, Cambridge.

Kunze, E., A. J. Williams, and M. G. Briscoe, 1990: Observations of shear and vertical stability from a neutrally buoyant float. *Journal of Geophysical Research*, **95 (C10)**, 18 127, doi:10.1029/JC095iC10p18127.

Large, W. G., and P. R. Gent, 1999: Validation of Vertical Mixing in an Equatorial Ocean Model Using Large Eddy Simulations and Observations. *Journal of Physical Oceanography*, **29 (3)**, 449–464, doi:10.1175/1520-0485(1999)029⟨0449:VOVMIA⟩2.0.CO;2.

Large, W. G., J. C. McWilliams, and S. C. Doney, 1994: Oceanic vertical mixing: A review and a model with a nonlocal boundary layer parameterization. *Reviews of Geophysics*, **32 (4)**, 363, doi:10.1029/94RG01872.

Legeckis, R., 1977: Long Waves in the Eastern Equatorial Pacific Ocean: A View from a Geostationary Satellite. *Science*, **197 (4309)**, 1179–1181, doi:10.1126/science.197.4309.1179.

Levitus, S., 1982: Climatological Atlas of the World Ocean. *NOAA Prof. Paper #13*, US Government Printing Office, Washington, D.C.

Lewis, D., and S. Belcher, 2004: Time-dependent, coupled, Ekman boundary layer solutions incorporating Stokes drift. *Dynamics of Atmospheres and Oceans*, **37 (4)**, 313–351, doi:10.1016/j.dynatmoce.2003.11.001.

Liebmann, B., 1996: Description of a complete (interpolated) outgoing longwave radiation dataset. *Bull. Amer. Meteor. Soc.*, **77**, 1275–1277.

Lien, R.-C., D. R. Caldwell, M. C. Gregg, and J. N. Moum, 1995: Turbulence variability at the equator in the central Pacific at the beginning of the 1991-1993 El Nino. *Journal of Geophysical Research*, **100 (C4)**, 6881, doi:10.1029/94JC03312.

Lien, R.-C., E. A. D'Asaro, and C. E. Menkes, 2008: Modulation of equatorial turbulence by tropical instability waves. *Geophysical Research Letters*, **35 (24)**, doi:10.1029/2008GL035860.

Lister, J. R., and H. A. Stone, 1996: Time-dependent viscous deformation of a drop in a rapidly rotating denser fluid. *Journal of Fluid Mechanics*, **317 (-1)**, 275, doi:10.1017/S0022112096000754.

Lumpkin, R., and G. C. Johnson, 2013: Global ocean surface velocities from drifters: Mean, variance, El Nino-Southern Oscillation response, and seasonal cycle: Global Ocean Surface Velocities. *Journal of Geophysical Research: Oceans*, **118 (6)**, 2992–3006, doi:10.1002/jgrc.20210.

Lupini, R., A. Speranza, and A. Trevisan, 1975: A re-examination of the classical formulation of turbulent Ekman boundary layer flow. *Il Nuovo Cimento B Series 11*, **25 (2)**, 871–881, doi:10.1007/BF02724758.

Madsen, O. S., 1977: A Realistic Model of the Wind-Induced Ekman Boundary Layer. *Journal of Physical Oceanography*, **7 (2)**, 248–255, doi:10.1175/1520-0485(1977)007⟨0248:ARMOTW⟩2.0.CO;2.

Mahadevan, A., and A. Tandon, 2006: An analysis of mechanisms for submesoscale vertical motion at ocean fronts. *Ocean Modelling*, **14 (3-4)**, 241–256, doi:10.1016/j.ocemod.2006.05.006.

Mangat, P. S., and B. T. Molloy, 1994: Prediction of long term chloride concentration in concrete. *Materials and Structures*, **27 (6)**, 338–346, doi:10.1007/BF02473426.

Marshall, J., C. Hill, L. Perelman, and A. Adcroft, 1997: Hydrostatic, quasi-hydrostatic, and nonhydrostatic ocean modeling. *Journal of Geophysical Research*, **102 (C3)**, 5733, doi:10.1029/96JC02776.

Maury, M., 1864: *The Physical Geography of the Sea, and Its Meteorology*. Sampson Low, Son & Marston, London, U.K.

McCreary, J. P., K. E. Kohler, R. R. Hood, S. Smith, J. Kindle, A. S. Fischer, and R. A. Weller, 2001: Influences of diurnal and intraseasonal forcing on mixed-layer and biological variability in the central Arabian Sea. *Journal of Geophysical Research*, **106 (C4)**, 7139, doi:10.1029/2000JC900156.

McPhaden, M. J., 1981: Continuously Stratified Models of the Steady-State Equatorial Ocean. *Journal of Physical Oceanography*, **11 (3)**, 337–354, doi:10.1175/1520-0485(1981)011⟨0337:CSMOTS⟩2.0.CO;2.

McPhaden, M. J., 1993: Trade wind fetch-related variations in equatorial undercurrent depth, speed, and transport. *Journal of Geophysical Research*, **98 (C2)**, 2555, doi:10.1029/92JC02683.

McWilliams, J. C., and B. Fox-Kemper, 2013: Oceanic wave-balanced surface fronts and filaments. *Journal of Fluid Mechanics*, **730**, 464–490, doi:10.1017/jfm.2013.348.

McWilliams, J. C., J. Gula, M. J. Molemaker, L. Renault, and A. F. Shchepetkin, 2015: Filament Frontogenesis by Boundary Layer Turbulence. *Journal of Physical Oceanography*, doi:10.1175/JPO-D-14-0211.1.

McWilliams, J. C., and E. Huckle, 2006: Ekman Layer Rectification. *Journal of Physical Oceanography*, **36 (8)**, 1646–1659, doi:10.1175/JPO2912.1.

McWilliams, J. C., E. Huckle, J. Liang, and P. P. Sullivan, 2014: Langmuir Turbulence in Swell. *Journal of Physical Oceanography*, **44 (3)**, 870–890, doi:10.1175/JPO-D-13-0122.1.

McWilliams, J. C., E. Huckle, J.-H. Liang, and P. P. Sullivan, 2012: The Wavy Ekman Layer: Langmuir Circulations, Breaking Waves, and Reynolds Stress. *Journal of Physical Oceanography*, **42 (11)**, 1793–1816, doi:10.1175/JPO-D-12-07.1.

McWilliams, J. C., E. Huckle, and A. F. Shchepetkin, 2009: Buoyancy Effects in a Stratified Ekman Layer. *Journal of Physical Oceanography*, **39 (10)**, 2581–2599, doi: 10.1175/2009JPO4130.1.

McWilliams, J. C., and J. M. Restrepo, 1999: The wave-driven ocean circulation. *Journal of Physical Oceanography*, **29 (10)**, 2523–2540.

McWilliams, J. C., P. P. Sullivan, and C.-H. Moeng, 1997: Langmuir turbulence in the ocean. *Journal of Fluid Mechanics*, **334**, 1–30.

Miles, J., 1994: Analytical solutions for the Ekman layer. *Boundary-Layer Meteorology*, **67 (1-2)**, 1–10, doi:10.1007/BF00705505.

Moum, J. N., and D. R. Caldwell, 1985: Local Influences on Shear-Flow Turbulence in the Equatorial Ocean. *Science*, **230 (4723)**, 315–316, doi:10.1126/science.230.4723.315.

Moum, J. N., R.-C. Lien, A. Perlin, J. D. Nash, M. C. Gregg, and P. J. Wiles, 2009: Sea surface cooling at the Equator by subsurface mixing in tropical instability waves. *Nature Geoscience*, **2 (11)**, 761–765, doi:10.1038/ngeo657.

Moum, J. N., A. Perlin, J. D. Nash, and M. J. McPhaden, 2013: Seasonal sea surface cooling in the equatorial Pacific cold tongue controlled by ocean mixing. *Nature*, **500 (7460)**, 64–67, doi:10.1038/nature12363.

Nagai, T., A. Tandon, and D. L. Rudnick, 2006: Two-dimensional ageostrophic secondary

circulation at ocean fronts due to vertical mixing and large-scale deformation. *Journal of Geophysical Research*, **111 (C9)**, doi:10.1029/2005JC002964.

Niiler, P. P., 1969: On the Ekman divergence in an oceanic jet. *Journal of Geophysical Research*, **74 (28)**, 7048–7052, doi:10.1029/JC074i028p07048.

O'Brien, J. J., 1970: A Note on the Vertical Structure of the Eddy Exchange Coefficient in the Planetary Boundary Layer. *Journal of the Atmospheric Sciences*, **27 (8)**, 1213–1215, doi:10.1175/1520-0469(1970)027⟨1213:ANOTVS⟩2.0.CO;2.

Parmhed, O., I. Kos, and B. Grisogono, 2005: An improved Ekman layer approximation for smooth eddy diffusivity profiles. *Boundary-layer meteorology*, **115 (3)**, 399–407.

Pawlowicz, R., B. Beardsley, and S. Lentz, 2002: Classical tidal harmonic analysis including error estimates in MATLAB using T_tide. *Computers & Geosciences*, **28 (8)**, 929–937, doi:10.1016/S0098-3004(02)00013-4.

Peters, H., and M. C. Gregg, 1988: Some Dynamical and Statistical Properties of Equatorial Turbulence. *Elsevier Oceanogr. Ser.*, Vol. 46, Elsevier, Amsterdam, 185–200.

Peters, H., M. C. Gregg, and T. B. Sanford, 1994: The diurnal cycle of the upper equatorial ocean: Turbulence, fine-scale shear, and mean shear. *Journal of Geophysical Research*, **99 (C4)**, 7707, doi:10.1029/93JC03506.

Peters, H., M. C. Gregg, and T. B. Sanford, 1995: On the parameterization of equatorial turbulence: Effect of fine-scale variations below the range of the diurnal cycle. *Journal of Geophysical Research*, **100 (C9)**, 18 333, doi:10.1029/95JC01513.

Peters, H., M. C. Gregg, and J. M. Toole, 1988: On the parameterization of equatorial turbulence. *Journal of Geophysical Research*, **93 (C2)**, 1199, doi:10.1029/JC093iC02p01199.

Pham, H. T., S. Sarkar, and K. B. Winters, 2013: Large-Eddy Simulation of Deep-Cycle Turbulence in an Equatorial Undercurrent Model. *Journal of Physical Oceanography*, **43 (11)**, 2490–2502, doi:10.1175/JPO-D-13-016.1.

Pollard, R. T., and L. A. Regier, 1992: Vorticity and Vertical Circulation at an Ocean Front. *Journal of Physical Oceanography*, **22 (6)**, 609–625, doi:10.1175/1520-0485(1992)022⟨0609:VAVCAA⟩2.0.CO;2.

Pollard, R. T., P. B. Rhines, and R. O. R. Y. Thompson, 1973: The Deepening of the Wind-Mixed Layer. *Geophysical Fluid Dynamics*, **4 (1)**, 381–404, doi:10.1080/03091927208236105.

Polton, J. A., Y.-D. Lenn, S. Elipot, T. K. Chereskin, and J. Sprintall, 2013: Can Drake Passage Observations Match Ekman's Classic Theory? *Journal of Physical Oceanography*, **43 (8)**, 1733–1740.

Polton, J. A., D. M. Lewis, and S. E. Belcher, 2005: The role of wave-induced Coriolis-Stokes forcing on the wind-driven mixed layer. *Journal of Physical Oceanography*, **35 (4)**, 444–457.

Polzin, K., 1996: Statistics of the Richardson Number: Mixing Models and Finestructure. *Journal of Physical Oceanography*, **26 (8)**, 1409–1425, doi:10.1175/1520-0485(1996)026⟨1409:SOTRNM⟩2.0.CO;2.

Ponte, A. L., P. Klein, X. Capet, P.-Y. Le Traon, B. Chapron, and P. Lherminier, 2013: Diagnosing Surface Mixed Layer Dynamics from High-Resolution Satellite Observations: Numerical Insights. *Journal of Physical Oceanography*, **43 (7)**, 1345–1355, doi:10.1175/JPO-D-12-0136.1.

Price, J. F., and M. A. Sundermeyer, 1999: Stratified Ekman layers. *Journal of Geophysical Research*, **104 (C9)**, 20 467, doi:10.1029/1999JC900164.

Price, J. F., R. A. Weller, and R. Pinkel, 1986: Diurnal cycling: Observations and models of the upper ocean response to diurnal heating, cooling, and wind mixing. *Journal of Geophysical Research*, **91 (C7)**, 8411, doi:10.1029/JC091iC07p08411.

Price, J. F., R. A. Weller, and R. R. Schudlich, 1987: Wind-driven ocean currents and Ekman transport. *Science*, **238 (4833)**, 1534–1538.

Ralph, E. A., and P. P. Niiler, 1999: Wind-Driven Currents in the Tropical Pacific. *Journal of Physical Oceanography*, **29 (9)**, 2121–2129, doi:10.1175/1520-0485(1999)029⟨2121:WDCITT⟩2.0.CO;2.

Rascle, N., and F. Ardhuin, 2009: Drift and mixing under the ocean surface revisited: Stratified conditions and model-data comparisons. *Journal of Geophysical Research*, **114 (C2)**, doi:10.1029/2007JC004466.

Rascle, N., and F. Ardhuin, 2013: A global wave parameter database for geophysical applications. Part 2: Model validation with improved source term parameterization. *Ocean Modelling*, **70**, 174–188, doi:10.1016/j.ocemod.2012.12.001.

Rascle, N., F. Ardhuin, P. Queffeulou, and D. Croiz-Fillon, 2008: A global wave parameter database for geophysical applications. Part 1: Wave-current-turbulence interaction parameters for the open ocean based on traditional parameterizations. *Ocean Modelling*, **25 (3-4)**, 154–171, doi:10.1016/j.ocemod.2008.07.006.

Reynolds, R. W., N. A. Rayner, T. M. Smith, D. C. Stokes, and W. Wang, 2002: An Improved In Situ and Satellite SST Analysis for Climate. *Journal of Climate*, **15 (13)**, 1609–1625, doi:10.1175/1520-0442(2002)015⟨1609:AIISAS⟩2.0.CO;2.

Risien, C. M., and D. B. Chelton, 2008: A Global Climatology of Surface Wind and Wind Stress Fields from Eight Years of QuikSCAT Scatterometer Data. *Journal of Physical Oceanography*, **38 (11)**, 2379–2413, doi:10.1175/2008JPO3881.1.

Roach, C. J., H. E. Phillips, N. L. Bindoff, and S. R. Rintoul, 2015: Detecting and Characterizing Ekman Currents in the Southern Ocean. *Journal of Physical Oceanography*, **45 (5)**, 1205–1223.

Rudnick, D. L., 1996: Intensive surveys of the Azores Front: 2. Inferring the geostrophic and vertical velocity fields. *Journal of Geophysical Research*, **101 (C7)**, 16 291, doi:10.1029/96JC01144.

Saha, S., and Coauthors, 2006: The NCEP Climate Forecast System. *Journal of Climate*, **19 (15)**, 3483–3517, doi:10.1175/JCLI3812.1.

Samelson, R. M., 1993: Linear instability of a mixed-layer front. *Journal of Geophysical Research*, **98 (C6)**, 10 195, doi:10.1029/93JC00457.

Sanford, T., J. Dunlap, J. Carlson, D. Webb, and J. Girton, 2005: Autonomous velocity and density profiler: EM-APEX. *Current Measurement Technology, 2005. Proceedings of the IEEE/OES Eighth Working Conference*, IEEE, 152–156, doi:10.1109/CCM.2005.1506361.

Santiago-Mandujano, F., and E. Firing, 1990: Mixed-Layer Shear Generated by Wind Stress in the Central Equatorial Pacific. *Journal of Physical Oceanography*, **20 (10)**, 1576–1582, doi:10.1175/1520-0485(1990)020⟨1576:MLSGBW⟩2.0.CO;2.

Schneider, N., and P. Mller, 1994: Sensitivity of the Surface Equatorial Ocean to the Parameterization of Vertical Mixing. *Journal of Physical Oceanography*, **24 (7)**, 1623–1640, doi:10.1175/1520-0485(1994)024⟨1623:SOTSEO⟩2.0.CO;2.

Schudlich, R. R., and J. F. Price, 1998: Observations of Seasonal Variation in the Ekman Layer. *Journal of Physical Oceanography*, **28 (6)**, 1187–1204, doi:10.1175/1520-0485(1998)028⟨1187:OOSVIT⟩2.0.CO;2.

Servain, J., 1991: Simple climatic indices for the tropical Atlantic Ocean and some applications. *Journal of Geophysical Research*, **96 (C8)**, 15 137, doi:10.1029/91JC01046.

Servain, J., A. J. Busalacchi, M. J. McPhaden, A. D. Moura, G. Reverdin, M. Vianna, and S. E. Zebiak, 1998: A Pilot Research Moored Array in the Tropical Atlantic (PIRATA). *Bulletin of the American Meteorological Society*, **79 (10)**, 2019–2031, doi: 10.1175/1520-0477(1998)079⟨2019:APRMAI⟩2.0.CO;2.

Sheih, C. M., 1972: A Theoretical Study of the Diurnal Wind Variations in the Planetary Boundary Layer. *Journal of the Atmospheric Sciences*, **29 (5)**, 995–998, doi:10.1175/ 1520-0469(1972)029⟨0995:ATSOTD⟩2.0.CO;2.

Shinoda, T., 2005: Impact of the Diurnal Cycle of Solar Radiation on Intraseasonal SST Variability in the Western Equatorial Pacific. *Journal of Climate*, **18 (14)**, 2628–2636, doi:10.1175/JCLI3432.1.

Sillmann, J., V. V. Kharin, X. Zhang, F. W. Zwiers, and D. Bronaugh, 2013: Climate extremes indices in the CMIP5 multimodel ensemble: Part 1. Model evaluation in the present climate. *Journal of Geophysical Research: Atmospheres*, **118 (4)**, 1716–1733, doi: 10.1002/jgrd.50203.

Singh, M. P., R. T. McNider, and J. T. Lin, 1993: An analytical study of diurnal wind-structure variations in the boundary layer and the low-level nocturnal jet. *Boundary-Layer Meteorology*, **63 (4)**, 397–423, doi:10.1007/BF00705360.

Skeel, R. D., and M. Berzins, 1990: A Method for the Spatial Discretization of Parabolic Equations in One Space Variable. *SIAM Journal on Scientific and Statistical Computing*, **11 (1)**, 1–32, doi:10.1137/0911001.

Skielka, U. T., J. Soares, A. P. Oliveira, and J. Servain, 2011: Diagnostic of the diurnal cycle of turbulence of the Equatorial Atlantic Ocean upper boundary layer. *Natural Science*, **03 (06)**, 444–455, doi:10.4236/ns.2011.36061.

Smith, J. A., 1992: Observed growth of Langmuir circulation. *Journal of Geophysical Research*, **97 (C4)**, 5651, doi:10.1029/91JC03118.

Smyth, W., 1854: *The Mediterranean: A Memoir, Physical, Historical and Nautical*. J.W. Parker and Son, London, U.K.

Smyth, W. D., D. Hebert, and J. N. Moum, 1996: Local ocean response to a multiphase westerly wind burst: 1. Dynamic response. *Journal of Geophysical Research*, **101 (C10)**, 22 495, doi:10.1029/96JC02005.

Smyth, W. D., and J. N. Moum, 2013: Marginal instability and deep cycle turbulence in the eastern equatorial Pacific Ocean. *Geophysical Research Letters*, **40 (23)**, 6181–6185, doi:10.1002/2013GL058403.

Smyth, W. D., J. N. Moum, L. Li, and S. A. Thorpe, 2013: Diurnal Shear Instability, the Descent of the Surface Shear Layer, and the Deep Cycle of Equatorial Turbulence. *Journal of Physical Oceanography*, **43 (11)**, 2432–2455, doi:10.1175/JPO-D-13-089.1.

Soloviev, A., and R. Lukas, 2014: *The near-surface layer of the ocean: structure, dynamics and applications*, Atmospheric and oceanographic sciences library, Vol. 48. 2nd ed., Springer, Dordrecht.

Soloviev, A., R. Lukas, and P. Hacker, 2001: An approach to parameterization of the oceanic turbulent boundary layer in the western Pacific warm pool. *Journal of Geophysical Research*, **106 (C3)**, 4421, doi:10.1029/2000JC900154.

Stern, M. E., 1965: Interaction of a uniform wind stress with a geostrophic vortex. *Deep Sea Research and Oceanographic Abstracts*, **12 (3)**, 355–367, doi:10.1016/0011-7471(65)90007-0.

Stommel, H., 1960: Wind-drift near the equator. *Deep Sea Research (1953)*, **6**, 298–302, doi:10.1016/0146-6313(59)90088-7.

Stommel, H., K. Saunders, W. Simmons, and J. Cooper, 1969: Observations of the diurnal thermocline. *Deep Sea Res*, **16**, 269–284.

Stuart-Menteth, A. C., 2003: A global study of diurnal warming using satellite-derived sea surface temperature. *Journal of Geophysical Research*, **108 (C5)**, doi:10.1029/2002JC001534.

Stull, R. B., 1950: *An introduction to boundary layer meteorology*, Vol. 13. Springer Science & Business Media.

Sullivan, P. P., and J. C. McWilliams, 2010: Dynamics of Winds and Currents Coupled to Surface Waves. *Annual Review of Fluid Mechanics*, **42 (1)**, 19–42, doi:10.1146/annurev-fluid-121108-145541.

Sun, C., W. D. Smyth, and J. N. Moum, 1998: Dynamic instability of stratified shear flow in the upper equatorial Pacific. *Journal of Geophysical Research*, **103 (C5)**, 10 323, doi:10.1029/98JC00191.

Tan, Z.-M., 2001: An Approximate Analytical Solution For The Baroclinic And Variable Eddy Diffusivity Semi-Geostrophic Ekman Boundary Layer. *Boundary-Layer Meteorology*, **98 (3)**, 361–385, doi:10.1023/A:1018708726112.

Tan, Z.-M., and M. M. Farahani, 1998: An analytical study of the diurnal variations of wind in a semi-geostrophic Ekman boundary layer model. *Boundary-Layer Meteorology*, **86 (2)**, 313–332.

Temme, N. M., 1996: *Special functions: an introduction to the classical functions of mathematical physics*. Wiley, New York.

Thomas, L., and R. Ferrari, 2008: Friction, Frontogenesis, and the Stratification of the Surface Mixed Layer. *Journal of Physical Oceanography*, **38 (11)**, 2501–2518, doi:10.1175/2008JPO3797.1.

Thomas, L. N., 2005: Destruction of Potential Vorticity by Winds. *Journal of Physical Oceanography*, **35 (12)**, 2457–2466, doi:10.1175/JPO2830.1.

Thomas, L. N., 2007: Dynamical constraints on the extreme low values of the potential vorticity in the ocean. *Proc. 15th Aha Huliko a Hawaiian Winter Workshop*, 117–124.

Thomas, L. N., and C. M. Lee, 2005: Intensification of Ocean Fronts by Down-Front Winds. *Journal of Physical Oceanography*, **35 (6)**, 1086–1102, doi:10.1175/JPO2737.1.

Thomas, L. N., and P. B. Rhines, 2002: Nonlinear stratified spin-up. *Journal of Fluid Mechanics*, **473**, 211–244.

Thompson, L., 2000: Ekman layers and two-dimensional frontogenesis in the upper ocean. *Journal of Geophysical Research*, **105 (C3)**, 6437, doi:10.1029/1999JC900336.

Thorpe, S. A., and Z. Liu, 2009: Marginal Instability? *Journal of Physical Oceanography*, **39 (9)**, 2373–2381, doi:10.1175/2009JPO4153.1.

Van de Wiel, B. J. H., A. F. Moene, G. J. Steeneveld, P. Baas, F. C. Bosveld, and A. A. M. Holtslag, 2010: A Conceptual View on Inertial Oscillations and Nocturnal Low-Level Jets. *Journal of the Atmospheric Sciences*, **67 (8)**, 2679–2689, doi:10.1175/2010JAS3289.1.

Wade, M., G. Caniaux, Y. duPenhoat, M. Dengler, H. Giordani, and R. Hummels, 2011: A one-dimensional modeling study of the diurnal cycle in the equatorial Atlantic at the PIRATA buoys during the EGEE-3 campaign. *Ocean Dynamics*, **61 (1)**, 1–20, doi:10.1007/s10236-010-0337-8.

Waliser, D. E., and C. Gautier, 1993: A Satellite-derived Climatology of the ITCZ. *Journal of Climate*, **6 (11)**, 2162–2174, doi:10.1175/1520-0442(1993)006⟨2162:ASDCOT⟩2.0.CO;2.

Ward, B., 2006: Near-surface ocean temperature. *Journal of Geophysical Research*, **111 (C2)**, doi:10.1029/2004JC002689.

Weisberg, R. H., and T. J. Weingartner, 1988: Instability Waves in the Equatorial Atlantic Ocean. *Journal of Physical Oceanography*, **18 (11)**, 1641–1657, doi:10.1175/1520-0485(1988)018⟨1641:IWITEA⟩2.0.CO;2.

Welander, P., 1957: Wind Action on a Shallow Sea: Some Generalizations of Ekman's Theory. *Tellus*, **9 (1)**, 45–52, doi:10.1111/j.2153-3490.1957.tb01852.x.

Weller, R. A., and A. J. Plueddemann, 1996: Observations of the vertical structure of the oceanic boundary layer. *Journal of Geophysical Research*, **101 (C4)**, 8789, doi:10.1029/96JC00206.

Wenegrat, J. O., and M. J. McPhaden, 2015a: Dynamics of the surface layer diurnal cycle in the equatorial Atlantic Ocean (0°, 23°W). *Journal of Geophysical Research: Oceans*, **120 (1)**, 563–581, doi:10.1002/2014JC010504.

Wenegrat, J. O., and M. J. McPhaden, 2015b: Wind, waves, and fronts: Frictional effects in a generalized Ekman model. *Journal of Physical Oceanography*, doi:10.1175/JPO-D-15-0162.1.

Wenegrat, J. O., M. J. McPhaden, and R.-C. Lien, 2014: Wind stress and near-surface shear in the equatorial Atlantic Ocean. *Geophysical Research Letters*, **41 (4)**, 1226–1231, doi:10.1002/2013GL059149.

Wijffels, S., E. Firing, and H. Bryden, 1994: Direct Observations of the Ekman Balance at 10N in the Pacific. *Journal of Physical Oceanography*, **24 (7)**, 1666–1679, doi:10.1175/1520-0485(1994)024⟨1666:DOOTEB⟩2.0.CO;2.

Wilcox, R. R., 2010: *Fundamentals of modern statistical methods: Substantially improving power and accuracy*. Springer Science & Business Media.

Woolnough, S. J., F. Vitart, and M. A. Balmaseda, 2007: The role of the ocean in the Madden-Julian Oscillation: Implications for MJO prediction. *Quarterly Journal of the Royal Meteorological Society*, **133 (622)**, 117–128, doi:10.1002/qj.4.

Wu, R., and W. Blumen, 1982: An Analysis of Ekman Boundary Layer Dynamics Incorporating the Geostrophic Momentum Approximation. *Journal of the Atmospheric Sciences*, **39 (8)**, 1774–1782, doi:10.1175/1520-0469(1982)039⟨1774:AAOEBL⟩2.0.CO;2.

Xie, S.-P., and J. A. Carton, 2004: Tropical Atlantic variability: Patterns, mechanisms, and impacts. *Earth Climate: The Ocean-Atmosphere Interaction, Geophys. Monogr*, **147**, 121–142.

Xu, Z., and A. J. Bowen, 1994: Wave-and wind-driven flow in water of finite depth. *Journal of physical oceanography*, **24 (9)**, 1850–1866.

Zebiak, S. E., 1993: Air-Sea Interaction in the Equatorial Atlantic Region. *Journal of Climate*, **6 (8)**, 1567–1586, doi:10.1175/1520-0442(1993)006⟨1567:AIITEA⟩2.0.CO;2.

Zhang, Y., and Z.-M. Tan, 2002: The diurnal wind variation in a variable eddy viscosity semi-geostrophic Ekman boundary-layer model: Analytical study. *Meteorology and Atmospheric Physics*, **81 (3-4)**, 207–217.

Zikanov, O., D. N. Slinn, and M. R. Dhanak, 2003: Large-eddy simulations of the wind-induced turbulent Ekman layer. *Journal of Fluid Mechanics*, **495**, 343–368, doi:10.1017/S0022112003006244.